

THESIS

KINEMATIC STRUCTURES, DIABATIC PROFILES, AND PRECIPITATION SYSTEMS  
IN WEST AFRICA DURING SUMMER 2006

Submitted by

Adam James Davis

Department of Atmospheric Science

In partial fulfillment of the requirements

For the Degree of Master of Science

Colorado State University

Fort Collins, Colorado

Spring 2013

Master's Committee:

Advisor: Richard Johnson

Eric Maloney  
Michael Kirby

Copyright by Adam James Davis 2013

All Rights Reserved

## ABSTRACT

### KINEMATIC STRUCTURES, DIABATIC PROFILES, AND PRECIPITATION SYSTEMS IN WEST AFRICA DURING SUMMER 2006

West Africa is a region characterized by great spatial contrasts in temperature, precipitation, and topography, which combine to create many complex and interesting weather phenomena. In particular, the area is home to a seasonal monsoon, propagating easterly waves, and some of the most intense thunderstorm systems on Earth. These types of events have both local and global effects – precipitation variability has a major bearing on regional water resource issues, while West Africa is also the source of many of the disturbances that develop into tropical cyclones in the North Atlantic Ocean. Unfortunately, atmospheric data has historically been very sparse in West Africa, leading to an incomplete understanding of many of these meteorological features and a corresponding difficulty in modeling them accurately. An exceptional opportunity for improvement on these fronts exists thanks to the African Monsoon Multidisciplinary Analysis (AMMA) field campaign, which collected an unprecedented quantity of observations throughout the region, with the most concentrated effort during the summer of 2006. This work uses a gridded analysis of radiosonde measurements obtained during AMMA and places those observations in the context of AMMA radar data and satellite rainfall estimates to examine the patterns of kinematic and diabatic quantities in West Africa relative to the summer monsoon phase, easterly wave disturbances, precipitation systems, and the diurnal cycle.

Many unique aspects of West African weather compared to conditions elsewhere in the tropics are revealed by this study. The meridional transitions related to the West African monsoon comprise the predominant control on the location and intensity of precipitation at

seasonal time scales, with variations in convective activity related to the Madden-Julian Oscillation contributing at 25 to 60 day periods. On shorter time scales of two to six days, easterly wave disturbances look to be the principal factor governing the timing of rainfall events, though especially persistent cold pools and residual cloudiness generated by thunderstorm systems also act as constraints on convective evolution on the days following a precipitation episode. One of the most distinctive traits of the study region in West Africa compared to other tropical areas is the particular prevalence of convective downdrafts, chiefly those associated with mesoscale zones of stratiform precipitation in thunderstorm complexes. These features, along with the gravity waves forced by their characteristic heating pattern, have an especially large influence on the time-mean atmospheric structure relative to the majority of the tropics. A comparison of the diabatic profiles from the AMMA dataset with those from other field projects indicates that the signals of both convective downdrafts and diurnal variations of the planetary boundary layer are much stronger in West Africa than in the previously studied regions. Beyond the mentioned differences, though, the AMMA profiles show resemblance to those from both western Pacific and eastern Atlantic field campaigns.

The vertical patterns of atmospheric variables tend to be complex and multi-layered in West Africa, suggesting that the area is home to an especially diverse cloud population, with contributions from numerous height regimes prominent enough to influence the mean state. Meridional differences within the domain of the analysis are evident, including indications of more intense convective updrafts toward the north, stronger effects of boundary layer mixing in the north, and a greater influence of mesoscale convective system downdrafts toward the south. The diurnal cycle of precipitation appears most prominently shaped by convective initiation near areas of high topography and the subsequent development and long-distance propagation of

extensive, well-organized thunderstorm systems, though there seem to be effects related to diurnal flow patterns near the Gulf of Guinea coast too. Inland, moisture transport achieved by the nocturnal low-level jet is a key influence on rainfall, with mixing by the daytime boundary layer playing an important function as well. Changes in the relative contribution and intensity of deep convective and stratiform heating and moistening patterns arise among different times of day and night, as the leading precipitation regime transitions from developing deep convection at midday to organizing thunderstorm systems by evening and propagating thunderstorm complexes with extensive stratiform rainfall overnight.

The analyses in the present work demonstrate a few different issues and caveats that need to be considered when utilizing observational or remote sensing datasets. Namely, the timing of radiosonde launches and the spacing of the sounding site array combined to create a delay between when convective systems passed the Niamey, Niger measurement site and when their effects were detected in the gridded AMMA sounding data. Similarly, infrared satellite rainfall estimates from the Tropical Rainfall Measuring Mission (TRMM) are shown to have a time lag of about three hours between when precipitation actually occurs and when it appears in the estimate product, complicating the intended use of the data in evaluating the diurnal cycle of rainfall.

## ACKNOWLEDGMENTS

I would like to express my sincere gratitude to the numerous parties without whom the completion of the present work would not have been possible. First, I thank my advisor, Professor Richard Johnson, for his insightful guidance, support, and encouragement throughout my years of graduate study. His assistance in formulating, planning the course of, and interpreting the results of this research project have proven invaluable. I also thank the other members of my committee, Professors Eric Maloney and Michael Kirby, for their thoughtful evaluations and recommendations regarding my work. The contributions of Paul Ciesielski to my research are greatly appreciated as well; he provided the vast majority of the data on which this work is based, along with numerous figures and helpful computer code, and made himself readily available to answer any scientific, algorithmic, and mathematical questions that I had along the way. I need to recognize Rick Taft for his work in keeping all of the office computing hardware and software running smoothly and for his technical help in taming everything from scanners to poster printers. I would like to acknowledge the rest of the members of the Johnson group too, for their helpful comments and assistance during the course of my time at Colorado State University. The research presented here has been generously supported by NASA Precipitation Measurement Missions Grant NNX10AG81G (PI: Richard Johnson), a NASA Center for Earth Atmosphere Studies (CEAS) graduate fellowship awarded to the author, and the support of Dr. Ramesh Kakar; the backing of these funding sources has allowed this project to come to fruition and is deeply appreciated.

I also wish to recognize the guidance provided by my CEAS mentor at NASA, Dr. Scott Braun, whose astute remarks and beneficial suggestions concerning my work helped shape its direction in a very positive way. Dr. Nick Guy was a valuable resource during this project as

well; his provision of radar data, computer programs, and fresh observations to this study are certainly appreciated. I thank Professor Rosana Nieto Ferreira for providing the Niamey radar case log from which the convective systems studied in Chapter 6 of this paper were selected. The members of the University of Utah Tropical Meteorology Group, especially Professors Edward Zipser and Chuntao Liu, likewise deserve recognition for their work in designing and constructing the TRMM precipitation feature database used in this project, as well as for kindly making this data openly available for scientific inquiry. I would like to acknowledge the great amounts of time, energy, and hard work expended by the international team of scientists who, based on French initiative, managed to design and carry out the AMMA field project, which inspired and enabled the entirety of this inquiry. Lastly, I thank my family and friends, particularly my parents, Linda and Jim, and my brother, Jacob, for their caring support and advice throughout my educational career. Their backing has given me the confidence and determination necessary to succeed, and to them I am forever grateful.

## TABLE OF CONTENTS

Abstract.....	ii
Acknowledgments.....	v
1. Introduction.....	1
2. Background.....	7
a. Diabatic Variables and Convective Structures.....	7
b. West African Monsoon.....	13
c. African Easterly Jet, Easterly Waves, and Convective Systems.....	16
d. Diurnal Cycle.....	26
3. Data and Methods.....	30
a. Datasets.....	30
b. Methodology.....	35
4. Mean Properties and Variability of Flow, Diabatic Profiles, and Precipitation during Summer 2006.....	45
a. West African Monsoon Cycle.....	45
b. EBA-Average Conditions.....	50
c. Mean Meridional Cross Sections.....	74
5. Diurnal Cycle.....	79
a. AMMA Gridded Dataset Meridional Cross Sections.....	79
b. TRMM Precipitation Meridional Cross Sections.....	97
6. MCS-Relative Heating, Moistening, and Vertical Motion.....	107
a. Case Selection.....	107
b. Composite MCS-Relative Vertical Profiles.....	110
c. Individual MCS Cases and Discussion.....	134
7. Conclusion.....	140
References.....	145

# CHAPTER 1

## INTRODUCTION

West Africa is a region brimming with physical contrasts, encompassing wide variations in climactic temperature and precipitation, elevation, and land cover. In particular, the striking differences in the north-south direction create a unique environment that gives rise to complex and interesting weather phenomena. Figure 1.1 presents a map of the predominant vegetation and land cover types throughout the African continent. Focusing on West Africa, from Niger and Nigeria westward to the Atlantic Ocean, a distinct zonal banding pattern predominates. Near the Gulf of Guinea coast that defines the southern edge of the region, wet conditions support regions of tropical rainforest, while the most prevalent flora type transitions to woodland savanna and then grassland savanna moving inland. Even farther to the north, as the environment becomes drier, the nature of the ecosystem evolves further to a steppe regime, a semi-desert zone, and finally the Sahara desert. These profound meridional changes illustrate a strong gradient from a warm and wet climate near the coast to a hot and dry climate well inland.

The uniformity of these weather regimes and biome types in the east-west direction is disrupted by variations in topography across the region. A map of the surface elevation throughout West Africa is shown in Figure 1.2. Much of the area is characterized by gentle relief and low elevation, but there are also several zones of high terrain. These include the Guinea Highlands in the central and eastern part of the country of the same name, the Jos Plateau in north-central Nigeria, the Aïr Mountains in northern Niger, the Adamawa Highlands of western Cameroon, and the Darfur Mountains of western Sudan (Laing et al. 2008). Additional zones of moderately high terrain are found in southern and central Togo, northern Benin, and

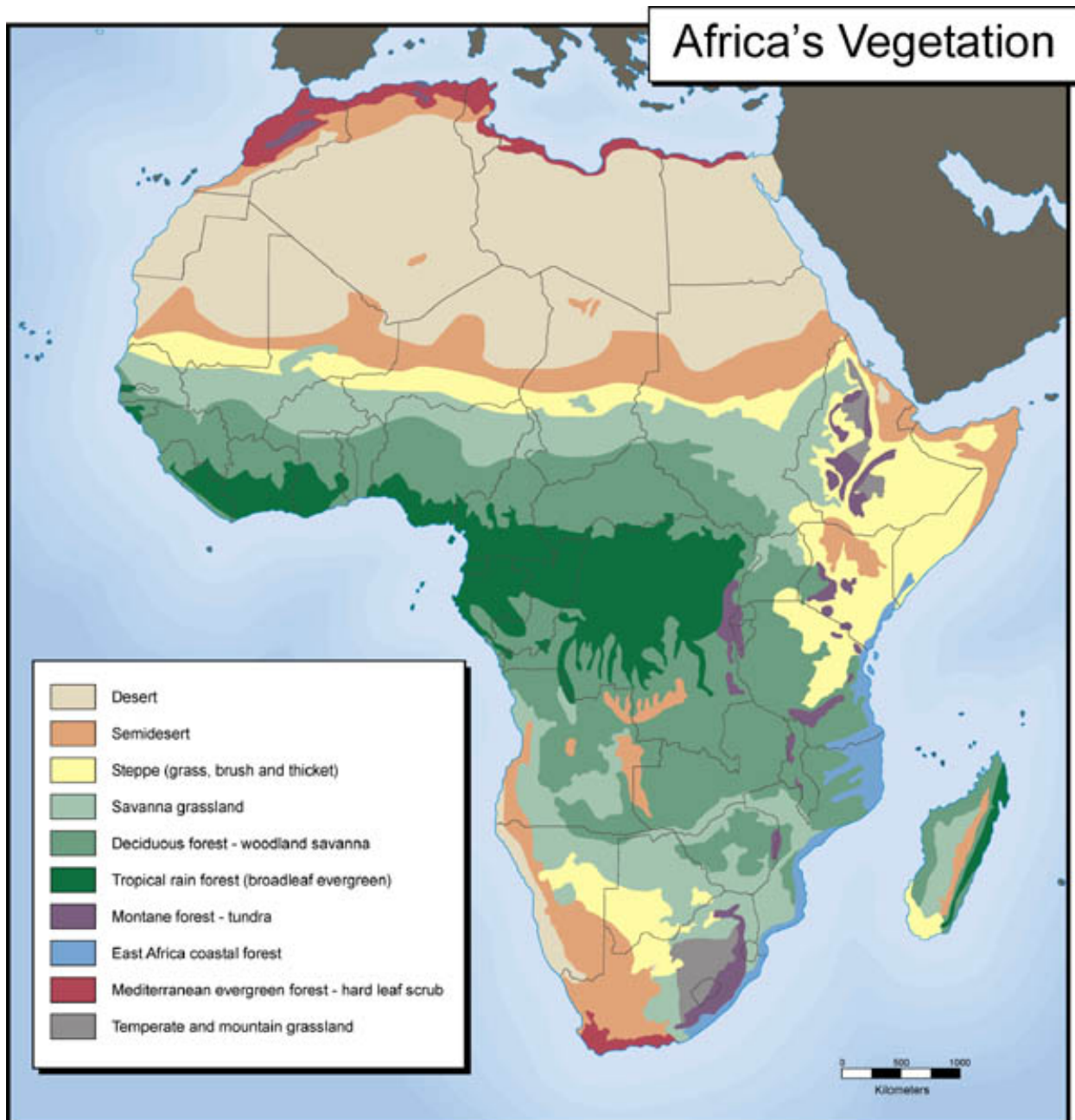


**Figure 1.1** Map of predominant vegetation and land cover types in Africa. Figure provided by the Exploring Africa! online curriculum, created by the African Studies Center and MATRIX digital humanities center at Michigan State University. Unit 2: Studying Africa through the Social Studies, Module 6: The Geography of Africa, Climate and Vegetation of Africa Map. Available online at <http://exploringafrica.matrix.msu.edu/images/africavegetation.jpg>.

southwestern Nigeria. The influence of several of these hilly and mountainous areas on precipitation patterns can be seen in Figure 1.1. For instance, the woodland savanna/grassland savanna boundary in northern Nigeria bends northward on the west side of the Jos Plateau, but

## Surface Elevation (m)

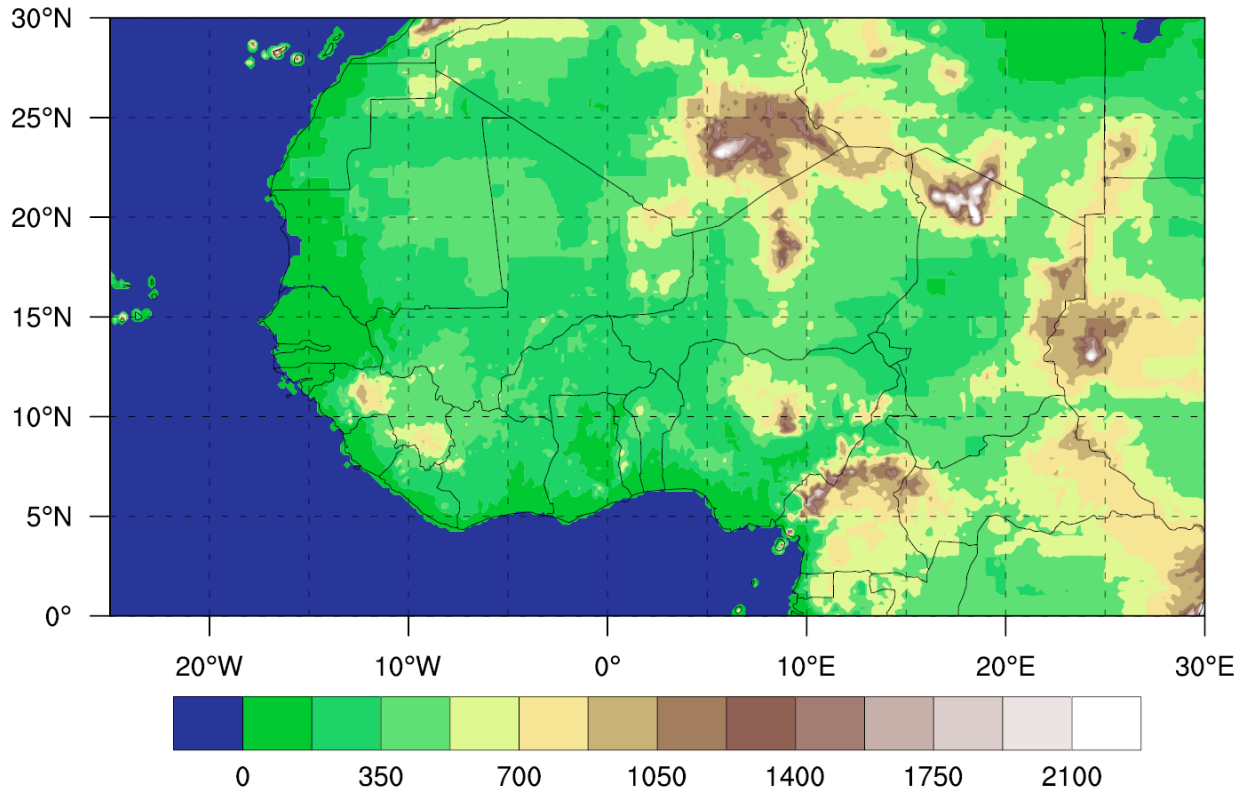


**Figure 1.2** Map of surface elevation in West Africa, in units of meters. Values are from a 10-minute resolution gridded elevation dataset created by the National Center for Atmospheric Research, provided via personal communication from Paul Ciesielski.

southward on the east side of the feature. This pattern suggests greater precipitation on the west side of the high terrain, which is the windward side during the summer monsoon season, and reduced rainfall on the east side, which is in the lee of the typical summer monsoon flow. As another example, the margin of the semi-desert zone is substantially displaced northward into the desert region in the vicinity of the Air Mountains and the Darfur Mountains, indicative of enhanced precipitation in connection with those orographic features as well.

The robust mean temperature and moisture gradients in the north-south direction and the areas of topographic relief interact to yield a variety of fascinating weather patterns and events in West Africa. As mentioned previously, West Africa is affected by a seasonal monsoon, which is associated with changes in wind regimes, variations in the latitude of maximum precipitation,

and coupling among the Gulf of Guinea, the Sahara desert, and the atmosphere in the region. African easterly wave disturbances propagate across this area as well, which display important feedbacks with heavy rain events. Much of the convective activity in West Africa becomes organized on the mesoscale – in fact, this region is home to some of the most intense thunderstorm systems on Earth! Accordingly, these phenomena are interesting subjects for study from a pure scientific perspective. However, understanding the weather in West Africa is also important for societal reasons. Water scarcity can be a major problem in the area, particularly in the semi-arid zone well inland, which is referred to as the Sahel. Thus, improved knowledge of precipitation in this region can have major benefits on agricultural and humanitarian fronts. Moreover, many of the summertime storm systems that move from east to west across northern Africa act as precursor disturbances for developing tropical cyclones over the Atlantic Ocean (Thorncroft and Hodges 2001). Consequently, a better understanding of the weather in West Africa can have important benefits even for locations thousands of miles away. Unfortunately, this region has historically been a data-sparse zone from an atmospheric science viewpoint. Observation stations tended to be far apart, or non-existent in some areas, and measurements were infrequent or unreliable. In accordance with this lack of data, accurately modeling weather and climate in West Africa was also a challenge. The outcome was an incomplete understanding of many of the meteorological features in the area.

In order to remedy these issues, the African Monsoon Multidisciplinary Analysis (AMMA) and NASA AMMA (NAMMA) field projects were conducted throughout West Africa (Redelsperger et al. 2006, Lebel et al. 2010). The projects comprised several nested time scales – a long-term monitoring program, based on existing infrastructure, extended from 2001 to 2009, an Enhanced Observing Period (EOP) from 2005 to 2007 saw an intensification and coordination

of the long-term networks, and a series of Special Observing Periods (SOPs) during 2006 were associated with the most extensive and thorough measurements. The SOPs in the summer of 2006, in particular, saw the deployment of a great variety of instruments throughout West Africa. An upper-air network of radiosonde launch sites was established that released weather balloons four times daily over a period of several months. Several weather radars were set up throughout the region to collect frequent, high-resolution observations of precipitation systems. Instrumented ships and buoys took measurements of conditions in the Gulf of Guinea and elsewhere in the eastern Atlantic Ocean. Rain gauge networks were established to measure precipitation variability from the regional scale to the local scale. Surface flux towers, lidars, radar profilers, sodars, and related instruments were installed to measure aerosol loading, optical properties, and cloud radiative effects. Six research aircraft were involved in flights throughout West Africa to collect both chemistry and weather-related observations, using in situ measurement systems, remote sensing instruments, and dropsondes.

The wealth of data collected by these field campaigns has contributed to numerous studies that have improved the scientific understanding of weather and climate in West Africa and continues to inspire additional research. In the present work, extensive use is made of the upper-air radiosonde observations collected by the network of AMMA weather balloon sites during the summer of 2006. Together with rainfall estimates from AMMA Doppler radar data and satellite readings from the Tropical Rainfall Measuring Mission (TRMM), these measurements are used to examine the vertical profiles of kinematic and diabatic quantities in West Africa in the context of the summer monsoon phase, easterly wave disturbances, precipitation systems, and the diurnal cycle.

Background information for the material presented in this paper is provided in Chapter 2. This includes details on the diabatic variables used; basic heating and moistening vertical patterns; a brief description of the structure of mesoscale convective systems; an overview of the West African monsoon; a discussion of the African easterly jet, African easterly waves, and their relationship with thunderstorm activity; and a review of the diurnal cycle of precipitation in the region. Further details about the various datasets used in this study are given in Chapter 3, along with explanations of the methodologies used to analyze them. Chapter 4 includes numerous looks into the mean properties and the variability of atmospheric flow, diabatic profiles, and precipitation events in West Africa during the summer 2006 study period. The diurnal cycle of these kinematic and diabatic quantities is examined in Chapter 5, as well as their connection to the timing of precipitation, and the differences among precipitation estimates from various sources. The patterns of temperature, humidity, heating, moistening, and winds with respect to passing mesoscale convective systems are investigated in Chapter 6. Lastly, Chapter 7 provides a summary of the paper's findings, a discussion of some of the challenges encountered, suggestions for avenues of future research, and concluding remarks.

## CHAPTER 2

### BACKGROUND

#### a. Diabatic Variables and Convective Structures

Two diabatic quantities that will be used frequently in this paper are the  $Q_1$  apparent heat source and the  $Q_2$  apparent moisture sink, as introduced by Yanai et al. (1973). Following the discussion in that paper, dry static energy can be defined as  $s \equiv c_p T + gz$ , or the sum of enthalpy and gravitational potential energy per unit mass, where  $c_p$  is the specific heat capacity at constant pressure of dry air,  $T$  is temperature,  $g$  is the acceleration of gravity, and  $z$  is geopotential height. Similarly, moist static energy is defined as  $h \equiv s + Lq$ , or the sum of dry static energy and “latent” energy associated with water vapor, where  $L$  is the enthalpy of vaporization of water and  $q$  is the water vapor mixing ratio. Then, the apparent heat source is defined by  $Q_1 \equiv \partial s / \partial t + u \partial s / \partial x + v \partial s / \partial y + \omega \partial s / \partial p$ , where  $t$  represents time,  $u$  and  $v$  are the zonal and meridional horizontal wind, respectively,  $x$  and  $y$  are the zonal and meridional horizontal directions, respectively,  $\omega$  represents the vertical velocity in pressure coordinates, and  $p$  represents pressure. All of the dry static energy and wind values in the equation for  $Q_1$  correspond to averages over some large-scale area, such as a grid box or sounding array, since the apparent heat source is intended to represent the effects of sub-grid-scale diabatic processes and heat fluxes on the large-scale environment. In turn, the apparent moisture sink  $Q_2$  is defined as  $Q_2 \equiv -L (\partial q / \partial t + u \partial q / \partial x + v \partial q / \partial y + \omega \partial q / \partial p)$ , with all symbols used as previously defined. The water vapor mixing ratio and wind values in the apparent moisture sink equation also represent large-scale averages, since  $Q_2$  is also meant to characterize the impacts of sub-grid-scale diabatic processes and moisture fluxes on the broader environment. After computing  $Q_1$  and  $Q_2$  using these defining equations, it

is conventional to divide the values by  $c_p$ , to convert the units from energy per mass per time to the more easily interpreted temperature per time; this approach will be followed in the present work.

Using the first law of thermodynamics, the sources and sinks of dry static energy and moisture in the atmosphere, the continuity equation, and Reynolds averaging, the following physical interpretations of the apparent heat source and apparent moisture sink can be made (Yanai et al. 1973, Yanai and Johnson 1993, Maloney 2011a). The apparent heat source is expressed as  $Q_1 = Q_R + L(\bar{c} - \bar{e}) - \partial(\overline{s'u'})/\partial x - \partial(\overline{s'v'})/\partial y - \partial(\overline{s'\omega'})/\partial p$ , where  $Q_R$  is the radiative heating rate,  $c$  is the condensation rate,  $e$  is the evaporation rate, and other symbols are used as previously defined. The overbars represent the large-scale averages of quantities over the area for which  $Q_1$  was computed, while the primes represent deviations from the large-scale mean values. This interpretation relationship for  $Q_1$  indicates why the variable is called the “apparent” heat source – it includes the effects of actual heat sources and sinks, namely radiation and net condensation or evaporation, as well as “apparent” sources and sinks of heat on the large scale that are actually associated with flux convergences due to sub-grid-scale motions. These “eddy” fluxes represent the influence of unresolved flow within the averaging domain on the large-scale heat budget, though given a large enough grid size (on the order of 100 km or more), these motions tend to be associated with processes like convective updrafts, which might not normally be thought of as eddies. It is also typical in the interpretation of  $Q_1$  to neglect the horizontal flux convergence terms (the third and fourth terms on the right hand side of the equation), based on the assumption that the domain-averaged horizontal dry static energy flux convergence is small compared to the horizontal transport connected with large-scale processes. This leaves radiative heating, net condensation or evaporation, and vertical eddy heat flux convergence as the leading

terms contributing to  $Q_1$ . However, Yanai and Johnson (1993) point out that the sub-grid-scale horizontal flux convergences of dry static energy cannot always be neglected, as mesoscale circulations can result in appreciable fluxes through the sides of the averaging domain.

A corresponding equation for the apparent moisture sink is  $Q_2 = L(\bar{c} - \bar{e}) + L \partial(\bar{q}'\bar{u}')/\partial x + L \partial(\bar{q}'\bar{v}')/\partial y + L \partial(\bar{q}'\bar{\omega}')/\partial p$ , with all variables used as defined previously. Again, overbars correspond to averages over the large-scale area for which  $Q_2$  was calculated, while primes designate deviations from that mean. Similar to the apparent heat source, the apparent moisture sink is so named because it incorporates the actual sink of “latent” energy, net condensation, along with “apparent” large-scale sinks connected with moisture flux divergences due to sub-grid-scale flow. Conventionally, the horizontal flux terms are also neglected in the interpretation of  $Q_2$ , leaving just net condensation or evaporation and vertical eddy moisture flux divergence to explain the apparent moisture sink values, though similar to the disregard of the horizontal flux terms in the  $Q_1$  expression, this may not always be a valid assumption either. Using the equations for the interpretation of the apparent heat source and apparent moisture sink and neglecting the horizontal flux terms, it can also be discerned that the difference between these quantities can be expressed as  $Q_1 - Q_2 = Q_R - \partial(\bar{h}'\bar{\omega}')/\partial p$ . Thus, the difference between  $Q_1$  and  $Q_2$  represents the combined effects of radiative heating and vertical eddy moist static energy flux convergence.

In the context of tropical precipitation systems, the vertical profile of  $Q_1$  is traditionally interpreted as being composed of a combination of three major heating structures, which are associated with three different main cloud types (Johnson et al. 1999, Schumacher et al. 2004, Schumacher et al. 2007, Zhang and Hagos 2009, Maloney 2011b). Figure 2.1 provides a schematic diagram of these predominant heating modes, and a few examples of the net result

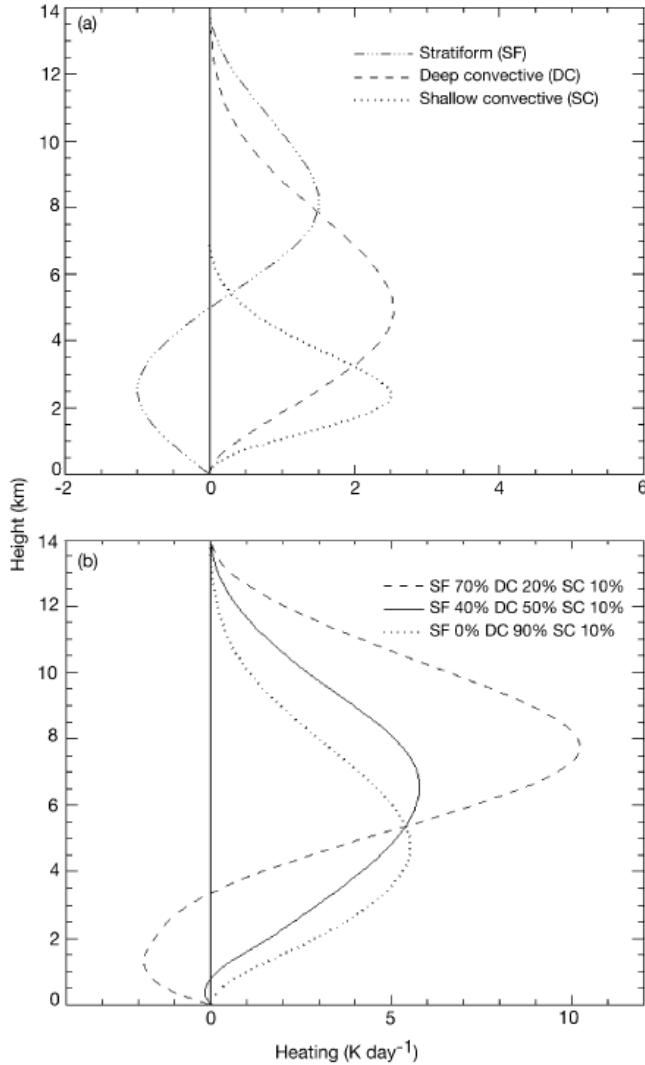


FIG. 3. Idealized stratiform, deep convective, and shallow convective latent heating profiles. The  $x$  axis is meant to be nondimensional until a precipitation amount is specified. (b) Total latent heating profiles for 0%, 40%, and 70% stratiform rain fractions, assuming  $3.5 \text{ m yr}^{-1}$  rain accumulation.

**Figure 2.1** Schematic vertical profiles of major tropical latent heating modes (top panel) and example net latent heating structures from superimposing these modes in various proportions (bottom panel). From Schumacher et al. (2004), Figure 3.

from old, weakening convection. This scheme consists of heating aloft overlying cooling at low levels, with a sign change at mid levels. As a point of terminology, Houze (1997) points out that all three of these cloud types actually result from the process of convection, which is simply the

when they are superimposed in various proportions. The first of the leading modes is the shallow convective pattern, which is associated with cumulus clouds with little vertical development as well as the moderately deeper cumulus congestus type, and is represented by heating in the lower half of the troposphere, with a peak a few kilometers above the surface. Next is the deep convective regime, which is connected with cumulonimbus clouds containing vigorous updrafts that have great vertical extent. This pattern comprises deep heating throughout the troposphere, with a peak at mid levels. The third structure is known as the stratiform mode, which is associated with

the mesoscale regions of layered, gentle ascent in the upper troposphere and the light to moderate precipitation that result

overturning of a fluid under gravity. However, the word convective is traditionally used to describe the vigorous air motions, intense precipitation, and predominant vertical orientation of young, active convection, with “deep” and “shallow” convection being defined in a relative sense, depending on the proportion of the troposphere through which the clouds and updrafts extend. The term stratiform is used to describe older, less active convection, which has weaker vertical motion and precipitation, and takes on a more horizontally uniform, layered structure. As shown in the lower panel of Figure 2.1, a cloud population that is dominated by the convective type will tend to yield a heating profile with positive  $Q_1$  throughout the tropospheric column and a mid-level peak. As the proportion of the stratiform regime increases, though, the maximum in heating intensifies and develops higher in the upper levels, while net cooling takes over near the surface.

Mesoscale convective systems (MCSs), in particular, often include multiple cloud types and heating regimes together. Houze (2004) defines an MCS as “a cumulonimbus cloud system that produces a contiguous precipitation area  $\sim 100$  km or more in at least one direction,” and notes that such systems are responsible for much of the precipitation that falls in the tropics and tend to have more complex dynamics than lone thunderstorms or simple lines of thunderstorms. Specifically, MCSs frequently contain extensive regions of stratiform precipitation along with convective activity, which results in substantial effects on their heating and moistening influence on the large scale. The thunderstorm activity that, by definition, must take place within an MCS is frequently organized into lines or clusters, and these areas are characterized by the predominance of deep updrafts. This general rising motion throughout the troposphere is associated with near-surface convergence and divergence at upper levels within this portion of

the MCS (Houze 1997). Additionally, the net condensation that takes place in this zone, associated with intense precipitation, creates strong heating at all levels (Houze 2004).

The region of stratiform precipitation, while contiguous with the convective area, may occur ahead of, behind, or parallel to the band of deep convection. The stratiform zone tends to have a cloud base at mid levels, beneath a region of rising motion that is associated with both broad-scale layer lifting and continued positive buoyancy as the old, weakening convection that comprises this part of the MCS gradually declines in intensity. Below the cloud base, the stratiform area is characterized by descending motion, which is largely associated with the melting and evaporation of precipitation falling from the clouds above (Houze 2004). This pattern of mesoscale ascent overlying sinking motion below is connected with convergence at mid levels, while divergence predominates both aloft and near the surface (Houze 1997). In terms of  $Q_1$ , the rising motion, net condensation, and net deposition in the upper levels are associated with heating aloft, while melting, evaporation, and sublimation yield cooling at low levels (Houze 2004). In particular, due to the role of melting both as a diabatic cooling process and in transforming hydrometeors from slower-falling snow and ice to faster-falling rain, the tops of the strong downdrafts in the lower levels of the stratiform region tend to be found near the level where the temperature is  $0^\circ\text{C}$ . Accordingly, the peak in mid-level convergence is also usually found near this melting layer, and this maximum can be intense (Mapes and Houze 1995). The net heating and cooling effect of the entire thunderstorm complex on the larger-scale environment is a superposition of the deep convective heating mode and the stratiform heating over cooling pattern. However, depending on the relative intensity and spatial extent of the convective and stratiform zones, the overall profile can predominantly resemble one mode or the other, or more of an equal blend of the two.

An important factor when considering the influence of a mesoscale heating source like an MCS on the surrounding environment is how those effects are communicated. As described by Mapes and Houze (1995), such heating anomalies excite outward propagating gravity waves, which create temperature perturbations as they move away from the systems. They note that while the storms generate waves at a wide range of frequencies and length scales, the slower-moving, high-frequency modes tend to cause direct vertical motion and heating responses within the MCS itself that work to counteract the impacts of those waves. On the other hand, the two lowest-wavenumber modes generally dominate the effects in the broader region outside of the system. The wavenumber-1 pattern is associated with deep subsidence throughout the troposphere, an associated deep positive temperature anomaly due to adiabatic warming, and is the fastest propagating wave, moving at about  $50 \text{ m s}^{-1}$  in the model used by Mapes and Houze (1995). The wavenumber-2 configuration comprised subsidence aloft overlying an upward displacement of the lower troposphere, connected with a warm anomaly at upper levels and a cool anomaly below, and moved at about half the speed of the wavenumber-1 mode,  $24 \text{ m s}^{-1}$  in the Mapes and Houze (1995) model. Of note, though, the mentioned model involved instantaneously imposing the two heating structures and did not include any later modification, so if additional diabatic heating altered the waves as they moved, their propagation speeds would be reduced and their distinct patterns would be spatially “smeared.”

### **b. West African Monsoon**

This brief overview of the West African monsoon (WAM) will largely follow the excellent review provided by Janicot et al. (2011). The WAM is a coupled system among the atmosphere, ocean, and land surface that is associated with precipitation over the continental

regions of West Africa during the boreal summer and a lack of rainfall during the winter. The mean annual cycle consists of a south-north-south transition of the latitude of maximum precipitation, which occurs in a series of relatively abrupt steps, and includes both active periods and lulls in convective activity. Specifically, the year begins with low rainfall amounts over the Gulf of Guinea and almost no rainfall on land during the winter, followed by an increase in precipitation near the coast during April and May. While the zone of rainfall gradually expands toward the north during the spring, there is a sudden northward shift of the precipitation band well inland at the end of June, which is referred to as the monsoon onset. Janicot et al. (2011) note that the mean date of this monsoon onset between 1968 and 2004 was 24 June, with a standard deviation of seven days. During July, August, and the first part of September, moist, southwesterly monsoon flow predominates at low levels in West Africa, transporting moisture from the Gulf of Guinea over the continent and feeding into heavy precipitation systems well into the Sahel region. After mid-September, the rainfall magnitude declines and the latitude of maximum precipitation begins to shift southward again, reaching the coast by the end of October. By late autumn, nearly all rainfall has moved over the Gulf of Guinea and amplitudes again become low.

The mechanisms of these meridional changes in precipitation through the seasonal cycle look to be connected to both oceanic and land surface processes. As described by Janicot et al. (2011), sea surface temperatures in the Gulf of Guinea reach their highest values in April, rapidly cool to their minimum levels in August, and then gradually warm again through the next April. The warming water temperatures at the beginning of the year are thought to contribute to the springtime increase in rainfall over the Gulf of Guinea, while the cooling through the spring and summer have been found in modeling studies to significantly intensify southerly winds over the

water that aid in pushing the maximum precipitation band inland. Through a series of positive feedbacks, the increased winds also help to further cool sea surface temperatures via upwelling and an augmentation of low-level stratus cloud development. The role of a thermal low-pressure zone over the Sahara desert in the summer also appears to be key in forcing the monsoon onset in June. This low intensifies around the time of the onset, a development that may be attributable to interactions with orography in northern Africa combined with the distribution of albedo and shortwave heating across the region, and which results in greater moisture advection inland, setting the stage for increased precipitation.

Rainfall within the West African monsoon regime varies on a number of sub-seasonal time scales. Janicot et al. (2011) point out that two particularly prominent time scales for summertime precipitation variability in West Africa exist at 10 to 25 day and 25 to 60 day periods. The 10 to 25 day period includes a quasi-biweekly oscillation comprising an out-of-phase relationship between rainfall in West Africa and in the western Atlantic Ocean and the Americas. A second mode of variability at the 10 to 25 day time range is associated with a propagating cyclonic circulation that appears over central Africa, moves north to the latitude of the Sahel, and then proceeds west toward the Atlantic Ocean. The fluctuations in precipitation amounts at the 25 to 60 day scale look to be connected to a combination of equatorial Kelvin and Rossby waves forced by the Madden-Julian Oscillation (MJO). As discussed further in Chapter 4, this prominent mode of low-latitude variability, first discerned by Madden and Julian (1972), involves a series of wind anomalies that travel eastward around the tropical belt over the course of a month or two. The MJO has been found to influence weather patterns and rainfall throughout both the tropics and the mid-latitudes, and appears to play a role in modulating the activity of the WAM as well. Eastward propagating equatorially trapped Kelvin waves also

significantly modulate convective activity in West Africa during the summer monsoon phase. These waves have a typical phase speed around  $15 \text{ m s}^{-1}$  and a periodicity of about six days, and the associated wind anomalies can enhance or weaken both moisture advection and low-level convergence, leading to a corresponding augmentation or suppression of precipitation systems.

### c. African Easterly Jet, Easterly Waves, and Convective Systems

Another prominent temporal mode of precipitation variability in West Africa is associated with African easterly waves (AEWs) and the African easterly jet (AEJ) along which those disturbances propagate. The AEJ is an important consequence of the meridional temperature gradient between the hot Sahara Desert and the relatively cooler coastal areas to the south. Figure 2.2 illustrates a schematic north-south cross section of the AEJ in boreal summer.

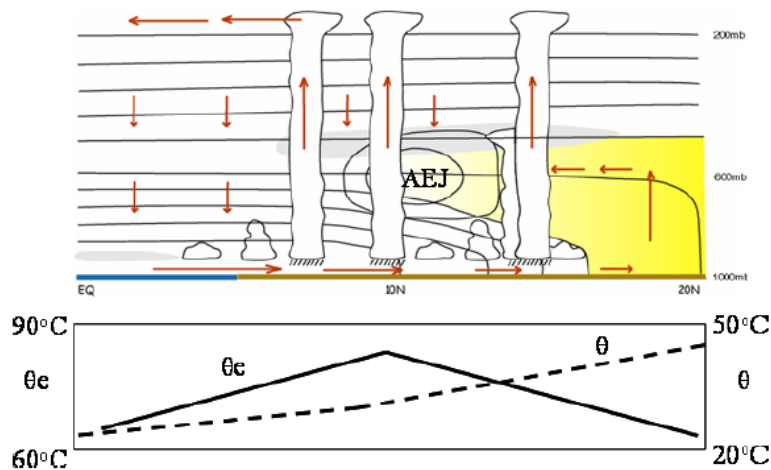


Figure 2. Schematic of the atmospheric circulation in the West African monsoon system during the boreal summer. Closed solid lines represent the isotachs of the African Easterly Jet (AEJ), which lies around 600 hPa. The red arrows show the thermally direct meridional monsoon circulation, and are typical of the time-mean winds in the peak monsoon season. This circulation will also be observed on many individual days, but there is strong variability over the diurnal cycle, and around mesoscale convective systems. The typical corresponding meridional variations in atmospheric boundary layer potential temperature ( $\theta$ ) and moist static energy equivalent potential temperature ( $\theta_e$ ) are given in the panel below. North of  $10^\circ\text{N}$ ,  $\theta_e$  starts to decrease while  $\theta$  continues to increase, due to the drying of the boundary layer north of the core of the ITCZ. Grey stippled shading represents peak rainfall and yellow shading indicates the location of the Saharan Air Layer (SAL). North of the AEJ, convective systems are highly intermittent, commonly with several days' interval between the occurrences of organised systems. (After the AMMA International Science Plan, 2005, adapted from Parker *et al.*, 2005). This figure is available in colour online at [www.interscience.wiley.com/journal/qj](http://www.interscience.wiley.com/journal/qj)

**Figure 2.2** Schematic meridional cross-section of the African easterly jet and associated potential temperature contours, monsoon flow vectors, and convective systems during boreal summer. From Lebel *et al.* (2010), Figure 2.

This figure shows, among other things, contours of potential temperature (increasing atmospheric temperature with increasing latitude in this region below the mid troposphere) and isotachs of the AEJ (centered near 600 hPa and 10° to 15° N latitude). Of note is the fact that this easterly wind maximum results in cyclonic shear to the south of the jet and anticyclonic shear to the north of the jet, which can yield a reversal of the sign of the gradient of absolute vorticity from the planetary norm (e.g. Nieto Ferreira and Schubert 1997). In the simplest terms, the AEJ can be thought of as a thermal wind balance response to the meridional temperature gradient, yielding an increase in easterly wind with height. However, as pointed out by Thorncroft and Blackburn (1999), this explanation does not account for the westerly shear above the jet core, where temperature gradients are weak. Instead, their study suggests that the AEJ is maintained by two diabatically forced meridional circulations – one associated with surface fluxes and dry convection occurring in the thermal low of the Sahara Desert and a second caused by deep moist convection in the inter-tropical convergence zone (ITCZ) south of the jet. Whatever the exact nature of the causes of the AEJ, its associated meridional temperature and vorticity gradients result in the observed jet being both barotropically and baroclinically unstable (Thorncroft and Blackburn 1999), setting the stage for easterly wave disturbances to grow in the area.

Many of the properties of these AEWs were documented by Reed et al. (1977), based on observations during the GATE field campaign. They found that the observed AEWs had a mean westward propagation speed of  $8 \text{ m s}^{-1}$ , wavelengths of about 2500 km, and periods around 3.5 days. These values compare reasonably well with the results of Burpee (1974), who used mainly surface observations to determine AEW wavelengths of 3100-3800 km and periods of 3.8-4.5 days. Reed et al. (1977) also noted that the wave axis had a distinct southwest-northeast tilt

around 700 hPa. This finding, combined with the cyclonic shear south of the AEJ, suggests that the waves were growing via barotropic conversion of the zonal kinetic energy of the AEJ into eddy kinetic energy of the AEWs. The same study described the disturbances, based on the perturbation wind field, as vertical below 700 hPa and sloped westward with height above 700 hPa near and south of the latitude of the jet. However, north of the jet, in the region of stronger meridional temperature gradients and baroclinicity, the systems sloped eastward with height at low to mid levels, suggesting baroclinic growth of the AEWs contributed in that area. Also in the Reed et al. paper, upward motion at mid levels was found to be strongest in advance of (west of) the AEW trough, with convective cloudiness and precipitation being enhanced in the same region. Correlations of the vertical velocity with temperature anomalies additionally suggested that the waves were supported, at least in part, by a baroclinic energy conversion.

Pytharoulis and Thorncroft (1999) extended the earlier work on typical AEW structures using radiosonde observations, model analysis data, and infrared satellite imagery. Their study indicated that AEWs comprise two distinct centers of vorticity – one center near and south of the AEJ at mid levels and a second center at low levels north of the jet latitude – that move together as a coherent system. They attributed the disturbances near and south of the jet to the influences of the meridional vorticity gradients discussed previously and found that they grew primarily via barotropic means. On the other hand, the low-level disturbances north of the jet were found mainly to be related to the strong low-level potential temperature gradients and low static stability in that area and their growth was attributed to baroclinic interactions. Some evidence of the disturbances near and south of the jet was also found at low levels, especially near the west coast of Africa, with latent heating suggested as a possible mechanism for extending the systems down through the atmosphere. This paper additionally noted that the low-level northern waves

tend to move southwestward after moving off the coast of Africa into the Atlantic, potentially yielding some sort of merger of the two centers of wave activity over the ocean. As would be expected from the typical meridional moisture gradients in West Africa, this study indicated that the southern centers of wave activity were associated with more deep convection than the northern centers.

These findings match well with results from Burpee (1974), who noted that easterly wave activity was maximized in “dry cyclones” near 20° N as well as a second area of disturbances around 5° to 10° N in the region of maximum seasonal mean rainfall. The Reed et al. (1977) study also found evidence of dual AEW circulation centers at the surface, mainly over land, which straddled the AEJ latitude. Figure 2.3 provides a more detailed representation of the geographical distribution of these two tracks of AEW disturbance activity. This plot shows contours of the eddy kinetic energy at 700 hPa (upper panel) and 950 hPa (lower panel) during July through September 1995 from bandpass-filtered winds for a typical AEW time scale of 2.5 to 5 day periods. Superimposed on these maps are dashed contours representing areas of strong easterly winds at 700 hPa, as a proxy for the AEJ. The upper panel clearly shows evidence of wave disturbance activity near and south of the AEJ at mid levels, while the lower panel illustrates the development of low-level disturbances north of the jet, with the band of eddies turning more southwestward near the African west coast.

Several recent studies have investigated the role of convection in the initiation, growth, and evolution of the previously discussed AEW structures. Easterly wave disturbances play a predominant role in determining the timing of convective activity in West Africa on multi-day time scales. In turn, well-organized MCSs, which account for the majority of rainfall in the Sahel region, can have important feedbacks on the development of the waves (Janicot et al.

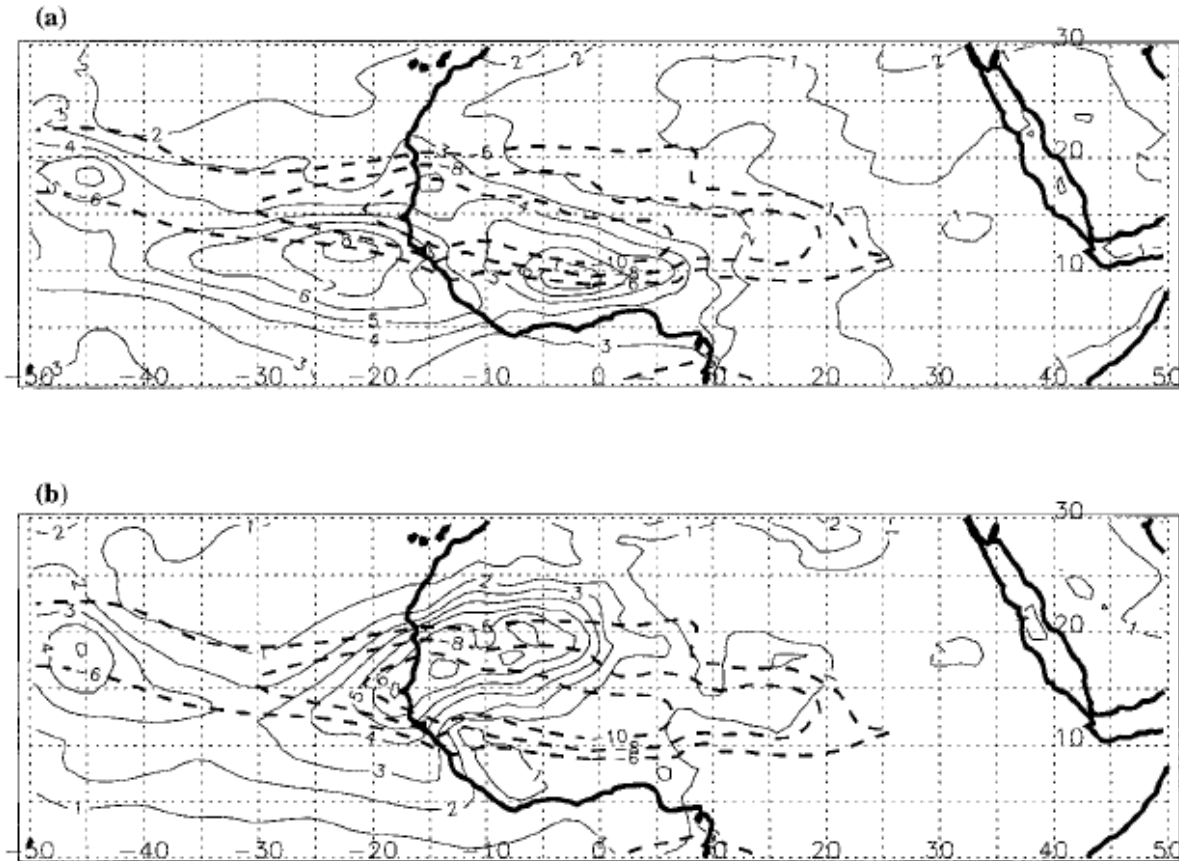


FIG. 10. Mean  $(u'^2 + v'^2)/2$  ( $\text{m}^2 \text{s}^{-2}$ ) averaged from Jul to Sep 1995 at (a) 700 mb and (b) 950 mb. Here  $u'$ ,  $v'$  are the 2.5–5-day bandpass-filtered zonal and meridional winds. Contour interval =  $1 \text{ m}^2 \text{ s}^{-2}$ . The bold dashed contours show regions where the mean easterly flow at 700 mb (from Jul to Sep 1995) was stronger than  $6 \text{ m s}^{-1}$ . Contour interval =  $2 \text{ m s}^{-1}$  (UKMO analysis data).

**Figure 2.3** Contours of mean eddy kinetic energy during July–September 1995 from bandpass-filtered winds for a typical AEW time scale of 2.5 to 5 day periods at 700 hPa (upper panel) and 950 hPa (lower panel). Dashed contours show regions where mean 700 hPa easterly flow is greater than  $6 \text{ m s}^{-1}$ , a proxy for the AEJ location. From Pytharoulis and Thorncroft (1999), Figure 10.

2011). Berry and Thorncroft (2005) analyzed a case study of a strong AEW in 2000 and combined their findings with previous work on these wave disturbances to derive a new conceptual model for the life cycle of an AEW. The discussion of this life cycle here is based on both the original paper by Berry and Thorncroft (2005) and an interpretation of their results by Janicot et al. (2011). Berry and Thorncroft determined that the genesis of AEWs is frequently

preceded by the triggering of several MCSs over elevated terrain in northeastern Africa, such as the Ethiopian Highlands and the Darfur region of Sudan. The authors surmise that the unstable basic state near the AEJ axis, when perturbed by a large region of convection developing over high terrain, results in the downstream development of baroclinically and barotropically growing AEWs. In particular, after the convection initiated in their case study scenario, it rapidly grew to cover a very large area, which represents a large region of heating, causing a dynamical response that significantly perturbed the wind field and that could result in AEW development.

Once these disturbances are in place, the next stage of the proposed life cycle begins when the synoptic-scale perturbation to the low-level potential temperature gradient interacts with a synoptic-scale perturbation of the AEJ-level potential vorticity (PV) strip over central and western North Africa. These perturbations are seen to move together across West Africa in an arrangement that suggests baroclinic development of the wave is taking place. Moreover, isolated PV maxima that are diabatically generated by deep convection are observed to develop within the zone of overall positive PV deviations. Interestingly, these PV maxima are found to remain intact for several days while the associated convection undergoes cycles of growth and decay on shorter time scales, and the PV maxima tend to be located just west of the AEW trough location, indicating that they may contribute to the westward propagation of the system.

The final phase of the AEW life cycle comes to fruition as the disturbance approaches the west coast of Africa. Significant convection frequently develops over the Guinea Highlands as the AEW advances toward the region, while the AEW begins to lose its baroclinic character as the perturbation to the low-level potential temperature gradient becomes distorted near the coast. PV anomalies associated with the Guinea Highlands convection can then interact with the westward moving PV maxima embedded within the AEW, resulting in the formation of a

merged column of high PV air near the coast that is deep, warm, moist, and has a near-surface cyclonic circulation. Convection continues to occur within this column, and as it moves off the coast and into the Atlantic, the organization of the convection about this merged warm-core structure can increase, setting the stage for tropical cyclogenesis.

Additional recent papers have investigated the relative contributions of convective heating and instabilities of the AEJ to the initiation of AEW disturbances. Thorncroft et al. (2008) used a primitive-equation model with a basic state similar to the conditions in tropical North Africa, forced by transient, localized latent heating with a variety of vertical structures. Despite the basic state in this model setup being linearly stable, when localized heating was imposed near the entrance region of the AEJ, a trough that propagated westward to the Atlantic coast was still generated. After five to seven days, a structure comprising a number of westward moving disturbances that greatly resembled AEWs became established in the model. This paper also found that the waves were most effectively generated by heating profiles that included vertical gradients in the low to mid troposphere, such as shallow convective and stratiform modes, as these structures created low-level circulations near the AEJ entrance region.

An alternative perspective on the role of convection in generating AEWs is provided by the work of Hsieh and Cook (2007). This paper used a regional climate model to study the energetics of AEWs, and they found that the important atmospheric response to upstream convective activity in producing AEW disturbances is through the creation of a more unstable AEJ. In particular, their work indicates that baroclinic overturning dominates as an energy source for AEWs, though barotropic conversion can approach the same magnitudes in the presence of concentrated ITCZ convection near the disturbance or strong shallow convection beneath the AEJ. Although these outcomes are based on regional model output and not actual

observations, the findings of this study are comparable to a previous energetics analysis of the region by Lau and Lau (1992) that used ECMWF operational analysis data.

Another regional climate model study that investigated the function of convection in controlling the development and character of AEWs was carried out by Sylla et al. (2011). This paper describes two RegCM3 simulations over West Africa in which a scheme of deep convection is turned on and off and compares the response of the AEJ and AEWs to the change. The results indicate that deep convective heating in the ITCZ region is necessary to generate an AEJ with realistic magnitude – the jet is too weak without convection. On the other hand, it was found that AEWs were still generated and propagated westward with the convection turned off, though they dissipated near the west coast of Africa and were much weaker than observed waves over land. Thus, the authors reached the conclusions that orographic friction and broad-scale near-surface moisture convergence may play a dominant role in initiating and growing AEWs, while convection strengthens the wave activity and promotes development of disturbances near the Atlantic coast.

Much research has been focused on examining the phase relationship between AEW troughs and ridges and thunderstorm systems in this region. Kiladis et al. (2006) determined the mean structure of AEWs over West Africa and the North Atlantic by projecting the distributions of dynamical quantities onto space-time filtered outgoing longwave radiation (OLR) data from satellites. Since OLR is an indicator of cloud top height, it is a proxy for the location and intensity of convective activity. The outcomes of their easterly wave space-and-time filtering indicate that over most of tropical North Africa and adjacent areas of the Atlantic Ocean, a majority of the OLR variability on sub-monthly scales derives from easterly waves, suggesting that AEW activity is the primary control on convective variance in these areas. Looking along

the 10° N parallel, located toward the south side of the typical AEJ position, they found that convection tended to occur within northerly flow (ahead of the AEW trough) east of 0° longitude, shifted into the wave trough farther west, and then moved into southerly flow (behind the AEW trough) as the waves moved offshore into the Atlantic. Conversely, along the 15° N parallel, located north of the AEJ axis, convection remained in the region of southerly flow throughout the trajectory of the AEW.

A similar study addressing the modulation of convective cloudiness by AEWs was performed by Duvel (1990), using ECMWF analyses and Meteosat cloud data. He finds that at 7.5° N latitude, south of the AEJ axis, convection is maximized just ahead of the AEW trough over both land and ocean. The author describes this phase relationship in terms of an increase in upward motion ahead of the trough due to diabatic heating; thus, this positioning is primarily a result of the dynamical feedback of the convection. At 17.5° N latitude, though, north of the jet position, convective activity tends to be concentrated in the zone of southerly flow east of (behind) the trough axis. At this latitude, particularly over land where it corresponds to the southern margins of the Sahara Desert, shallow dry convection predominates ahead of the trough while subsidence occurs above 500 hPa, yielding cloud-free conditions. On the other hand, the enhanced convection in the region of southerly flow is related to the increase in low to mid level moisture that this wind direction brings to the area.

Laing et al. (2008) looked at several years' worth of May-August infrared satellite imagery over northern tropical Africa to examine the propagation characteristics of cold cloud clusters, proxies for deep convection and rainfall. Their analyses identified MCSs in the region as spanning a mean distance of about 1000 km and lasting for about 25 hours on average. However, many of the studied precipitation events showed evidence of propagation over regional

to continental scales while the convection itself underwent cycles of growth and decay, consistent with the AEW life cycle model of Berry and Thorncroft (2005). Most of the rainfall episodes initiated in the lee of high terrain, also consistent with earlier findings, and then propagated westward with phase speeds of 10 to 20 m s<sup>-1</sup>. This speed is faster than the average motion of AEW disturbances, which was computed as 7.7 m s<sup>-1</sup> in this study, very close to the 8 m s<sup>-1</sup> mean found by Reed et al. (1977). Laing et al. (2008) also investigated the phasing of cold cloud streaks with AEW disturbances in the band of 10° W to 10° E longitude. Their results indicated that 35% of the cold cloud streaks occurred in southerly winds behind the trough, 24% occurred ahead of the trough, 10% within the trough, 7% within the ridge, 4.3% moved from behind the trough to ahead of the trough, and 19% of the cold cloud streaks were deemed not to be associated with AEWs.

A few recent papers have used both AMMA/NAMMA radar data and satellite products to investigate the effects of AEW disturbances on convective characteristics. Cifelli et al. (2010) found that while some West African MCSs looked to be unaffected by passing easterly waves, for those systems that were associated with an AEW, the most intense convection tended to occur ahead of the wave trough, consistent with dynamical forcing arguments connected to the wave structure. Guy et al. (2011) compared MCS features among a continental, a coastal, and a maritime site, and discerned that the presence of AEW activity generally enhanced MCS strength, as measured by such properties as total precipitation and vertical reflectivity profiles, at the continental and maritime sites. At the coastal location, the presence of AEW disturbances resulted in a greater number of large MCSs being observed, leading to increased stratiform precipitation, but with no obvious change in convective strength relative to when AEW activity was absent. Overall, the authors found that the differences between the various regions'

environmental states (e.g. vertical shear, convective available potential energy, the degree of synoptic forcing) resulted in more variability in the MCS characteristics than any changes induced by the presence or absence of easterly wave activity.

#### **d. Diurnal Cycle**

The mean diurnal cycle of precipitation in West Africa involves complex interactions among varying insolation, land vs. ocean differences, areas of high terrain, and long-distance propagation of well-organized thunderstorm systems. Laing et al. (2008) examined this diurnal cycle through the lens of cold cloud tops in infrared satellite data. Cold clouds are frequently used as a proxy for deep convection and heavy precipitation, since infrared observations are available over a much larger part of the Earth than is sampled by more direct rainfall measurement instruments like rain gauges and radars. However, it is important to keep in mind that this technique can underestimate precipitation associated with shallower atmospheric features like cumulus congestus clouds, and even within deep thunderstorms, the timing, intensity, and distribution of rainfall does not necessarily match the cloud top temperature pattern. This discrepancy will be investigated further in Chapter 5.

Keeping these limitations in mind, Laing et al. (2008) noted that deep convection in continental regions of West Africa initiates most often in the lee of zones of high topography. Over land, cold cloud coverage is at a minimum around noon, when mountainous regions stand out due to the developing thunderstorms located around them. The convective activity grows during the afternoon and individual storms merge into more organized systems, so that by evening, prominent areas of very cold cloud tops exist in the lee of most mountain ranges in the area. By midnight, the number of intense convective systems decreases, but for those that

persist, the cold cloud area continues to expand and the complexes are observed to propagate westward. In the early morning, thunderstorm intensity and areal coverage have decreased slightly from the peaks in the evening and overnight, but the cold cloud maxima continue to shift farther to the west, indicative of long-lived thunderstorm systems that last through the night. Focusing on the region of West Africa examined in this paper, Laing et al. (2008) mention that the Jos Plateau, Aïr Mountains, and Adamawa Highlands regularly trigger daytime convection. This longitude band is also influenced by propagating systems that arrive from the east after being triggered by the Darfur Mountains or Ethiopian Highlands, and which undergo cycles of decay and regeneration. West of the aforementioned terrain features, relatively flat relief prevails, and this lack of orographic triggering mechanisms means that rainfall from propagating systems that developed to the east comprises a large proportion of the total. For example, Laing et al. (2008) point out a nocturnal and early-morning peak in precipitation at Niamey, Niger associated with organized thunderstorm systems that were initiated by high topography to the east.

Over the ocean and near the coast, some other factors come into play when considering the diurnal cycle of rainfall. Sea/land breeze circulations, which involve onshore flow during the day and offshore flow at night, can influence the positioning and intensity of convective activity by varying the location of low-level convergence and moisture transport. In West Africa, these circulations are complicated by several areas of hilly to mountainous terrain located near the coastline, such as in Guinea, Togo, Nigeria, and Cameroon, where upslope daytime winds and downslope nighttime winds are superimposed on the flow. Laing et al. (2008) note that during the peak of the summer monsoon phase, the persistent southwesterly low-level monsoon flow tends to overwhelm the sea/land breeze cycle, though, removing that as an influence on the

diurnal variations. Johnson (2011) examined the time of day when precipitation reached its maximum rate using estimates from TRMM 3B42, a dataset based on infrared satellite readings that will be discussed in more detail in Chapters 3 and 5. On an annual mean basis, rainfall near the Gulf of Guinea coast peaks in mid to late morning, while areas farther offshore display a mix of morning to early afternoon maxima. Regions just inland from the coast have a late afternoon peak, similar to many tropical land areas. The Johnson (2011) analysis is also consistent with the work of Laing et al. (2008) in that westward propagation during the overnight hours away from zones of high terrain is apparent in much of West Africa. Near the topographic features, precipitation is maximized in mid to late afternoon, while areas just to the west show the greatest rainfall amounts during the evening, and locations proceeding farther to the west progress to nighttime and eventually early morning peaks. Notably, there is a dearth of late morning or noontime precipitation maxima in the inland parts of West Africa, which agrees with the daily minimum of cold cloud coverage found by Laing et al. (2008) during the 1100-1200 UTC period.

Another important factor in the diurnal cycle of West African weather is the nocturnal low-level jet. As described by Lothon et al. (2008) based on AMMA observations, a consistent low-level jet develops year round over continental West Africa, beginning early in the night, becoming firmly established by midnight, and peaking in intensity in the early morning hours. Specifically, that study found that the jet speed reached a maximum around 0500 UTC at an altitude of 400 m above ground level. During the dry season, which occupies most of the year in the Sahel zone, this jet is an arid northeasterly wind blowing off the Sahara desert, but during the wet summer monsoon phase, the jet comprises a moist southwesterly flow blowing from the ocean to inland areas. The formation of the low-level jet is tied to planetary boundary layer

processes, as the near-surface winds can intensify at night when the stable surface layer appears, the lower troposphere becomes decoupled from the ground, and the turbulent frictional force wanes. During the daytime, mixing in the boundary layer and moist convective activity both work to disrupt this widespread flow pattern, but also play key roles in distributing water vapor that has been transported inland by the nocturnal jet through a deeper layer of the atmosphere. Lothon et al. (2008) particularly emphasized the importance of the moist low-level jet during the summer monsoon regime in advecting moisture northward at night and of the dispersal of this humidity throughout the lower levels by the subsequent development of vigorous mixing connected with the daytime boundary layer. This moistening can help to precondition the environment for thunderstorm activity, while the nocturnal jet itself can aid the propagating convective systems that traverse this region overnight in maintaining their organization and producing heavy precipitation.

## CHAPTER 3

### DATA AND METHODS

#### a. Datasets

The primary dataset used in this work is a gridded analysis of zonal and meridional wind, temperature, geopotential height, and water vapor mixing ratio over West Africa during the AMMA Special Observing Periods (SOPs) in the summer of 2006, prepared by Paul Ciesielski. The analysis was created using all available radiosonde observations from AMMA stations on the African continent, supplemented by data from the ECMWF special AMMA reanalysis (Agustí-Panareda et al. 2010) in regions of sparse or missing sounding coverage. This dataset covers a spatial domain from  $0^{\circ}$  to  $20^{\circ}$  N latitude and  $25^{\circ}$  W to  $15^{\circ}$  E longitude at a horizontal resolution of one degree, and uses pressure as the vertical coordinate, extending from 1000 hPa to 50 hPa at 25 hPa intervals, with an additional analysis level at the surface. The time period of the analysis runs from 0000 UTC 1 June 2006 through 1800 UTC 30 September 2006, with a time resolution of six hours.

Figure 3.1 shows a map of the AMMA sounding network used in preparing the gridded analysis. The large black rectangle in the lower left corner of the map shows the spatial domain of the dataset, while the labeled circles portray the locations of the radiosonde release sites. The degree to which each circle is filled in black represents the completeness of the sounding record during the 1 June 2006 to 30 September 2006 period. The smaller quadrilateral and triangle between  $5^{\circ}$  N and  $20^{\circ}$  N latitude and  $5^{\circ}$  W and  $10^{\circ}$  E longitude outline the two enhanced budget array (EBA) regions, with the triangular region hereafter referred to as the EBA North area and the quadrilateral region as the EBA South area. The stations forming the corners of the EBAs

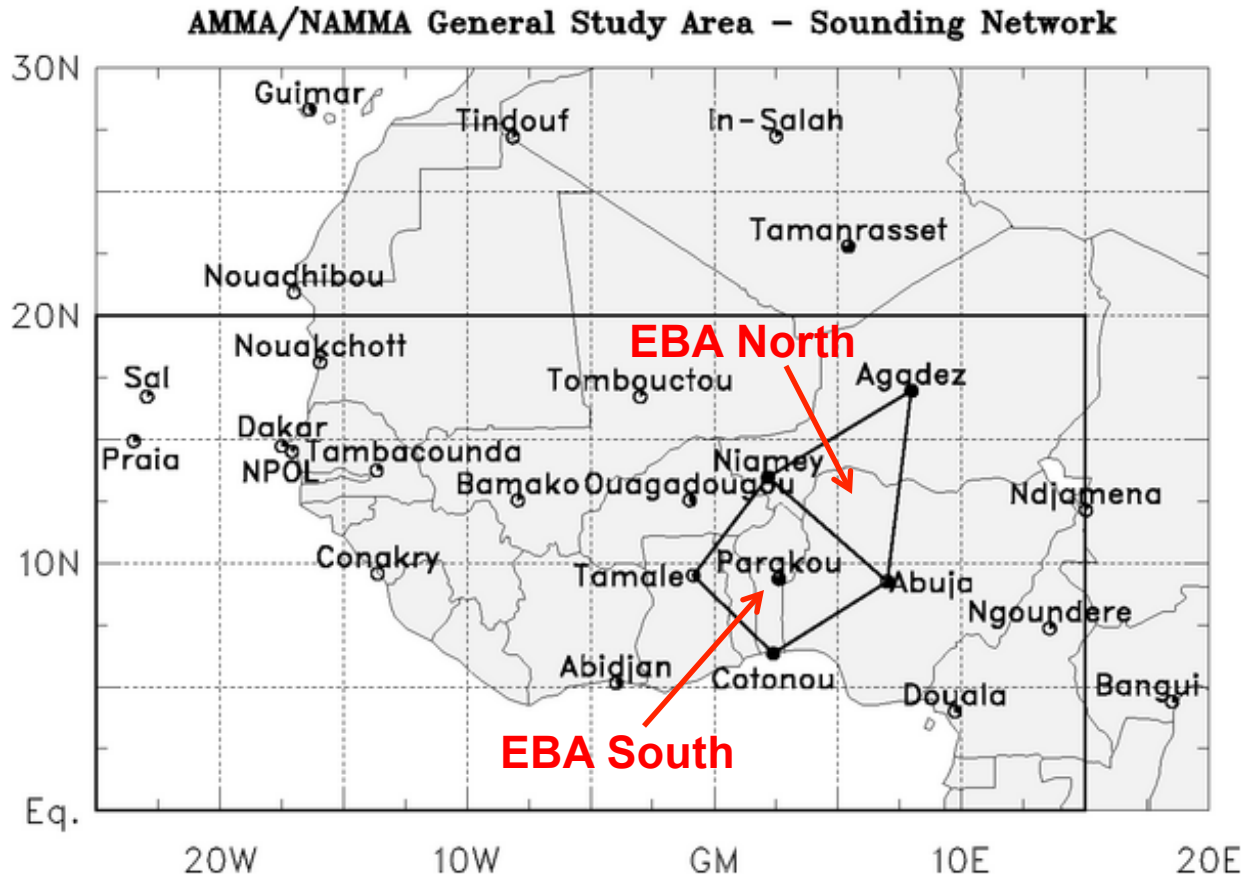


**Figure 3.1** Map of the sounding network in place during the summer of 2006 as part of the AMMA/NAMMA field project. The black rectangle bounded by the equator, 20° N latitude, 25° W longitude, and 15° E longitude represents the spatial domain of the AMMA radiosonde gridded analysis dataset. Each circle shows the location of a sounding launch site, with the fraction of the circle that is filled in black indicating the completeness of that station’s radiosonde record during the 1 June 2006 to 30 September 2006 period. The two enhanced budget array (EBA) regions are also labeled.

are those with the most complete sounding data record in the gridded analysis zone; thus, the analysis in this region is based the most heavily on the radiosonde data, with minimal influence from the ECMWF reanalysis. The remainder of this paper therefore focuses primarily on the EBA regions and the corresponding longitude band of 0° to 7° E, so that the results are developed to the greatest extent possible from the radiosonde observations themselves and the influence of any biases and peculiarities of the ECMWF modeling or reanalysis procedures are minimized. Of course, there are still some times with missing data even in the EBA regions, and

a lack of sounding stations in the northern and southern reaches of that longitude band means that some ECMWF reanalysis data will inevitably be included.

A couple of additional caveats must be considered when using this gridded dataset. First, the humidity measurements reported by the models of radiosondes used during the AMMA project are known to exhibit a daytime dry bias. These systematic errors have been partially corrected, but it is likely that the moisture values in the gridded dataset still generally represent an underestimate of the true conditions during the daytime. The other potential issue is that only sounding data from the regular AMMA stations located on the African continent were used in preparing the gridded analysis. Other AMMA/NAMMA observations, such as radiosondes released from islands and ships, dropsondes, and driftsondes, were not included in this dataset. However, the exclusion of these additional data sources should be of little impact in the relatively data-rich EBA regions.

Satellite products from the Tropical Rainfall Measuring Mission (TRMM) were also used in this work. The first such dataset is the TRMM 3B42 precipitation product. The 3B42 algorithm outputs merged-infrared satellite precipitation estimates, corrected using observations from the TRMM satellite (Huffman et al. 2007). More specifically, the TRMM Visible and Infrared Scanner and Microwave Imager data (TRMM products 1B01 and 2A12) and the monthly TRMM Combined Instrument calibration parameters (TRMM product 3B31) are used together to produce monthly calibration parameters linking infrared brightness temperature observations and TRMM satellite precipitation estimates. Then, these derived calibration values are applied to a merged-infrared dataset that includes observations from the Himawari, Geostationary Operational Environmental Satellite-East and West, Meteosat-7, Meteosat-5, and National Oceanic and Atmospheric Administration-12 satellites. The resulting TRMM-adjusted

merged-infrared precipitation estimates in the 3B42 product are provided on a 0.25-degree resolution horizontal grid, from 50° S to 50° N latitude and at all longitudes, and with a time resolution of three hours. This work uses 3B42 data from the same temporal and spatial domains as provided by the AMMA gridded dataset – 1 June 2006 to 30 September 2006, 0° to 20° N latitude, and 25° W to 15° E longitude.

The TRMM 3B42 product is intended as a “best estimate” precipitation dataset with continuous temporal and spatial coverage. Such a product is available due to the worldwide field of view provided by the constellation of geostationary infrared satellites used, whereas the TRMM satellite itself only observes any given location on the Earth’s surface approximately twice per day. However, an infrared-based precipitation estimate is less accurate than one that can be derived using all of the instruments available on the TRMM satellite together (precipitation radar, microwave imager, visible and infrared scanner, and so on). Huffman et al. (2007) point out that infrared brightness temperatures and precipitation are only well correlated at scales longer than about one day and larger than about 2.5 degrees of latitude and longitude.

In order to examine the relationship between TRMM precipitation estimates and the AMMA radiosonde analysis over sub-daily time periods, this work uses records from the TRMM precipitation feature database provided by the University of Utah Tropical Meteorology Group. This database is described in detail by Liu et al. (2008), but a summary of the procedure is provided here. First, observations from several TRMM satellite instruments (the Precipitation Radar (PR), TRMM Microwave Imager (TMI), Visible and Infrared Scanner (VIRS), and Lightning Imaging Sensor (LIS)) are collocated. Then, the collocated data are grouped into precipitation features (PFs) defined using a number of criteria (e.g. PR contiguous raining pixels, low VIRS brightness temperatures, low TMI polarization-corrected temperature). Rainfall

statistics are computed for each of the precipitation features, and finally, the statistics of the features are aggregated onto a one-degree horizontal resolution grid at monthly time resolution for eight three-hour periods through the diurnal cycle. This study examines Radar PF rainfall data, based on areas of surface precipitation as detected by the TRMM PR. Radar Projection PF rainfall data is also examined, which is based on the ground projection area of PR reflectivity greater than 20 dBZ at any level, thereby including surface rainfall, precipitation that evaporates before reaching the ground, and thick anvils aloft.

A few caveats with the interpretation of this dataset should be borne in mind. One potential issue with the gridded PF rainfall statistics is that all rainfall associated with a given precipitation feature is assigned to the grid box where the centroid of the feature lies. Thus, the actual spatial distribution of rainfall could be broader (extending over several grid boxes) than portrayed by this analysis (all precipitation shown in a single grid box). Another concern is that while both the TRMM 3B42 data and the University of Utah PF data are grouped into eight three-hour periods through the diurnal cycle, there is a 1.5-hour offset between the times used. Namely, the 3B42 product uses periods of 0130 UTC – 0430 UTC, 0430 UTC – 0730 UTC, etc. while the PF values are computed from 0000 UTC – 0300 UTC, 0300 UTC – 0600 UTC, etc. Additionally, the AMMA gridded sounding data are only available at four times daily – 0000 UTC, 0600 UTC, 1200 UTC, and 1800 UTC – times which fall in the center of TRMM 3B42 analysis periods but on the boundaries of University of Utah PF analysis periods. These timing offsets unavoidably complicate the inter-comparison of the different datasets. Lastly, as mentioned previously, the TRMM satellite only samples a given part of the Earth approximately twice per day. Thus, the PF data has temporal gaps and likely misses some precipitation events

that are included in the more continuous AMMA sounding and TRMM 3B42 products, which could account for some of the differences shown when contrasting these three datasets.

Another data source used in this study is radar rain rate estimates near Niamey, Niger, provided by Nick Guy. The MIT C-band Doppler weather radar was installed at the Niamey airport during the AMMA SOPs from July through September 2006 (Lebel et al. 2010). Dr. Guy used reflectivity observations from this radar system, applied an attenuation correction algorithm, interpolated the data to a 1-km Cartesian grid, and partitioned the grid points into convective and stratiform classifications. Then, measurements from a rain gauge network deployed in the Niamey area for the AMMA campaign were used to compute best-fit reflectivity vs. rain rate (Z-R) relationships separately for the convective and stratiform classifications. These Z-R relationships were applied to the radar observations to generate maps of 1-km elevation rain rate, every ten minutes (the volume repetition interval of the radar), over the scan domain of the radar – within a 158 km radius of the Niamey airport site (Guy et al. 2011). In the present work, these rainfall estimates were used as a selection aid during the qualitative evaluation of potential mesoscale convective system cases for further analysis, as discussed further in Chapter 6.

## **b. Methodology**

In order to compute the many derived kinematic and diabatic quantities (relative vorticity, divergence, vertical velocity, apparent heat source, apparent moisture sink, and so on) used in this study from the basic variables provided by the AMMA radiosonde gridded dataset, temporal and spatial derivatives and integrals of these measurements needed to be calculated. Since the present work deals with datasets using discrete time steps and spatial grids, finite

differencing procedures were required. Specifically, formulas with second-order accuracy – that is, estimates that yield an error that is on the order of the square of the temporal or spatial step size – were used in all cases. For first derivatives computed away from the “edges” of the time or space domain (where both previous and subsequent values of the function being differentiated were available), a centered difference was calculated. For such derivatives computed at the beginning or end of a time or space domain, the second-order one-sided difference formula was used, which includes the three points nearest the “edge” in the calculation. A special problem was encountered when computing vertical derivatives near the surface, where the usual non-correspondence of the surface level with one of the standard 25-hPa levels of the gridded dataset created unequal spacing between the points used in the finite differencing. A second-order one-sided difference formula for arbitrarily spaced points was derived by Fulton (2011), which was successfully used for evaluating such derivatives. Lastly, for computing integrals of quantities available only at discrete points, the trapezoidal rule was employed. This procedure estimates the integral of a function as the summation over all subintervals of one-half the sum of the values of the function at each end of each subinterval, multiplied by the spacing of those endpoints.

A few unique issues arise when attempting to compute a physically consistent flow field using individual data points from a sounding network, so special procedures were applied in calculating zonal and meridional winds, divergence, and vertical velocity. One analysis quirk was simply a result of the particular format of the AMMA radiosonde gridded dataset. Namely, the zonal and meridional winds were provided on a staggered grid. Although the horizontal grid spacing in both the zonal and meridional directions was a constant one degree of latitude/longitude for both variables, the zonal wind was defined at points offset a half-degree of longitude from the intersections of integer-numbered meridians. Similarly, the meridional wind

was defined at points offset a half-degree of latitude from the intersections of integer-numbered parallels. That is, the zonal wind grid included such points as ( $10^\circ$  N,  $0.5^\circ$  E), ( $10^\circ$  N,  $1.5^\circ$  E), ( $11^\circ$  N,  $1.5^\circ$  E), etc., while the meridional wind grid included such points as ( $10.5^\circ$  N,  $1^\circ$  E), ( $11.5^\circ$  N,  $1^\circ$  E), ( $11.5^\circ$  N,  $2^\circ$  E), etc. This peculiar grid setup was used to facilitate the calculation of divergence at points where integer-numbered parallels and meridians intersect. Computing the divergence at, say, ( $11^\circ$  N,  $1^\circ$  E) requires a derivative of the zonal wind along  $11^\circ$  N and a derivative of the meridional wind along  $1^\circ$  E, both of which can easily be computed using a second-order centered difference with zonal wind data points at ( $11^\circ$  N,  $0.5^\circ$  E) and ( $11^\circ$  N,  $1.5^\circ$  E), and meridional wind data points at ( $10.5^\circ$  N,  $1^\circ$  E), and ( $11.5^\circ$  N,  $1^\circ$  E). In the present study, the staggered wind grids were used as-is wherever zonal and meridional wind data at the same location were not required, and the divergence calculation used the same centered difference method just described. However, for computing quantities that entailed derivatives of the horizontal wind in other directions not directly compatible with the grid staggering (such as relative vorticity), the staggered wind values were linearly interpolated to a one-degree grid of points with integer-numbered latitude and longitude values.

Another known issue with calculating flow fields by objectively analyzing data from discrete observation points, as in a sounding network, is the possibility that the analysis procedure can generate spurious divergence. As detailed by Haertel (2002), techniques like multiquadric interpolation can yield unphysical dipoles in the analyzed divergence field centered on the vertices of a radiosonde station array. In fact, that article showed that such interpolation techniques could even cause divergence dipole patterns to appear using pseudo-observations sampled from an artificially constructed, purely non-divergent wind field! Of course, these erroneous divergence features will cause inaccuracies in any quantities derived from the affected

data, such as vertical motion, and thus heating and moistening rates as well. To attempt to correct these deficiencies in a gridded analysis, Haertel (2002) recommends creating a non-divergent approximation of the wind field, creating a pseudo-analysis of the non-divergent wind values, and subtracting the pseudo-analyzed divergence from the originally calculated divergence analysis. Then, a correction to the zonal and meridional wind values can be computed that matches with the rectified divergence data. These wind corrections were included with the AMMA radiosonde gridded dataset as provided by Paul Ciesielski, and in the present work, the correction factors were applied to the wind field prior to all other calculations.

The computation of vertical velocity also requires particular care to ensure that the values are as physically realistic as possible. The methodology and corrections to vertical velocity and divergence used in this study are based on guidance and computer code provided to the author by Paul Ciesielski, via personal communication. The vertical velocity at the surface level was calculated using “slope flows” – that is, based on the zonal and meridional wind values and the zonal and meridional topographic gradients at each grid point. Specifically, north-south and east-west gradients of the surface elevation at each grid point in the AMMA radiosonde analysis were computed via second-order centered differencing, with the raw elevation data being derived from a 10-minute resolution global topography dataset obtained from the National Center for Atmospheric Research. Then, the vertical velocity at the surface was computed as  $\omega_0 = -g\rho(u \frac{dz}{dx} + v \frac{dz}{dy})$ , where  $\omega_0$  represents the vertical velocity in pressure coordinates,  $g$  represents the acceleration due to gravity at the surface,  $\rho$  represents the air density at the surface,  $u$  and  $v$  represent the zonal and meridional wind at the surface, and  $\frac{dz}{dx}$  and  $\frac{dz}{dy}$  represent the zonal and meridional topographic gradients. This equation calculates the vertical motion associated with the horizontal winds blowing over a land surface that changes in elevation, and converts the

values into a pressure framework using the hydrostatic approximation. Then, the vertical velocity at all levels above the surface is derived by integrating the divergence profile from the surface upward with respect to pressure. As mentioned earlier, this integration using discrete data points was performed using the trapezoidal rule, so the vertical velocity at each level is computed using the vertical velocity at the level below, plus the pressure spacing between the levels, multiplied by one-half the sum of the divergence values at the two levels.

Unfortunately, most vertical velocity profiles derived in this manner tend to have unrealistic magnitudes by the time that the top of the analysis column is reached, due to accumulating errors in the divergence estimates (O'Brien 1970). By imposing a physically reasonable condition on the vertical velocity at some point high in the profile, though, corrections can be developed for the divergence and vertical velocity values that can reduce these discrepancies and restore mass balance to the analysis. In the present study, it was decided to impose an adiabatic condition at the tropopause to constrain the divergence and vertical motion estimates. It is recognized that substantial diabatic vertical motion can occur across the tropopause in the presence of deep convective towers and that stratosphere-troposphere exchange comprises an important contribution to atmospheric dynamics. However, in the context of a large-scale analysis such as the AMMA radiosonde gridded dataset, only a small fraction of a one-degree grid box would be covered by convective towers that may "overshoot" the tropopause, even within a larger mesoscale convective system that could itself cover much of a grid box. Considering this larger-scale tropical framework for the analysis, an adiabatic condition at the tropopause should at least comprise a constraint that is physically reasonable to first order and a helpful guide for minimizing errors in the divergence and vertical motion estimates.

In order to find the tropopause at each time step and grid point, the official WMO definition thereof was employed. Thus, the level identified as the tropopause was the lowest at which the temperature lapse rate decreased to  $2 \text{ K km}^{-1}$  or less and for which the average temperature lapse rate between the given level and all higher levels within 2 km did not exceed  $2 \text{ K km}^{-1}$  (WMO 2011). Then, the vertical velocity that corresponded to an adiabatic condition at the tropopause level (i.e. the Lagrangian or material time derivative of potential temperature equal to zero) was computed. The consequent divergence and vertical velocity correction factors were next calculated according to equations 7 and 8 of O'Brien (1970). More explicitly, a constant correction value of the difference between the adiabatic tropopause vertical motion value and the previously computed vertical motion value at the tropopause, divided by the pressure difference between the surface and the tropopause, was applied to all divergence values in the column. The correction factor added to each vertical velocity amount in the profile was the constant divergence correction quantity multiplied by the pressure difference between the surface and the level of that particular vertical velocity value. Essentially, this procedure applies a vertical velocity correction that increases linearly (in pressure coordinates) from zero at the surface to whatever amount is necessary at the tropopause to make the computed vertical velocity match that imposed by the adiabatic condition. The divergence correction is the constant value by which the divergence profile must be adjusted to yield this altered vertical velocity distribution. In other words, the correction of the "error" that accumulated through the integration of the divergence profile to produce a vertical velocity at the tropopause that did not match the adiabatic value is evenly distributed by this method through the column from the surface to the tropopause.

Upon using the above procedure with the AMMA radiosonde gridded dataset, it was found that the tropopause was diagnosed at the 100 hPa level for the vast majority of time steps and grid points. The outlined methods seemed to improve the estimates of divergence and vertical velocity between the surface and the tropopause level, and thus derived quantities such as heating and moistening rates looked more realistic and consistent as well. The process thus seems to have worked as intended, and it was used in this study as described. On the other hand, vertical motion and derived variables appeared unrealistic overall at the analysis levels above the tropopause, usually 75 hPa and 50 hPa. In particular, the magnitude of vertical motion seemed to be too large, and coupled with the strong stratification in the lower reaches of the stratosphere, this generated intense heating and cooling rates, even in the time mean, that appeared unphysical. This outcome should not be entirely unexpected, since the original methodology described by O'Brien (1970) expects the upper-level constraint to be applied at the top of the analysis column – the procedure was not intended to be extended beyond the point at which the boundary condition is imposed. Thus, while there is already some question about the physical realism of the diagnosed vertical velocities in the stratospheric portion of the soundings based on integrating divergence from the surface, adding the O'Brien (1970)-style corrections to these values may actually be a misapplication that only makes them less accurate. Since there is very low confidence in the integrity of the calculations at levels above the tropopause, and the tropopause level is at 100 hPa for almost all cases in this analysis, the investigations in subsequent chapters of this work only include data from the surface up to 100 hPa. This is not a major loss in any case, since it only involves discarding the uppermost two levels' worth of information and the focus of the present study is on tropospheric processes.

Additional moisture variables were calculated from the water vapor mixing ratio values provided in the AMMA radiosonde gridded dataset – namely, relative humidity and dewpoint temperature. To compute relative humidity at each time and location, water vapor pressure was first calculated from the water vapor mixing ratio and total air pressure data. Then, the saturation water vapor pressure for the given dry-bulb air temperature was determined. Equation 7 from Murphy and Koop (2005) was used for temperatures below 273.15 K, expressing the saturation water vapor pressure with respect to ice, and equation 10 from the same paper was used for temperatures at or above 273.15 K, expressing the saturation water vapor pressure with respect to liquid water. Finally, relative humidity was found by dividing the actual water vapor pressure value by the saturation water vapor pressure value for that temperature and multiplying the result by 100 percent. For the dewpoint temperature computation, water vapor pressure was again determined using the water vapor mixing ratio and total air pressure values. The calculation of dewpoint temperature, though, involves determining the temperature for which the saturation water vapor pressure value equals the observed water vapor pressure amount. Thus, equation 10 from Murphy and Koop (2005) was again used, but was rearranged to isolate one of the temperature variables and then solved iteratively. The water vapor pressure value was substituted into the saturation vapor pressure equation, the dry bulb air temperature was supplied as an initial guess for the dewpoint temperature, and the dewpoint temperature was computed iteratively using the rearranged Murphy and Koop (2005) equation 10 until the change from one repetition to the next was less than 0.0002 K. This final value was then used as the estimate of the dewpoint temperature for that data point.

Lastly, a procedure based on the work of Berry et al. (2007) was employed to objectively identify African easterly waves (AEWs) using the wind and vorticity fields from the AMMA

radiosonde gridded dataset. Computer code that guided the author's implementation of this procedure was provided via personal communication from Nick Guy, who in turn based his programs on work by Gareth Berry. The fundamental metric used to identify AEW trough and ridge axes in this method is lines where the advection of curvature vorticity equals zero – essentially, positive curvature vorticity advection is expected ahead of a trough axis and negative advection behind it, and vice versa for a ridge axis. Thus, the axes of trough and ridge features are located where these advection terms change sign. As Berry et al. (2007) point out, the location of a trough or ridge axis might normally be thought of as the position where the advection of the full vorticity is equal to zero, but this is only correct for idealized waves where the wind is a function of only a single horizontal direction. In the more realistic case, curvature vorticity must be used as the diagnostic variable because a large contribution to the total vorticity can come from horizontal shear, especially in the region of a strong jet, such as the African easterly jet near which the AEWs propagate.

It should be noted that the original technique outlined by Berry et al. (2007) used the non-divergent wind field and the matching stream function for these calculations, but the computational code for the procedure supplied by Gareth Berry, the lead author of that paper, was subsequently changed to use the “raw” wind field instead. Thus, the implementation in this work followed that later change and utilized the full zonal and meridional wind fields, not just the non-divergent component. Additionally, the Berry et al. (2007) study used wind and vorticity data at 700 hPa to diagnose wave axes, simply because that was the closest “standard atmospheric level” to the level of maximum AEW perturbations. Luckily, the AMMA radiosonde gridded analysis removes such data availability restrictions from the present work. Since the mid-level maximum of AEW activity occurs around 600 to 650 hPa, but with

appreciable variation above and below these typical pressures, mean winds and vorticity from the 550 hPa to 700 hPa layer were used in this paper as input to the AEW identification code.

As mentioned previously, the primary means of identifying AEW trough and ridge axes in this procedure is to find locations where the advection of curvature vorticity is equal to zero. However, not all such positions qualify as trough or ridge axes, so additional masking parameters were employed following Berry et al. (2007). First, to remove weak systems from the analysis, a trough axis was required to have a curvature vorticity value greater than  $0.5 \cdot 10^{-5} \text{ s}^{-1}$ , while a ridge axis was required to have a curvature vorticity less than  $-0.5 \cdot 10^{-5} \text{ s}^{-1}$ . Additionally, since easterly waves were the focus of this technique, the zonal wind speed in both trough and ridge axes was required to be negative. A third masking function was used to prevent local minima of curvature vorticity within a zone of positive curvature vorticity from being misidentified as troughs and to prevent local maxima of curvature vorticity within a zone of negative curvature vorticity from being misidentified as ridges. Namely, the negative advection of the advection of curvature vorticity must be greater than zero for a trough axis but less than zero for a ridge axis. While this quantity sounds complex, it is neatly shown in Figure 3 of Berry et al. (2007) that these inequalities select as troughs those axes of zero curvature vorticity advection identified within areas of positive curvature vorticity that are local maxima of curvature and not minima, and vice versa for the ridge axes. Finally, the individual points identified as being along trough and ridge axes were grouped together into whole axes, using a maximum permitted gap of two degrees of latitude or longitude between axis points, and only retaining axes containing four or more points, to focus on robust systems and eliminate spurious localized features identified as wave axes.

**CHAPTER 4**

**MEAN PROPERTIES AND VARIABILITY OF FLOW, DIABATIC PROFILES, AND  
PRECIPITATION DURING SUMMER 2006**

**a. West African Monsoon Cycle**

As discussed in Chapter 2, the West African monsoon comprises a seasonal cycle where rainfall is maximized near the coast during late spring, the most intense precipitation shifts northward toward the Sahel region during the summer, and precipitation gradually becomes weaker and shifts southward again at the end of the summer and into the autumn. The northward movement of intense precipitation associated with the monsoon tends to be relatively abrupt, is thought to be attributable to a combination of sea surface temperature forcing from the Gulf of Guinea and the effects of the thermal low over the Sahara, and normally occurs at the end of June (Janicot et al. 2011). During the AMMA SOP year of 2006, though, this monsoon onset occurred later than usual (well into July), although a healthy rainy season in the Sahel ensued after the late beginning (Lebel et al. 2010).

Figure 4.1 shows a time vs. latitude contour plot of daily-mean TRMM 3B42 precipitation rate data, averaged over the 0° to 7° E longitude band that includes the EBA regions and the best AMMA radiosonde coverage. The north-south seasonal cycle of precipitation is clearly evident in this plot, with the heaviest rainfall from June through the first week of July occurring over the Gulf of Guinea and along the coast (which varies between 4° N and 6° N latitude in this longitude band). By the middle of July, though, precipitation quickly increases from 10° N latitude and northward, and with the exception of a few major precipitation events that covered a large swath of latitudes at the beginning of August, in late August, and in early

# TRMM 3B42 Daily Mean Precipitation Rate

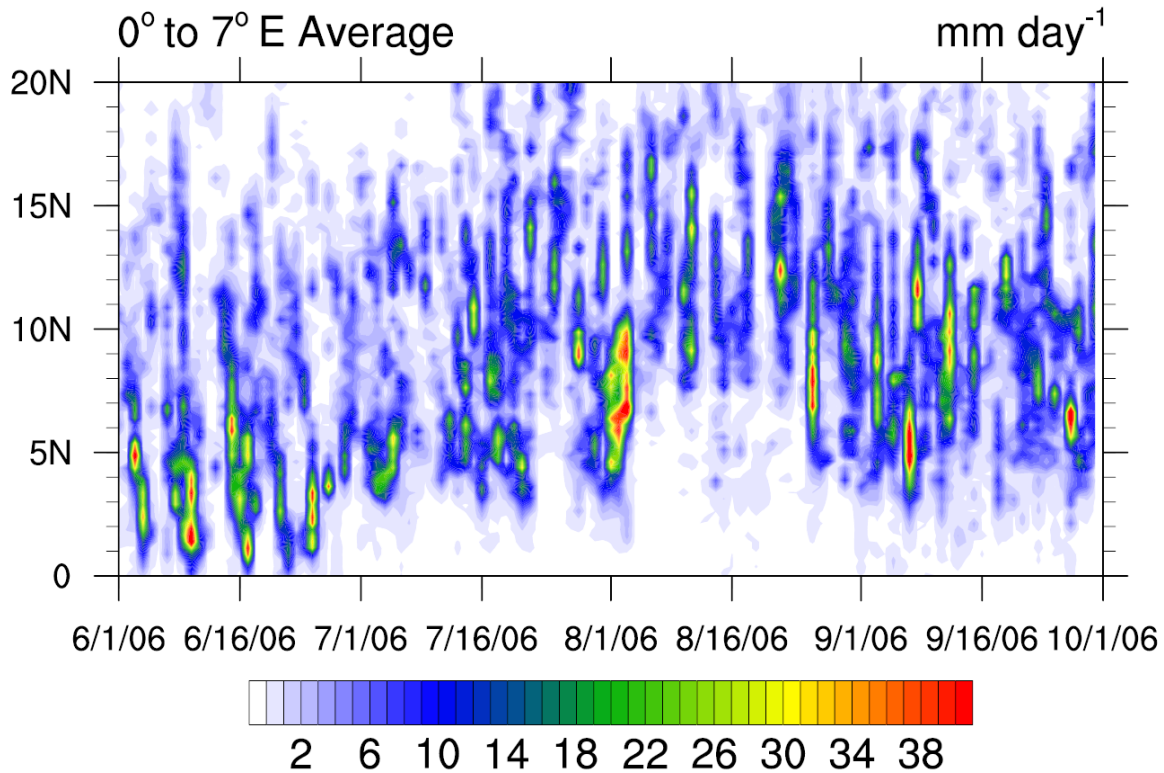


**Figure 4.1** Time vs. latitude contour plot of TRMM 3B42 daily mean precipitation rate data, in units of  $\text{mm day}^{-1}$ , averaged over the longitude band from  $0^\circ$  to  $7^\circ$  E. The lowest contour level is  $0.1 \text{ mm day}^{-1}$ , while the second lowest level is  $1 \text{ mm day}^{-1}$  and all subsequent levels have a  $1 \text{ mm day}^{-1}$  increment.

September, most of the heavier precipitation only occurs inland from mid July through the first part of September. Then, through the month of September, the most intense rainfall gradually shifts southward again, only occurring from near the coast to the very southern reaches of the Sahel region (to about  $12^\circ$  N) by the end of the month.

Another interesting feature evident in Figure 4.1 is that heavy rainfall events in this region do not generally occur every day. Looking at the plot, there is at least a one day gap between nearly all precipitation episodes at any given latitude, and in fact, the typical recurrence interval between rainfall maxima tends to be on the order of three to five days. This finding

matches well with the results of the modeling study of Laing et al. (2012), where long-lived precipitation episodes in the Sahel were only able to survive propagation away from high terrain once every two to three days. Laing et al. (2012) attributed this periodicity to strong stabilization, residual cloudiness, and reduced vertical shear in the wake of previous thunderstorm systems, leaving an inhospitable environment for subsequent convection until a few days had passed and the atmosphere had time to “recover.” Additionally, a three to five day periodicity corresponds very well with the typical time scale for the passage of African easterly waves, as detailed in Chapter 2. As also discussed in that chapter, feedbacks between convective activity and easterly wave development are numerous, so it is likely not coincidental that these phenomena repeat on similar time scales in this region, or that the usual periodicity of the precipitation events illustrated in Figure 4.1 fits well with both of them.

A longer time scale of precipitation variability in West Africa is associated with the Madden-Julian Oscillation (MJO), an intraseasonal fluctuation with a 25 to 60 day periodicity. As first described by Madden and Julian (1972), this pattern consists of a disturbance in atmospheric pressure, lower and upper tropospheric zonal winds and circulations, moisture, and precipitation that travels eastward around the tropical belt during a period of a month or two. MJO events are often thought of as initiating over the Indian Ocean, then propagating eastward across the Maritime Continent and the western Pacific Ocean. While the prominent signal in precipitation and cold cloudiness tends to diminish as the system moves into the central and eastern Pacific Ocean, the wind anomalies in particular often complete a full global circuit of the tropics. The variations associated with an MJO event can continue to influence weather conditions in the tropical portions of the Americas, the Atlantic Ocean, and Africa even after the

distinctive convective indications have decayed over the Pacific, and may even interact with conditions in mid-latitude areas as well.

A common method for visualizing the state of the MJO is using the Real-time Multivariate MJO index developed by Wheeler and Hendon (2004). This procedure is based on projecting observed conditions onto two empirical orthogonal functions derived from tropically averaged 200-hPa zonal wind, 850-hPa zonal wind, and outgoing longwave radiation that represent the patterns of variability associated with the MJO. The principal component time series associated with these projections can then be plotted on a Cartesian graph, in which case the radial distance from the origin of the graph represents the magnitude of the MJO signal, while the azimuthal angle about the center of the plot indicates the longitudinal phase position of the MJO event. Such a plot for June through September 2006 is shown in Figure 4.2. Again, the distance of the line in this figure from the center of the graph represents the strength of the MJO disturbance, where conditions outside of the black unit circle in the middle of the plot are considered to represent a robust MJO episode. The azimuthal position of the line illustrates the location in the tropics where the convective maximum phase of the MJO is found, with the sector labeled “1” in the lower left corner of the plot corresponding to Africa. Thus, at times where the line is outside of the central unit circle and located within the phase “1” sector of the graph, the MJO is supportive of enhanced precipitation activity over tropical Africa.

According to Figure 4.2, this condition is met for the first two weeks of June, the end of July, the end of August, and the beginning of September. Comparing these time frames with the time series of rainfall in Figure 4.1, there looks to be quite good correspondence. Several major heavy precipitation events took place during the first half of June, while there was a relative lull in rainfall from the end of June through most of July. Intense convection flares up again briefly

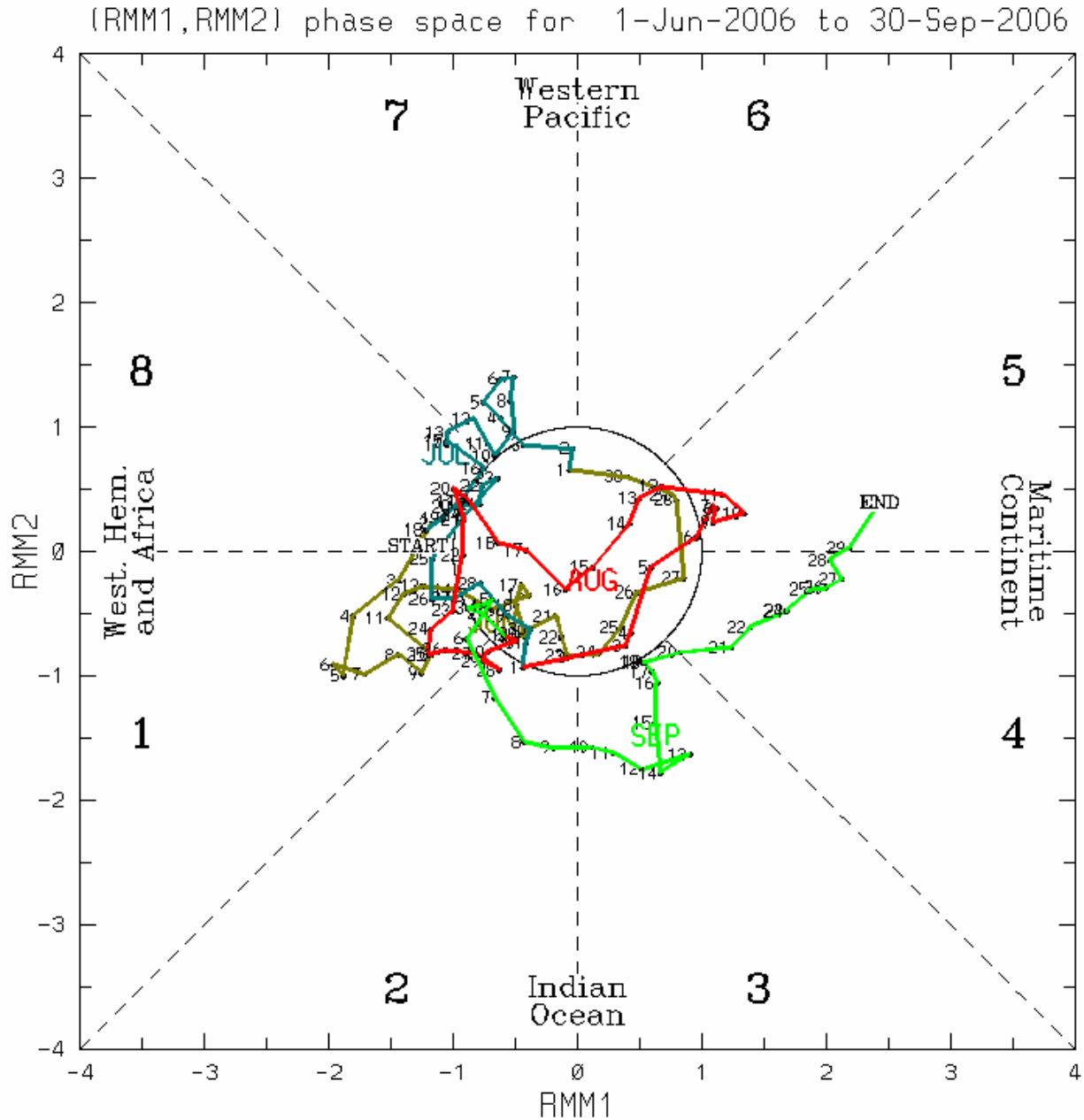


**Figure 4.2** Phase space plot of the Wheeler and Hendon (2004) Real-time Multivariate MJO index for June through September 2006. Computed by Dr. Matthew Wheeler, at the Center for Australian Weather and Climate Research, <http://cawcr.gov.au/staff/mwheeler/maproom/RMM/>. Figure available online at <http://cawcr.gov.au/staff/mwheeler/maproom/RMM/phasediag/pd.2006.6.1.gif>.

around the end of July and very beginning of August, followed by another decrease toward the middle of August. The end of August and the start of September were characterized by several

heavy precipitation events, while conditions quieted down somewhat into the middle of September. Of course, correlation does not imply causation, so these similarities should not be construed to guarantee a cause-and-effect relationship, but there does appear to be a substantial modulation of precipitation activity across this region of West Africa that matches very well with the diagnosed MJO signal. There are also many other factors and feedbacks influencing rainfall in this region, so not every increase or decrease matches with a change in the MJO, but these results do suggest that the MJO could be a predominant mechanism working to adjust precipitation intensity in the study area on longer intraseasonal time scales.

#### **b. EBA-Average Conditions**

Figure 4.3 shows time series plots of the daily-mean vertical profile of relative vorticity, computed from the AMMA radiosonde gridded dataset, averaged over the EBA North and EBA South regions. In the northern region, the vertical profile is dominated by negative relative vorticity during June, though with some maxima of positive relative vorticity at low levels. After the West African monsoon onset in early July, though, the vertical distribution of vorticity changes dramatically. At that time, the low levels tend to have negative relative vorticity, while the mid levels are characterized by a predominance of positive relative vorticity, with maxima and minima of vorticity occurring every few days. The upper levels continue to have generally negative relative vorticity. In the southern region, most of June has negative low-level relative vorticity, positive mid-level relative vorticity, and negative relative vorticity at upper levels, though magnitudes tend to be weak. Conditions in the southern region also change upon the monsoon onset in July, with generally low values of both positive and negative relative vorticity at low levels, and much stronger positive relative vorticity values at mid levels that pulsate at a

# Daily-Mean EBA-Average Relative Vorticity ( $10^{-5} \text{ s}^{-1}$ )

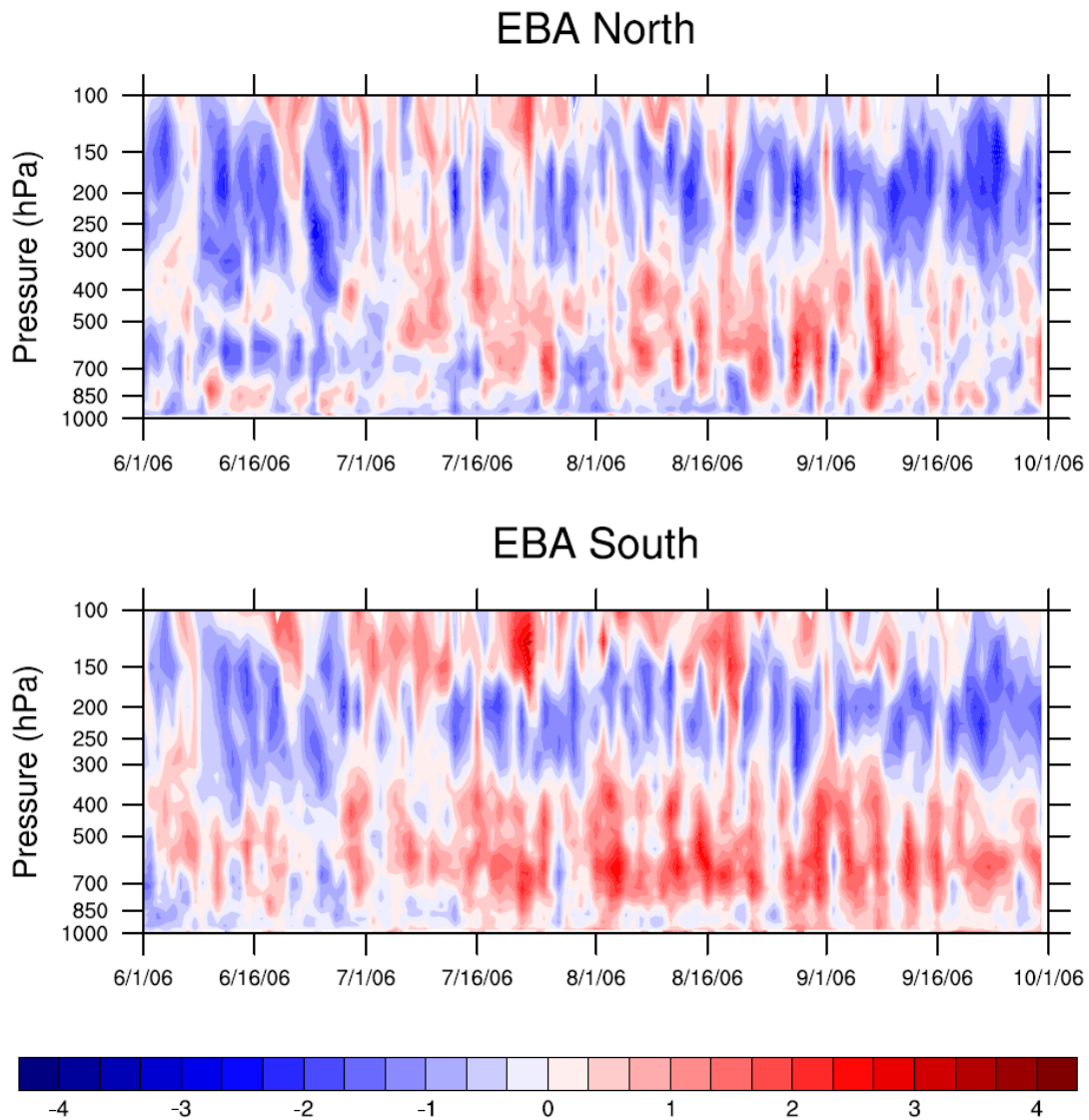


**Figure 4.3** Time vs. pressure contour plots of daily mean relative vorticity, in units of  $10^{-5} \text{ s}^{-1}$ , from the AMMA radiosonde gridded analysis, spatially averaged over the EBA regions.

time scale of a few days, similar to the EBA North area. The upper troposphere remains dominated by negative relative vorticity in the southern region. In both EBA zones, the magnitudes of the vorticity fluctuations begin to diminish in the second half of September, as the summer phase of the monsoon wanes.

The low-level changes in vorticity in the EBA regions look to be connected with the seasonal change in the position of the moist, southwesterly monsoon flow off the Gulf of Guinea. In June, when precipitation maximizes near the coast, the southwesterly flow is just beginning to work inland, but has not yet reached the Sahel latitudes, while the boreal summer easterly flow is starting to develop closer to the equator. As the monsoon flow is partially encroaching on the southern EBA region, the combination of this wind pattern with easterlies to the south yields some episodes of negative relative vorticity, though the weak magnitudes shown in Figure 4.3 suggest that the flow over this region remains variable at this time. On the other hand, the maximum monsoon flow is still south of the northern EBA area in June, setting up that region for positive relative vorticity episodes, as shown in the plot. During the peak summer monsoon season, though, the strongest southwesterly flow moves well northward over land, to around  $14^{\circ}$  N to  $15^{\circ}$  N latitude at the longitudes of the EBA regions. This places much of the northern region to the south of the most intense low-level southwesterly flow, and thus in a zone of negative relative vorticity, as observed. The southern region is now located away from the strongest monsoon flow, so the mean low-level relative vorticity magnitude in that area becomes low, though some positive and negative relative vorticity events do occur as the pattern shifts northward and southward at short time scales during the summer.

The upper level relative vorticity pattern throughout the time domain of this study is strongly related to the tropical easterly jet that is found in this region. This feature (which is clearly evident in Figure 4.11, to be discussed later in this chapter), maximizes in intensity at around 200 hPa between  $5^{\circ}$  N and  $10^{\circ}$  N latitude, and extends northward and upward, reaching the 100 hPa level around  $14^{\circ}$  N latitude. Thus, both the northern and southern EBA regions are on the anticyclonic side of the jet around 200 hPa, accounting for the predominance of negative

relative vorticity at that pressure. However, the southern region tends to be on the south (cyclonic) side of the jet at the 100 hPa level, and the northern region is also sometimes positioned south of the jet at that level as it meanders through the atmosphere, explaining the positive relative vorticity values often seen at the top edges of Figure 4.3.

The relative vorticity pattern at mid levels during the peak summer monsoon phase, in both EBA regions, looks to be strongly tied to easterly wave activity along the African easterly jet. As discussed in Chapter 2, this mid level jet is associated with the strong baroclinicity in the Sahel region as the moist, cooler monsoon flow meets dry, warmer air from the north under the influence of the Saharan heat low. Easterly wave disturbances propagate westward along this feature with a time scale of three to five days, and are intimately connected with convective activity through numerous feedback mechanisms. In both EBA regions, the maxima in mid level relative vorticity also appear to have a three to five day period throughout the peak monsoon phase of July through mid-September, suggesting that easterly wave activity likely predominates the mid level vorticity fluctuations in this region during the summer. It is also interesting to note that between maxima in positive relative vorticity associated with easterly waves, the mid level relative vorticity in the northern region is more likely to be negative, while it is usually close to zero or still weakly positive in the southern region. This can be attributed to the mean position of the African easterly jet at this time of year – the jet tends to be located near the center of the northern region, so meridional deflections of the flow due to easterly wave passage can place that EBA zone on either the cyclonic or the anticyclonic side of the jet. The wind maximum tends to be to the north of the southern region, though, so only a major excursion to the south places that area on the anticyclonic side of the jet.

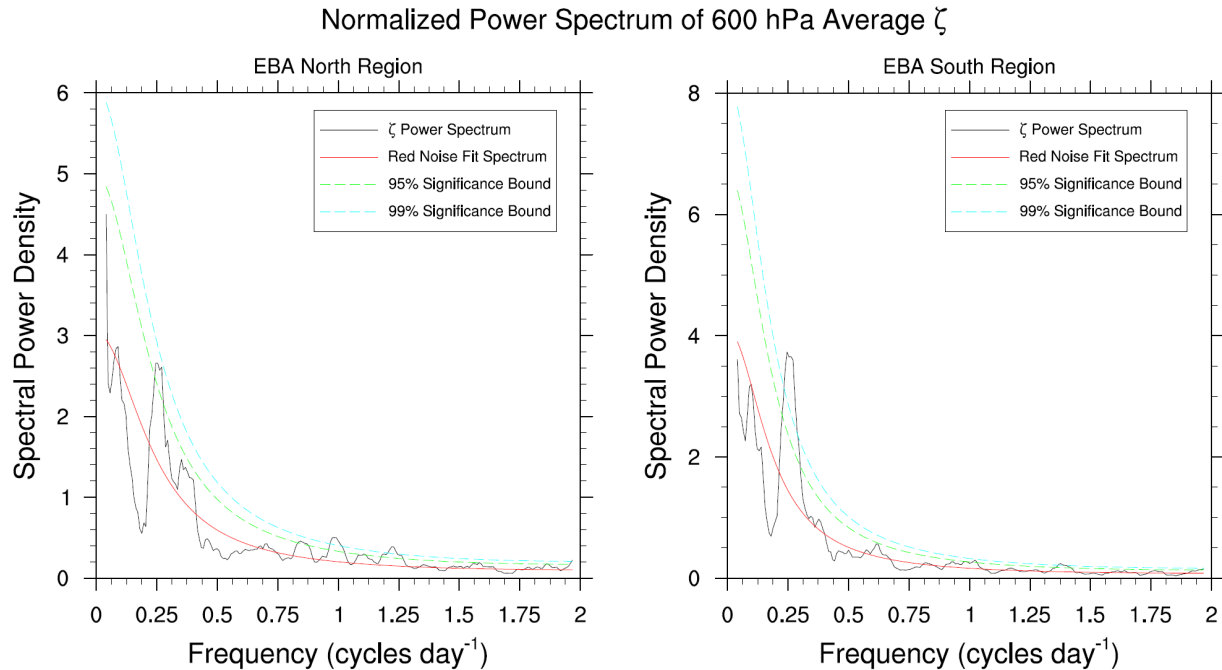


**Figure 4.4** Power spectra computed from time series analysis of 600 hPa relative vorticity averaged over the two EBA regions, using data from 1 June 2006 through 30 September 2006. The spectra have been normalized so that the area under each spectrum equals one. The black curves show the relative vorticity power spectra, the red curves show the spectra of red noise fits to the time series, and the dashed green and cyan curves show the significance bounds of confidence intervals at the 95% and 99% levels, respectively, for values that can be considered significantly different from the red noise spectra.

As a confirmation of the predominance of a three to five day time scale in mid level relative vorticity variability in this region, Figure 4.4 shows the results of spectral analysis of the time series of 600 hPa relative vorticity averaged over the EBA regions. The power spectra have been normalized so that the area under each spectrum is equal to one, and each plot also shows the spectrum of a red noise fit based on the lag-one autocorrelation of each time series, as a “null” comparison spectrum. The plots additionally show the bounds for confidence intervals of what spectral power density values can be considered significantly different from the red noise spectrum at 95% and 99% confidence levels. In both the northern and southern regions, there is a notable peak in the spectral power at frequencies of about 0.22 to 0.31 cycles day<sup>-1</sup>, which correspond to periods of 3.2 to 4.5 days. In the EBA North region, this peak is significant at the

95% confidence level, though not the 99% confidence level, while in the EBA South region, the peak is significant at the 99% confidence level. Thus, the African easterly wave time scale does indeed seem to be a dominant mode of mid level relative vorticity variability in the EBA regions. It is also interesting to note that both power spectra show peaks around the diurnal time scale as well, though the peak in the northern region is statistically significant while the southern region peak is not. The diurnal cycle in this area will be examined in much greater depth in Chapter 5 of this work.

While the variations in West Africa between the pre-monsoon conditions in June and the peak of the summer phase of the monsoon during July through September are interesting and worthy of the extensive study they have received in the literature, the focus of much of the remainder of this work will be on variability at shorter time scales within the primary monsoon season. Therefore, most of the remaining plots later in this chapter and in subsequent chapters represent averages over the period from 1 July 2006 through 15 September 2006. These particular limits were chosen based on the approximate timing of when substantial mid level positive relative vorticity was present in Figure 4.3, particularly in the EBA North region, where significant easterly wave activity and the majority of annual precipitation only occur during the heart of the summer monsoon season. Since the northward shift of rainfall is not absolute and some amount of precipitation occurs at most all latitudes both during and outside of the peak summer monsoon period, any selection of particular dates to capture the most convectively active period in the EBA regions must be somewhat arbitrary. However, this time frame does seem to contain the core of the summer monsoon phase, and will be used extensively later in this paper.

Figure 4.5 shows time series plots of the daily-mean vertical profile of the  $Q_1$  apparent heat source, computed from the AMMA radiosonde gridded dataset, averaged over the EBA North and EBA South regions. These graphs show a predominance of positive  $Q_1$  at low levels

## Daily-Mean EBA-Average Apparent Heat Source ( $K \text{ day}^{-1}$ )

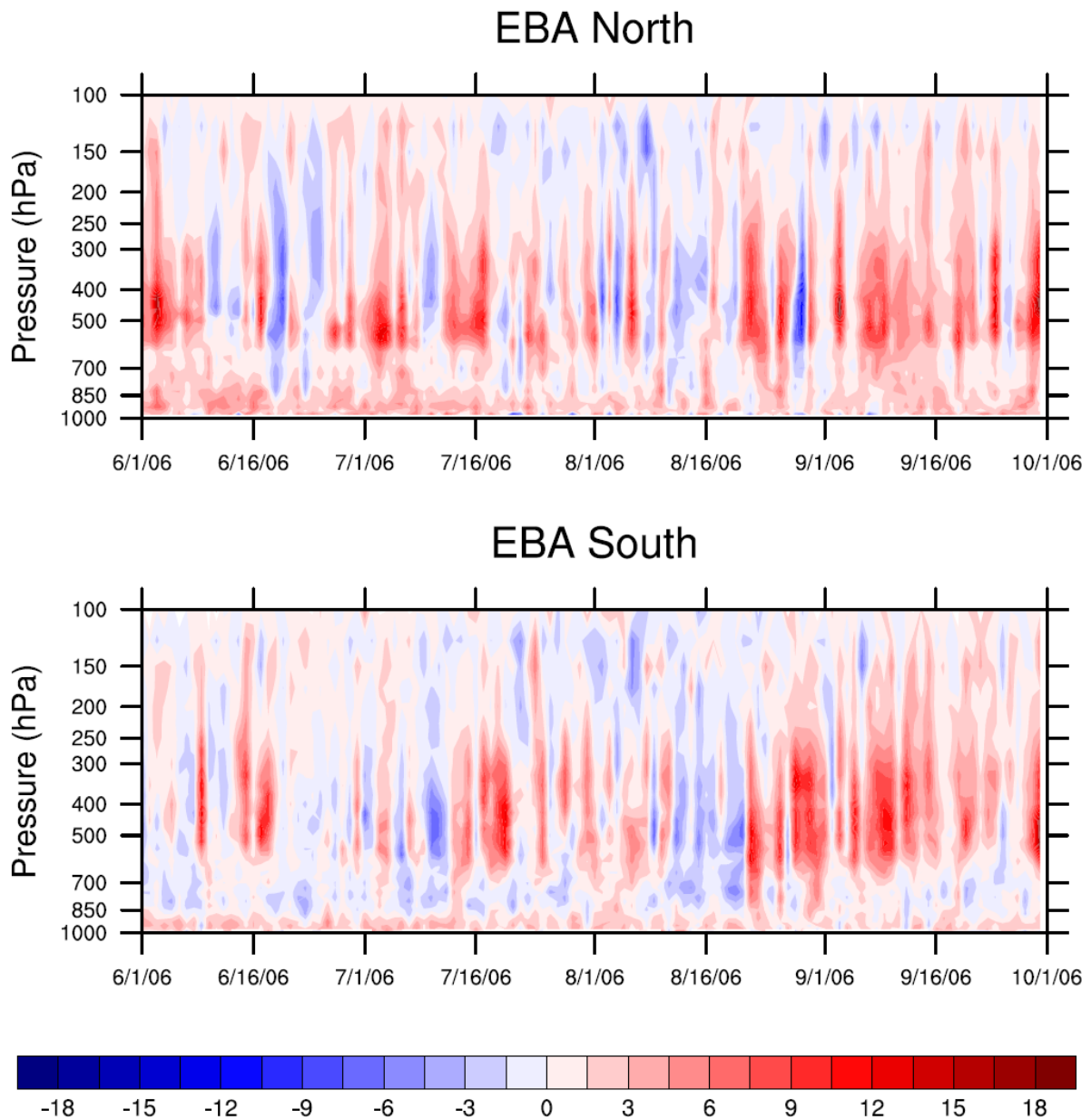


**Figure 4.5** Time vs. pressure contour plots of daily mean  $Q_1$  apparent heat source, in units of  $K \text{ day}^{-1}$ , from the AMMA radiosonde gridded analysis, spatially averaged over the EBA regions.

in both areas, though the layer of heating appears deeper in the northern region than in the southern region, and within the northern region, looks to be deeper in June during the pre-monsoon phase and shallower later in the summer. Between about 850 hPa and 600 hPa,  $Q_1$  generally has low magnitude, with a substantial number of cooling episodes, particularly in the EBA South zone. Above 600 hPa, the magnitudes of the  $Q_1$  values sharply increase, with many deep heating and cooling events. At upper levels,  $Q_1$  generally becomes weak, though the stronger heating and cooling peaks tend to extend higher in the atmosphere in the northern region than in the southern region. Of note is that the mid to upper level heating and cooling maxima appear to have a similar three to five day time scale to the relative vorticity maxima discussed previously. This suggests that these  $Q_1$  fluctuations are also tied to the passage of easterly waves across the region, likely through the coupling of convective activity, which is both forced by and helps to reinforce the waves, and tends to be associated with large magnitudes of heating and cooling through the troposphere.

The low level heating maximum is likely associated with the daytime development and growth of the planetary boundary layer, as solar radiation warms the Earth and causes heating and mixing of the lower troposphere. (The analysis of the diurnal cycle of  $Q_1$  in Chapter 5 will show that the mean magnitude of daytime heating in the boundary layer is greater than that of nighttime cooling, thereby yielding a positive low level daily mean  $Q_1$  value for most days.) The fact that this layer of heating is deeper in the northern region than the southern region also matches well with the hotter and drier conditions in the EBA North zone, which promote the formation of very deep, well-mixed boundary layers in that area. The deeper low level heating during the pre-monsoon period is consistent with reduced cloudiness and precipitation at that time, and thus stronger sensible heat fluxes as well, compared to later in the summer when

rainfall increases. The fact that upper level peaks in heating extend to higher levels in the northern region than the southern region indicates that the warmer and less cloudy conditions in the EBA North area may also contribute to more intense deep convective updrafts that reach higher altitudes there compared to the southern zone. (This pattern is suggested by analysis of the divergence profile as well, as shown later in this chapter and in Chapter 5.)

The relatively low magnitudes of  $Q_1$  values at mid levels below about 600 hPa compared to the sharp increase in magnitudes above that level comprise an interesting feature deserving of further investigation. For comparison, Figure 4.6 shows time series plots of the daily-mean vertical profile of the vertical velocity, computed from the AMMA radiosonde gridded dataset, averaged over the EBA North and EBA South regions. Notably, there does not appear to be any distinct change in vertical motion near the 600 hPa level. Since there is no substantial vertical velocity variation near 600 hPa, the change in  $Q_1$  at that height must be associated with differences in the thermal profile above and below that layer. Other aspects of the vertical velocity plot worth mentioning include, once again, the variability between maxima of upward and downward motion occurring on a three to five day time scale, suggesting that vertical velocity is also predominantly controlled by the passage of easterly waves. This variability can be attributed to both the larger scale influences of transitory troughs and ridges themselves as well as the smaller scale vertical motion impacts of the convective activity with which they are associated. There is also a prominent pattern of low level rising motion in the northern region during June, connected with the very deep, hot daytime boundary layers that form in that area during the pre-monsoon phase, while low level sinking motion is more common in the southern region, suggesting that convective downdrafts may play important roles as well. Overall, the

profile of vertical velocity appears much more homogeneous throughout the column than do the relative vorticity or apparent heat source structures.

## Daily-Mean EBA-Average Vertical Velocity ( $\text{hPa hr}^{-1}$ )

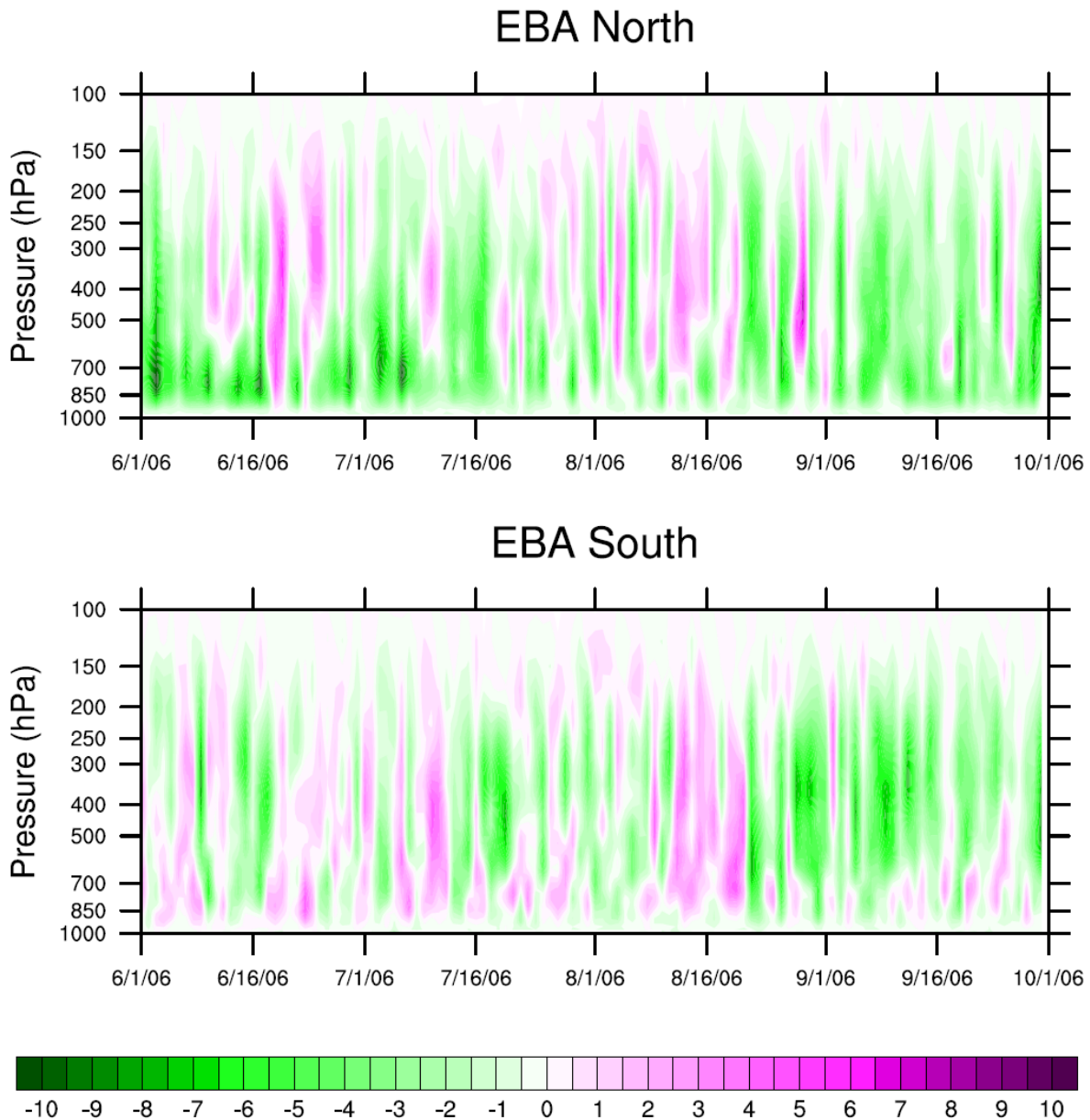


**Figure 4.6** Time vs. pressure contour plots of daily mean vertical velocity, in units of  $\text{hPa hr}^{-1}$ , from the AMMA radiosonde gridded analysis, spatially averaged over the EBA regions. Since the vertical velocity values are in pressure units, negative values (green colors) represent ascending motion, while positive values (magenta colors) represent descending motion.

To examine the possibility that a change in the thermal profile is responsible for the change in  $Q_1$  magnitude observed around 600 hPa, Figure 4.7 shows the time mean vertical profiles of temperature and dewpoint temperature, averaged over the EBA North and EBA South regions from 1 July to 15 September 2006, plotted on a skew-T/log-p diagram. In fact, these time mean profiles do show a distinct change in stability, marked by the change in the slope of the temperature curves, around 575 to 600 hPa. The less stable conditions below that layer (less of a change in potential temperature per change in pressure) would tend to yield a smaller  $Q_1$  magnitude for a given vertical velocity value. The more stable conditions above that layer (greater change in potential temperature per change in pressure) would tend to yield a larger  $Q_1$  magnitude for a given vertical velocity value. This explains the change in  $Q_1$  magnitudes around the 600 hPa level, but what might cause this distinct difference in stability?

Closer examination of the profiles reveals that the temperature and dewpoint curves spread apart as you move downward from 600 hPa, and then gradually move back toward each other

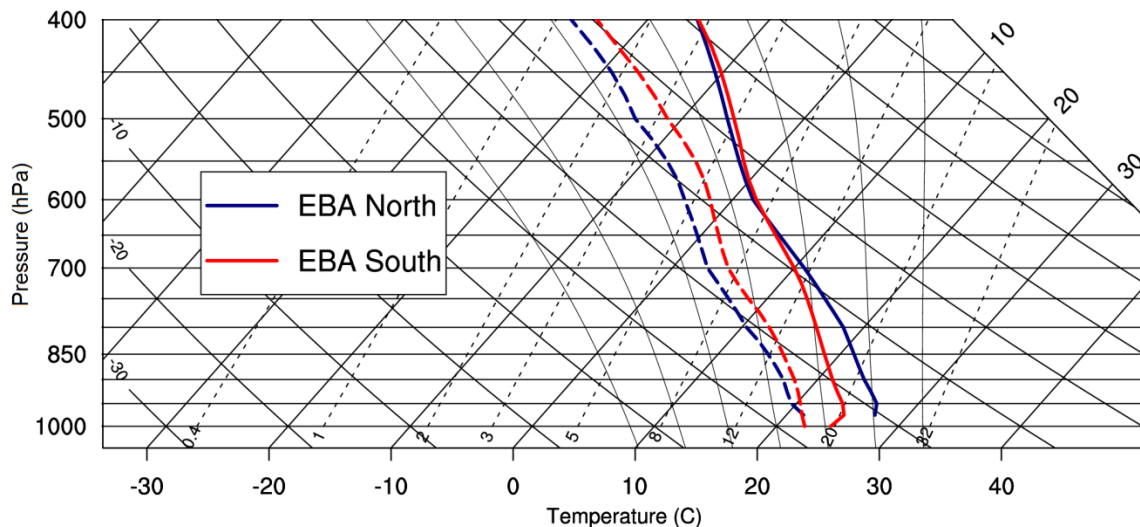


**Figure 4.7** Time-mean vertical profiles of temperature and dewpoint temperature, spatially averaged over the two EBA regions and temporally averaged from 1 July to 15 September 2006, plotted on a skew-temperature/log-pressure diagram. The solid curves represent temperature, while the dashed curves represent dewpoint temperature. The blue curves are averages over the EBA North zone and the red curves are averages over the EBA South zone.

other at lower levels. This sounding pattern, often referred to as an “onion shape” when the spreading and re-approach of the temperature and dewpoint lines is particularly dramatic, is a hallmark of a downdraft (Zipser 1977). The fact that this structure is present in a time mean vertical profile over two and a half months speaks to the great predominance in this area of mesoscale convective systems with extensive stratiform precipitation regions, which contain low to mid level downdrafts. This shape is more prominent in the mean sounding for the EBA South region, which matches with the relative commonality of low level sinking motion shown in Figure 4.6 in the southern zone and the numerous low level cooling episodes apparent in the EBA South panel of Figure 4.5. The pattern is still present in the northern region, and strong MCS downdrafts are likely there as well, considering that the drier ambient conditions would tend to promote low-level evaporation and cooling in precipitation systems even more than in the EBA South zone. However, the very deep, warm, and dry planetary boundary layers that regularly form in the northern area tend to make the profile less stable even in the absence of downdrafts, and mask some of the re-approach of the temperature and dewpoint curves at low levels that is more apparent in the EBA North structure. Additionally, the vigorous daytime rising motion connected with the deep boundary layers in the north appears to overwhelm the sinking motion related to downdrafts in the time mean, making low-level downward motion less common in the EBA North in Figure 4.6. It should also be pointed out that it is likely not a coincidence that the 575 to 600 hPa level where the thermal structure changes corresponds to where the temperature profiles cross the 0° C grid line. In addition to cooling from evaporation and sublimation, melting of frozen precipitation near the 0° C level contributes strongly to downdraft formation in thunderstorm systems, and the dividing line between heating and rising

motion aloft and cooling and sinking motion at low levels in the stratiform portion of the archetypal MCS tends to be near the freezing layer (e.g. Houze 1997).

Much reference has already been made to the typically hotter and drier conditions in the EBA North region compared to the southern zone, and this can be clearly seen in Figure 4.7, where time mean temperature values are several K warmer in the northern area at low levels, and dewpoint temperatures are a few degrees lower. Interestingly, the temperatures in the two EBA regions become quite similar in the mid levels, which is not surprising given the characteristically weak spatial temperature gradients in the tropical free troposphere, but the northern zone remains drier than the southern zone at both low and mid levels. These drier conditions could certainly influence MCS development in the northern area – entrainment of dry air can weaken convective updrafts, but the dry environment can also enhance evaporation and sublimation of hydrometeors and thus aid in downdraft formation. Some studies have suggested that when the dry air coexists with strong low-level wind shear, as in the Sahel region, long-lived, organized MCSs can be favored (Janicot et al. 2011). Whatever the precise role, it is clear from the thermal structure shown in Figure 4.7 and the low  $Q_1$  magnitudes and episodes of cooling at low to mid levels in Figure 4.5 that water phase changes and downdrafts in the stratiform regions of MCSs are major influences on the profiles of heating and vertical motion in the EBA areas.

Figure 4.8 shows time series plots of daily-mean TRMM 3B42 precipitation rate data, averaged over the EBA North and EBA South regions. Both panels of this figure show a very consistent three to five day period between major rainfall events, once again confirming the leading role played by easterly wave disturbances in modulating convective activity and precipitation episodes across the EBA zones. The influence of the timing of the seasonal shift in

# Daily-Mean EBA-Average TRMM 3B42 Precipitation Rate ( $\text{mm day}^{-1}$ )

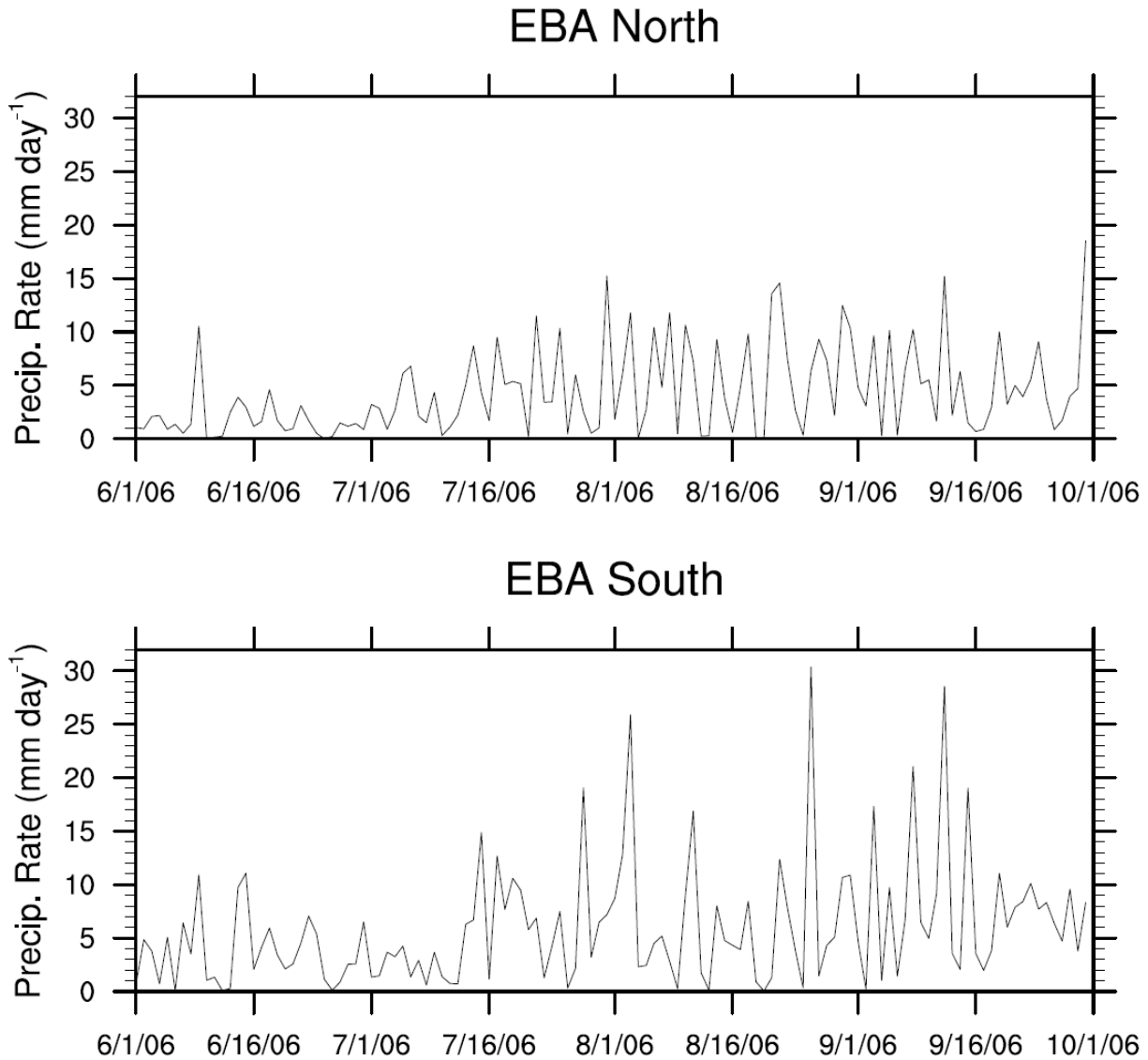


**Figure 4.8** Time series plots of daily mean TRMM 3B42 precipitation rate, in units of  $\text{mm day}^{-1}$ , spatially averaged over the EBA regions.

the West African monsoon regime is also evident in both graphs, as precipitation rates tended to be low during most of June, increased during the first part of July, were at their highest through the latter portion of the summer, and began to decline again by the second half of September.

This precipitation pattern helps to confirm the 1 July to 15 September period that was chosen

based on the relative vorticity plots for additional analysis as the peak of the summer monsoon phase and the most convectively active subset of the data availability time frame. Figure 4.8 also shows that precipitation rates were somewhat higher in the EBA South region than in the EBA North zone, which makes sense given the southern area's closer access to moist southwesterly flow off the Gulf of Guinea and generally more humid environment.

Time mean vertical profiles of divergence, vertical velocity, apparent heat source, and apparent moisture sink, averaged from 1 July to 15 September 2006, and averaged over the EBA North and EBA South regions, are shown in Figure 4.9. The profiles are generally rather complex, with lots of fine-scale structure, but this is not too surprising since they incorporate observations of many different types of conditions (day, night, clear, cloudy, shallow convection, deep convection, stratiform precipitation, and so on). Even so, many interesting patterns emerge. In both EBA regions, near-surface convergence is observed, which would be associated with rising motion at low levels. The depth of this convergence layer is much greater in the northern region (to about 800 hPa) than the southern region (to about 925 hPa), suggesting that it may be associated with the daytime planetary boundary layer, which tends to be quite deep in the dry northern areas and shallower in the south. Moving upward in both profiles, a divergence maximum is encountered next, but this feature is again located much higher (around 625 hPa) in the EBA North than in the EBA South (around 850 hPa). This pattern could be attributed to the top level to which typical shallow convection reaches in each region, either dry convective mixing, which can occur to a depth of several kilometers in the Sahel region on sunny summer afternoons, or cumulus convection and showery precipitation.

At mid levels, the EBA South profile is dominated by convergence, with maxima at around 675 hPa and 400 hPa. The EBA North profile follows a similar trend, but is shifted so

## EBA Mean Vertical Profiles (July 1 - Sept. 15)

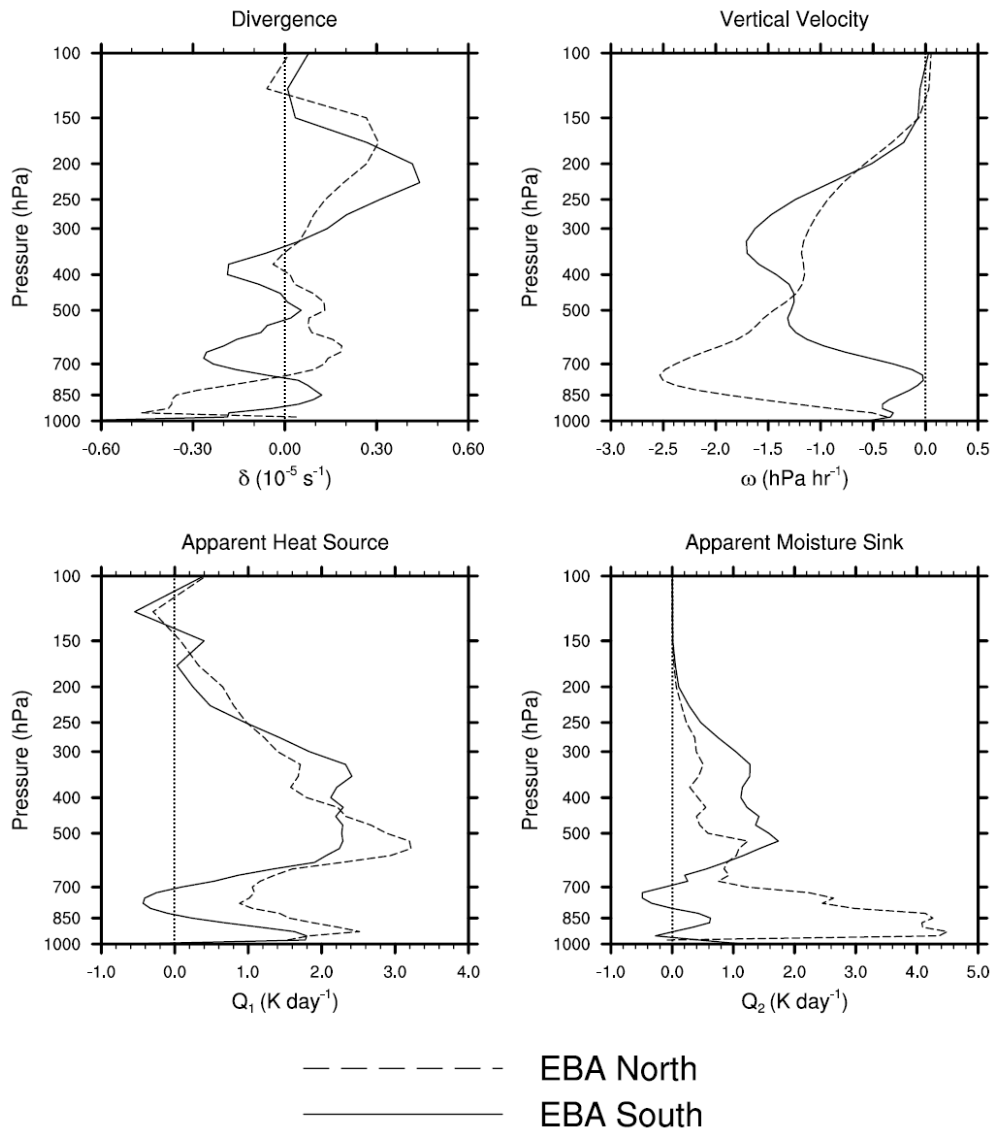


**Figure 4.9** Time-mean vertical profile plots, temporally averaged from 1 July to 15 September 2006 and spatially averaged over the two EBA regions, of divergence, in units of  $10^{-5} \text{ s}^{-1}$ , vertical velocity, in units of  $\text{hPa hr}^{-1}$ ,  $Q_1$  apparent heat source, in units of  $\text{K day}^{-1}$ , and  $Q_2$  apparent moisture sink, in units of  $\text{K day}^{-1}$ .

that divergence predominates, with minima near 525 hPa and 375 hPa. Both regions have a slight divergence maximum just above 500 hPa. In the upper troposphere, both areas' plots contain the largest maxima in divergence, with the southern profile peaking at 225 hPa and the

northern profile peaking at 175 hPa. The major divergence at upper levels is associated with deep convective activity, and the magnitude is bolstered by contributions from both “pure” deep convective updrafts and the stratiform regions of mesoscale convective systems, which both include rising motion at upper levels capped by divergence aloft. The fact that the divergence peak occurs at a higher level in the northern region than the southern region suggests that convective activity in the EBA North zone tends to reach a greater altitude, and thus may typically have more intense updrafts and higher anvils than that in the southern area. The mid-level convergence in both profiles is likely associated with extensive stratiform precipitation regions in MCSs, which feature rising motion aloft and sinking motion at low levels, and thus mid-level convergence into the system. In the classic MCS structure, this convergence tends to be maximized near the melting layer, which is typically near 600 hPa in this region, so the convergence maxima located between 500 and 700 hPa in the mean profiles could well be a reflection of this phenomenon.

The overall complexity of the divergence patterns suggest that both dry and moist convective activity in this area take place across a wide spectrum of heights, complicating the interpretation of any single mode. Rising motion features, such as growing boundary layers and convective updrafts, are associated with low-level convergence and divergence at the layer where they top out. However, other modes like stratiform precipitation systems include mid-level convergence with divergence both near the surface and aloft. Thus, for instance, widespread downdrafts in stratiform precipitation could mask out the divergence signal associated with growing boundary layers or vice versa. This could help to explain the shallow low-level divergence layer and dominant mid-level convergence in the EBA South region, where Figures 4.5 and 4.6 suggested cooling and sinking motion prevailed in the mean. On the other

hand, the greater intensity and vertical extent of dry boundary layers in the northern zone, associated with deeper and more prevalent mid-level divergence, could obscure indications of the convective downdrafts that also occur in that area. Despite the intricacy of the profiles, the EBA North region tends to have strong low-level convergence and areas of divergence at mid and upper levels, suggesting a predominance of shallow convective (both dry and moist) and deep convective modes. The EBA South area has more mid-level convergence, with divergence at low levels and aloft, indicating that a stratiform precipitation structure is the leading contributor to the mean pattern there.

The vertical velocity plot paints a similar picture to the divergence profiles, which is not surprising considering that the vertical motion field is mainly an integration of the divergence. The northern region is characterized by rising motion at all levels in the time mean, with a strong upward peak at 750 to 800 hPa, a relative minimum near 400 hPa, and additional rising motion at upper levels. The EBA South zone curve indicates shallow rising motion at low levels, near-zero vertical velocity around 750 hPa, one peak in upward motion near 550 hPa, and a larger peak in rising motion at 350 hPa. The low-level maximum in ascent in the northern region reiterates the prevalence of shallow convective activity in that area, with deep boundary layers growing during the daytime and showery precipitation taking place when adequate moisture is present. The upper-level rising motion peak can be explained by the combined effects of both deep convective updrafts and stratiform regions of MCSs. In the EBA South, the shallow layer of upward vertical velocities looks to be a reflection of the daytime boundary layer, but the mid-level minimum of vertical motion is another strong indication of the frequency of convective downdrafts in that area. Only the superposition of the structures of both shallow and deep updrafts on this pattern precludes downward velocities in this layer in the time mean. Similar to the northern zone, the

rising motion peak near 550 hPa in the south is suggestive of shallow moist convection, while the higher maximum at 350 hPa indicates the influence of deep convection and upward velocities in stratiform regions together. The fact that the upper-level peak in rising motion is stronger in the southern region than the northern zone may be attributable to a greater contribution from stratiform precipitation areas in the south. Of course, it could also indicate that convective systems in the northern region simply have a broader spectrum of heights while those in the south tend to concentrate their peak rising motion over a narrow range of levels.

The profiles of the  $Q_1$  apparent heat source show similar patterns between the EBA North and South areas, though some distinctions exist. Both regions have a low-level peak in positive  $Q_1$ , though the maximum  $Q_1$  value is greater and the peak is at a slightly higher altitude in the north. Then, both profiles show a strong minimum in  $Q_1$  at 750 to 800 hPa, with the apparent heat source value remaining positive in the north but becoming negative, indicating cooling, in the south. There is a large upper-level peak in  $Q_1$  in each of the two curves, though the maximum value is of greater magnitude but occurs at a lower height in the north, while the heating maximum is lower in amplitude but broader and at a higher layer in the south. The near-surface peaks look to be connected with the boundary layer and related shallow convection, with the greater magnitude and higher layer in the north both consistent with the deep, dry mixed layers that form there. The minima around 750 to 800 hPa represent a clear signal of cooling connected with widespread downdrafts in stratiform precipitation regions in both EBA zones. In the south, this pattern overwhelms the effects of shallow and deep convection to yield net cooling in the time mean, while the deeper boundary layers in the north combine with other shallow and deep convection to maintain a net positive  $Q_1$  value. The upper-level heating maxima in the two regions embody the influence together of deep convective updrafts and

stratiform regions in MCSs, both of which produce heating aloft. The thicker heating peak in the northern region is similar to that produced in the archetypal deep MCS, where vertically extensive layers of rising motion, condensation, and deposition in both the main convective line and the stratiform section produce a broad and relatively homogeneous zone of heating. In the EBA South,  $Q_1$  is greater than in the north between about 600 and 425 hPa, lower between 425 and 250 hPa, and greater again between 250 and 175 hPa. This implies, similar to the vertical motion arrangement discussed above, that there may be a wider spectrum of cloud heights in convective activity in the northern region, with some moderately deep updrafts with peak heating at mid levels, and other very deep storms that still produce appreciable heating around the 200 hPa level. Of course, the structure of the stratiform regions of MCSs could play a role as well, if, for instance, they contribute strong heating just above the freezing layer. As will be discussed in association with Figure 4.10, such a heating pattern has occasionally been detected in datasets from other field programs.

The profiles of the  $Q_2$  apparent moisture sink indicate notable differences between the EBA North and EBA South regions. In the southern zone, there is a small maximum around 850 hPa, a minimum near 750 hPa, and a broad maximum between 700 and 200 hPa. On the other hand, the northern area curve shows a strong maximum between about 950 and 700 hPa and a section of lower-magnitude, but still positive,  $Q_2$  from 700 to 200 hPa. The most striking feature is the intense low-level drying signal in the EBA North, showing the great influence of shallow convection, both dry and moist, on the water vapor budget in that area. Both condensation and vertical eddy water vapor flux divergence associated with deep mixing likely contribute to this substantial  $Q_2$  pattern. The broader zone of weaker positive apparent moisture sink aloft in the northern region is associated with condensation and eddy fluxes in the more standard moderate

to deep convective and stratiform modes. The low-level  $Q_2$  peak in the EBA South looks to be connected with boundary layer mixing and other shallow convection, while the  $Q_2$  minimum, characteristic of net moistening, is coupled with the prevalent stratiform region downdrafts and their associated evaporation. Again, the fact that this evaporation and moistening feature appears in the time mean over a two and a half month period speaks to the prime role played by stratiform rainfall across this area. Like in the EBA North, the broad region of positive  $Q_2$  aloft in the southern zone's curve is suggestive of vertically extensive net condensation at upper levels in deep convection and stratiform precipitation shields.

As a comparison for the  $Q_1$  and  $Q_2$  structures computed from AMMA data shown in Figure 4.9, Figure 4.10 illustrates heating and moistening profiles based on observations during numerous other tropical field campaigns that have been studied in the literature. Many of these experiments took place in the western Pacific Ocean (curves labeled as Yanai et al. (1973), OSA, IFA, and KWAJEX), while SCSMEX was located in the South China Sea, LBA occurred in the southwestern Brazilian Amazon, and the Thompson et al. (1979) data are from the GATE project in the eastern tropical Atlantic. It should be noted that the  $Q_1$  and  $Q_2$  profiles in the top two panels of Figure 4.10 were normalized by rainfall rate. Thus, the magnitude values will not be directly comparable to those in the bottom panel of Figure 4.10 or those in Figure 4.9, and structures associated with little to no precipitation (e.g. dry convection in daytime boundary layers) will not be detectable in the upper panels.

The apparent heat source structure in the EBA South region appears generally similar to that of the western Pacific field campaigns, with a relatively broad, homogeneous upper-level  $Q_1$  peak between 300 and 600 hPa, though the EBA South maximum looks to be even broader than any of those shown in Figure 4.10. The magnitude of the upper-level  $Q_1$  peak is comparable to

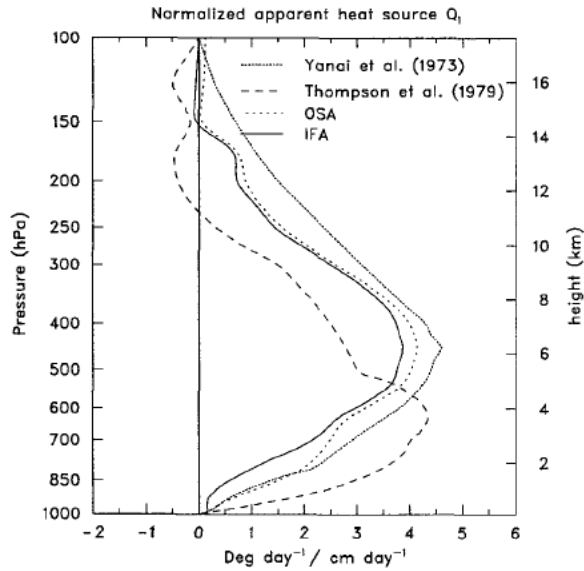


FIG. 11. Comparison of rainfall-normalized apparent heat source  $Q_1$  (in units of  $K \text{ day}^{-1}/1 \text{ cm day}^{-1}$ ) from the IFA, the OSA, the Marshall Islands region (Yanai et al. 1973), and the GATE region (Thompson et al. 1979).

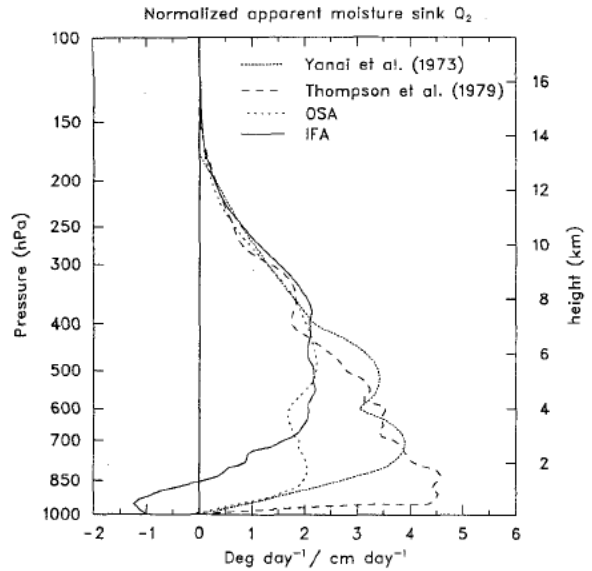


FIG. 12. Comparison of rainfall-normalized apparent heat source  $Q_2$  (in units of  $K \text{ day}^{-1}/1 \text{ cm day}^{-1}$ ) from the IFA, the OSA, the Marshall Islands region (Yanai et al. 1973), and the GATE region (Thompson et al. 1979).

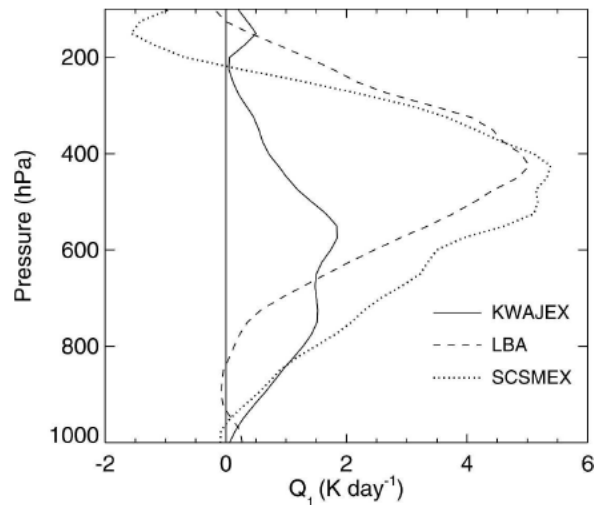


FIG. 4. Field campaign average  $Q_1$  profiles.

**Figure 4.10** Time-mean vertical profile plots of the  $Q_1$  apparent heat source and  $Q_2$  apparent moisture sink derived from observations during several tropical field campaigns other than AMMA. The upper left panel shows  $Q_1$  from several projects, normalized by rainfall rate, while the upper right panel shows  $Q_2$  from those same studies, also normalized by rainfall rate. The bottom panel shows raw (non-normalized)  $Q_1$  from a different set of field projects. The upper panels are from Lin and Johnson (1996), Figures 11 and 12, and the lower panel is from Schumacher et al. (2007), Figure 4.

that of the KWAJEX data, although the peak heating in that study was at a lower layer.

Additionally, none of the other projects show the substantial cooling feature near 750 hPa that is

present in the EBA South profile, though some very slight low-level cooling is indicated by the LBA curve, which was the only other field campaign that took place mainly over land. This continues to underscore the unique prominence of downdrafts and low-level cooling in the West Africa region compared to other tropical locations. Moreover, the near-surface heating maximum evident in Figure 4.9 does not appear in any of the Figure 4.10  $Q_1$  curves, highlighting the unique properties of the boundary layer and shallow convection over continents that have been revealed by AMMA.

The EBA North apparent heat source pattern, on the other hand, appears distinctly similar to the Thompson et al. (1979) profile from GATE. Perhaps this should not be too surprising, since GATE was geographically the closest of the other field projects to AMMA, taking place in the eastern Atlantic Ocean, but given the differing ocean vs. land environments of the studies, the resemblance is rather striking. Both the EBA North and GATE profiles had their maximum  $Q_1$  peak at around 600 hPa, with lower  $Q_1$  values at upper levels than the EBA South or other field project curves. The GATE structure did not include the downdraft-related  $Q_1$  minimum near 800 hPa that was present in the EBA North plot, so stratiform precipitation does appear to have played a larger part in shaping the AMMA heating profile. Similar to the EBA South comparison, the GATE data do not show the low-level heating maximum present in the EBA North region, but since this is likely due to mostly dry convection and the GATE data were normalized by rainfall rate, it is not surprising that this feature is absent in Figure 4.10.

Looking to the apparent moisture sink profiles presented in the upper right panel of Figure 4.10, an obvious parallel can also be drawn between the EBA North  $Q_2$  structure and that of the Thompson et al. (1979) observations from GATE. While the EBA North pattern appears to have an even stronger low-level drying peak than the GATE data, the overall shape of the

curves is remarkably similar, with a strong near-surface  $Q_2$  maximum and a gradual decrease at higher altitudes, but with positive apparent moisture sink all the way up to around 200 hPa. The EBA South structure, on the other hand, is more comparable to the IFA curve from TOGA-COARE in the western Pacific, with some low-level moistening overlaid by a healthy degree of vertically homogeneous drying between 700 and 200 hPa. Lin and Johnson (1996) attribute the low-level moistening in the IFA region to strong evaporation and upward moisture transport by shallow cumuli during high winds. While this type of process may play some role in the EBA South region as well, the coincident presence of notable cooling and downward vertical motion in the AMMA data suggest downdrafts are the main factor in West Africa.

Another connection between the AMMA mean vertical profiles and the GATE observations from Thompson et al. (1979) exists in relation to the divergence pattern. The GATE divergence structure, like that in the EBA regions, was quite complex, with numerous alternating layers of maxima and minima through the vertical column. Comparison of the GATE divergence data in Figure 5 from Thompson et al. (1979) with the upper left panel of Figure 4.9 shows remarkable similarity, with the lower part of the atmosphere especially resembling the EBA North curve and the upper levels looking more like the EBA South curve. It does make sense that these observations, taken in the same general part of the tropics, would look alike, but the relationship is quite good considering the differing marine vs. continental contexts of the two projects. On the whole, the intricate patterns in the GATE and AMMA measurements suggest a unique diversity in the cloud populations in this part of the world that complicates the application of general tropical meteorology principles to conditions in the area.

### c. Mean Meridional Cross Sections

Figure 4.11 shows a time mean north-south vertical cross section of zonal wind based on the AMMA radiosonde gridded dataset, averaged over the time period from 1 July to 15 September 2006, and averaged over the longitude band from  $0^{\circ}$  to  $7^{\circ}$  E, which corresponds to the EBA regions. The plot shows that at low levels, below about 850 hPa, flow with a westerly component predominates at this time of year. This flow pattern illustrates the moist, southwesterly monsoon winds that blow off the Gulf of Guinea and across the southern part of West Africa during the boreal summer season, transporting water vapor well inland and supporting the northward shift in the latitude of maximum precipitation. Within this layer of westerly winds, one maximum is evident around  $6^{\circ}$  N latitude, near the coast, while another peak in the magnitude of the monsoon flow is centered in the Sahel region, around  $14^{\circ}$  N to  $15^{\circ}$  N latitude. The lower right corner of the plot also shows some evidence of near-surface easterlies, which may be a reflection of the dry, northeasterly winds that blow off the Sahara Desert and meet the monsoon flow at the inter-tropical discontinuity (Janicot et al. 2011). Above the 850 hPa level, winds are easterly in the time mean. Some important mid-level features evident in Figure 4.11 include the African easterly jet, centered around 600 hPa at  $13^{\circ}$  N to  $16^{\circ}$  N latitude, along which easterly wave features propagate. The importance of these African easterly waves for modulating convective activity in the EBA regions has been greatly emphasized in both Chapter 2 and earlier in this chapter. Additionally, a relative minimum in the easterly flow at mid-levels is apparent near the coast, around  $6^{\circ}$  N latitude. In the upper levels, the dominant structure is that of the strong tropical easterly jet, which extends from around the 200 hPa layer at latitudes between  $5^{\circ}$  N and  $10^{\circ}$  N upward and northward to the 100 hPa level at  $13^{\circ}$  N to  $15^{\circ}$  N latitude.

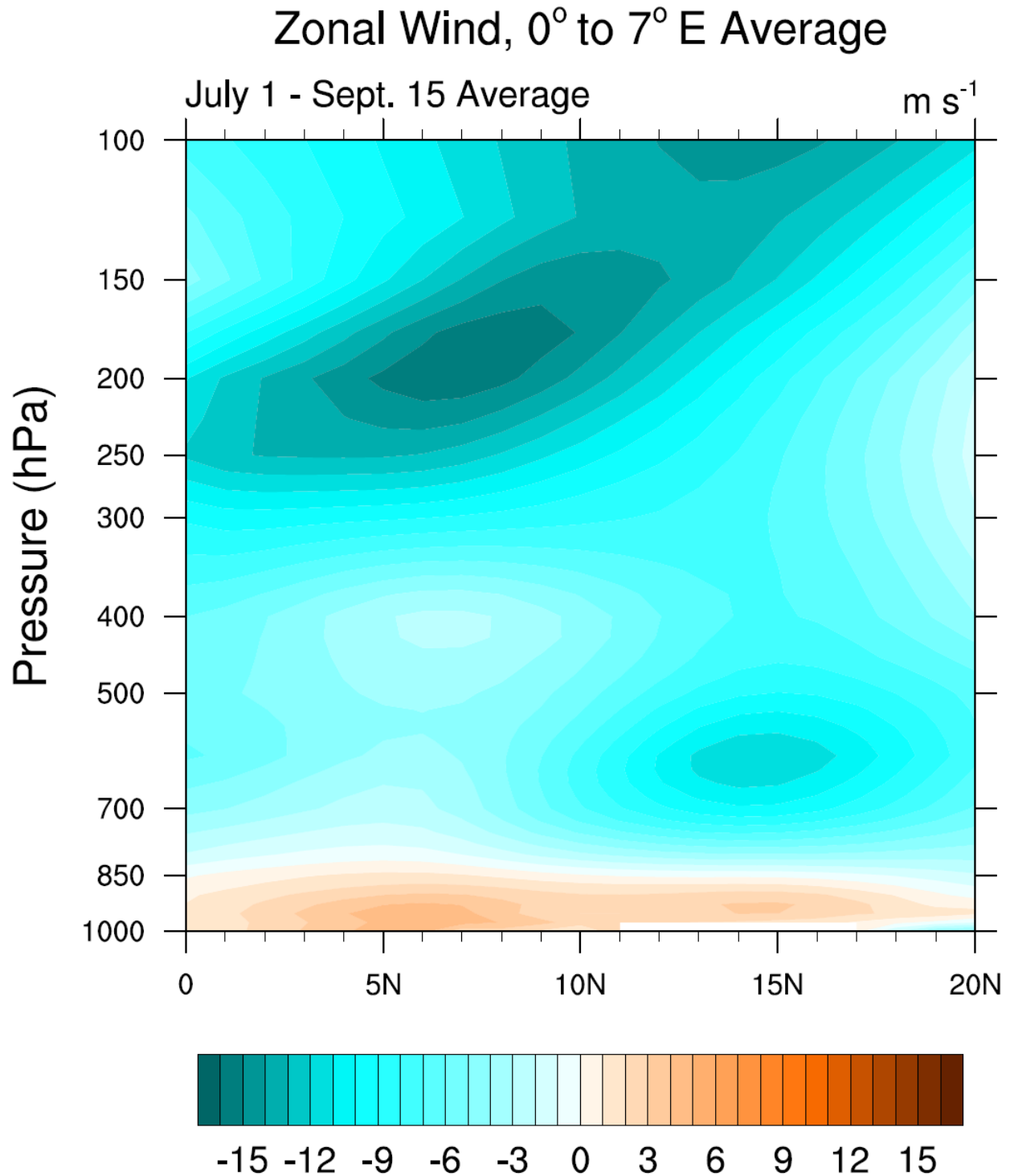


**Figure 4.11** Time-mean latitude vs. pressure cross-section contour plot of zonal wind, in units of  $\text{m s}^{-1}$ , from the AMMA radiosonde gridded analysis, temporally averaged from 1 July to 15 September 2006 and spatially averaged over the 0° to 7° E longitude band.

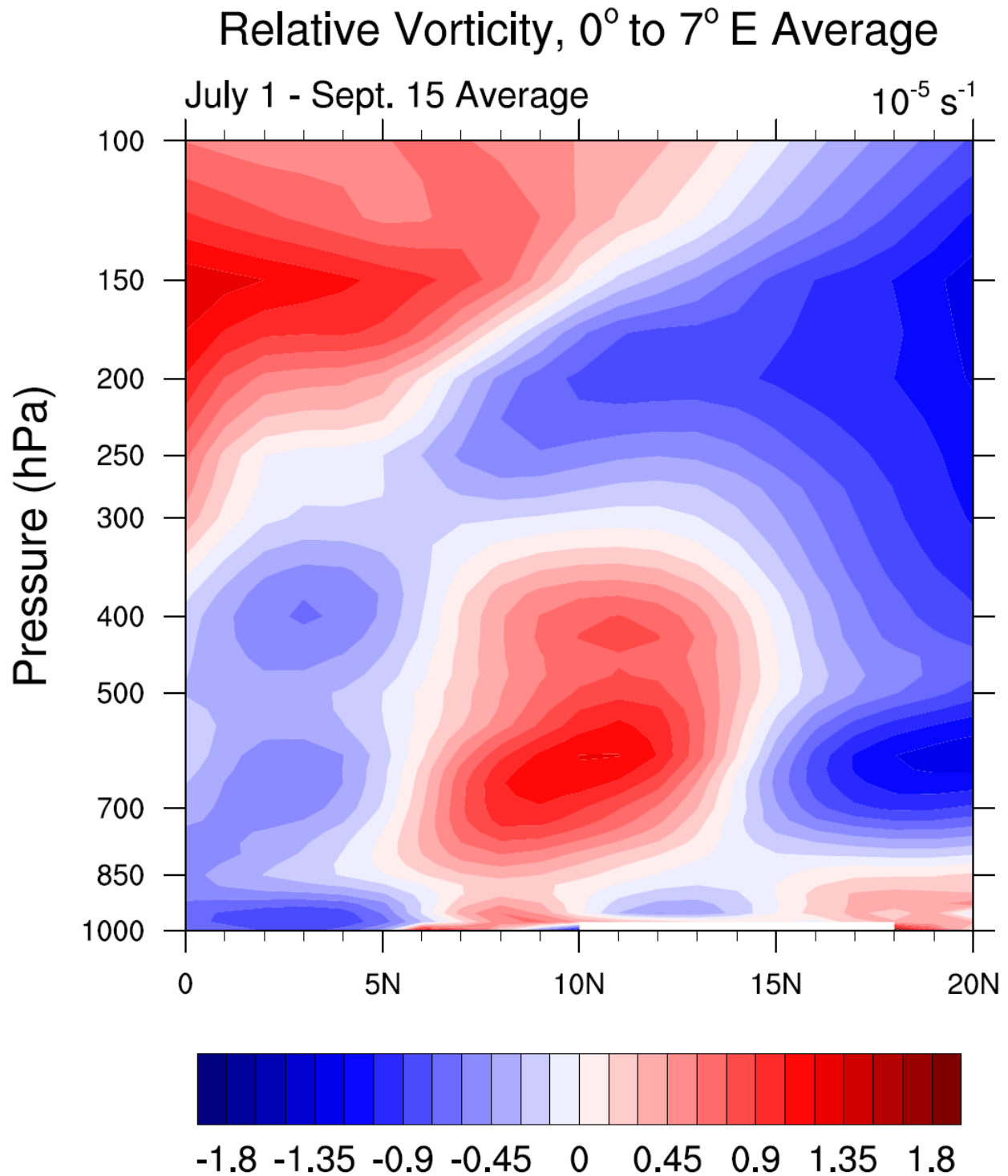


**Figure 4.12** Time-mean latitude vs. pressure cross-section contour plot of relative vorticity, in units of  $10^{-5} \text{ s}^{-1}$ , derived from the AMMA radiosonde gridded analysis, temporally averaged from 1 July to 15 September 2006 and spatially averaged over the 0° to 7° E longitude band.

In a similar vein, Figure 4.12 depicts a time mean north-south vertical cross section of relative vorticity based on the AMMA radiosonde gridded dataset, averaged over the time period from 1 July to 15 September 2006, and averaged over the longitude band from 0° to 7° E. The typical vorticity pattern shown in this plot matches up very nicely with the wind distribution from Figure 4.11. At low levels, each of the westerly wind maxima are straddled by a pair of vorticity centers, with negative relative vorticity to the south (off the coast and between 10° N and 15° N latitude), and positive relative vorticity to the north (between the coast and 10° N latitude and north of 15° N latitude). These patterns correspond with the relative prevalence of positive low-level relative vorticity in the EBA South region in Figure 4.3 and of negative low-level relative vorticity in the EBA North zone. Similarly, at mid levels, the African easterly jet is straddled by a deep zone of positive mean relative vorticity to its south and negative relative vorticity to its north. As discussed earlier in this chapter, this places the EBA North area in a position where meridional deflections of the jet can place it within a regime of either negative or positive mid-level relative vorticity, whereas the southern region tends to be more consistently characterized by positive mid-level relative vorticity in a mean sense.

It should be noted as well that a pattern of positive relative vorticity at mid levels near and south of the African easterly jet, along with a low-level maximum in positive relative vorticity north of the jet latitude, is a known signature of easterly wave activity. As discussed in Chapter 2, Pytharoulis and Thorncroft (1999) found that African easterly wave disturbances include two distinct centers of positive vorticity that move together as a single system – one at mid levels near and south of the jet, and the other at low levels north of the jet. That this vorticity configuration is evident in the time mean provides further evidence for the strong influence of easterly waves on the weather in this region. Also at mid levels, the relative

minimum in easterly flow located at the latitude of the coast is associated with a change in the sign of relative vorticity, with the zone of positive vorticity to the north, over land, and a weaker region of negative relative vorticity offshore to the south. Lastly, in the upper troposphere, the relative vorticity structure is dominated by the tropical easterly jet, with positive relative vorticity to its south and negative relative vorticity to its north. The north-south tilt of this jet structure with height usually places both EBA regions in a negative relative vorticity regime around the 200 hPa layer, but moving up toward the 100 hPa level, the southern zone, as well as the northern zone at times, is often characterized by positive relative vorticity, as discussed in association with Figure 4.3.

## CHAPTER 5

### DIURNAL CYCLE

#### a. AMMA Gridded Dataset Meridional Cross Sections

Figures 5.1 through 5.5 depict north-south vertical cross sections of variables from the AMMA radiosonde gridded dataset, averaged at different points in the diurnal cycle. Each figure contains four panels, representing the conditions at 0000 UTC, 0600 UTC, 1200 UTC, and 1800 UTC. For each time of day, the data were averaged over the period from 1 July to 15 September 2006, as well as over the longitude band from 0° to 7° E. While the local civil time zones vary somewhat from the theoretical ideal in this region, it should be noted that since the entire 0° to 7° E longitude band is quite close to the Prime Meridian, UTC is essentially equivalent to the local solar time in this area.

Figure 5.1 shows the values of the  $Q_1$  apparent heat source. Over the ocean (roughly south of 5° N to 6° N latitude), the profile at midnight is dominated by negative  $Q_1$ , which is likely associated with radiative cooling. By 0600 UTC, a shallow to moderately deep convective heating profile arises, suggestive of showers and thunderstorms developing offshore at this time. A similar structure persists at noon, though heating magnitudes continue to be relatively low, and a minimum in the heating forms around 800 hPa, indicating that downdrafts could be contributing to low-level cooling by then. At 1800 UTC, apparent heat source magnitudes are near zero as conditions transition back toward the 0000 UTC structure. This pattern generally matches well with the previous studies of the diurnal cycle of precipitation discussed in Chapter 2. Laing et al. (2008) found cold cloud coverage offshore of this part of West Africa increasing at 0500-0600 UTC, maximizing at 1100-1200 UTC, decaying at 1700-1800 UTC, and minimal

## Apparent Heat Source ( $\text{K day}^{-1}$ ), $0^\circ$ to $7^\circ$ E Average

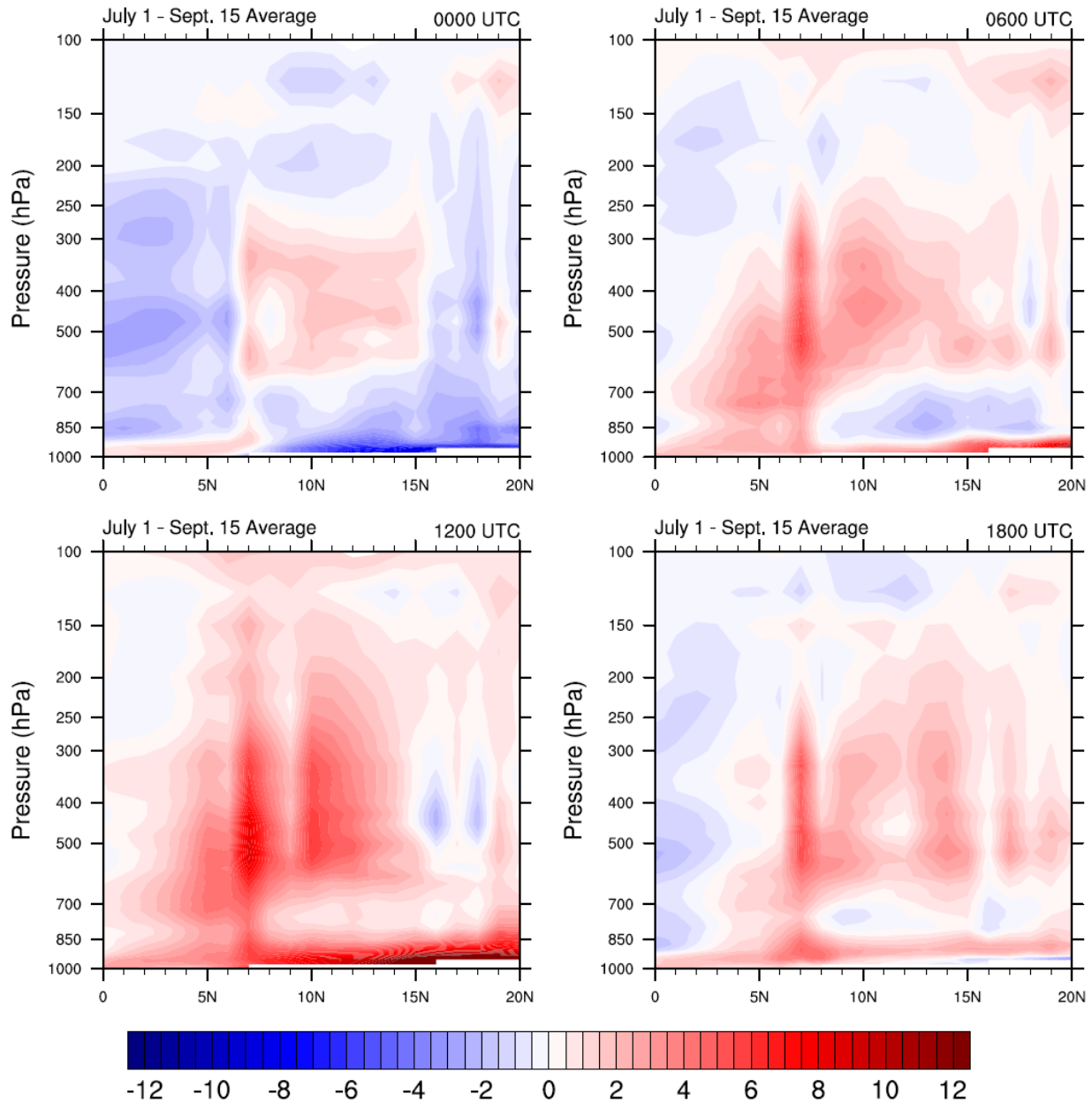


**Figure 5.1** Time-mean latitude vs. pressure cross-section contour plots of the  $Q_1$  apparent heat source, in units of  $\text{K day}^{-1}$ , derived from the AMMA radiosonde gridded analysis, averaged at different points in the diurnal cycle. The upper left panel shows the data from 0000 UTC, the upper right panel shows the data from 0600 UTC, the lower left panel shows the data from 1200 UTC, and the lower right panel shows the data from 1800 UTC. At each time of day, the values were temporally averaged from 1 July to 15 September 2006 and spatially averaged over the  $0^\circ$  to  $7^\circ$  E longitude band.

at 2300-0000 UTC. This suggests morning development of precipitation systems, with a peak in late morning or early afternoon. Similarly, Johnson (2011) showed the time of mean maximum TRMM 3B42 rainfall in this area varying from mid-morning to mid-afternoon. However, the comparatively shallow heating structures shown in Figure 5.1 suggest that precipitation estimates relying on infrared satellite data and cold cloud features may not be optimal for estimating rainfall in this area. The heating that is already occurring at 0600 UTC in Figure 5.1 indicates that convective activity may be developing earlier in the morning than previous analyses have indicated and that storms could be maturing or even decaying by the noon hour. A final caveat to the examination of the offshore  $Q_1$  profile is that all of the sounding sites used in creating the AMMA gridded analysis were on land. Therefore, these patterns may be influenced more by the ECMWF reanalysis data than other parts of the cross section, and accordingly should be interpreted with some caution.

The low-level apparent heat source cycle over land shows interesting features as well. At midnight, negative  $Q_1$  predominates, with the lowest values in the northern part of the domain. By 0600 UTC, positive  $Q_1$  develops, while by noon, the layer of positive apparent heat source becomes deeper and the magnitudes increase dramatically, especially toward the north. At 1800 UTC, a layer of generally positive  $Q_1$  persists at low levels, but amounts are much lower than at noon, and a thin strip of negative apparent heat source exists just above the surface in the northern half of the area. While water phase changes and radiative effects certainly play some role in shaping these features, they are likely primarily associated with vertical eddy sensible heat flux convergence and divergence in the boundary layer. At night, the negative  $Q_1$  would be associated with heat flux divergence and cooling as conditions stabilize. Contributions to negative apparent heat source overnight could also come from radiative cooling and evaporation

in downdrafts. During the daytime, though, as deep mixing and solar heating grow the boundary layer, heat flux convergence would occur, resulting in positive  $Q_1$ . The strong negative values at midnight and positive values at noon are not surprising, then, although the very high magnitudes and appreciable depth of the heating layer at 1200 UTC are noteworthy. Moreover, the increase in the amplitude of the diurnal cycle toward the north is as expected, since that region is typically hotter, drier, and has clearer skies, allowing deep mixing to take place during the day and increasing the magnitudes, in particular, of radiative and sensible heat fluxes at the surface and at low levels. It is interesting that appreciable heating is already taking place by 0600 UTC, indicating that boundary layer mixing and a daytime flux regime start quickly in the morning during the summer in West Africa. On the other hand, less heating and even some cooling occur at 1800 UTC, which may represent the combined effects of a quick evening transition toward the overnight scheme and some convective downdrafts, though well-organized MCSs tend to occur later in the night in this region.

Analysis of the evolution of the  $Q_1$  structure aloft over land is also revealing, particularly in terms of the diurnal cycle of precipitation systems. At 0000 UTC, a strong stratiform precipitation signal is present from  $7^\circ$  N to  $15^\circ$  N latitude, with weak to moderate heating above 600 hPa and cooling at low levels. Similar to the situation over the ocean, negative  $Q_1$  generally predominates at all levels north of  $15^\circ$  N, suggesting a lack of precipitation and radiative cooling taking place in those semi-arid and desert areas. By 0600 UTC, a more convective profile of deep heating develops near the coast, while the stratiform pattern of heating over cooling persists farther inland, and even intensifies and expands farther to the north. At noon, strong deep convective heating is taking place near the coast, with a peak around  $7^\circ$  N, and a deep convective pattern also forms farther inland, with a secondary peak in mid- to upper-level heating between

10° N and 13° N, which corresponds with the latitude of the high terrain of the Jos Plateau. A relative minimum in the  $Q_1$  magnitude exists inland between 700 and 850 hPa, suggesting some downdrafts are present, and a zone of negative apparent heat source at mid levels between 15° N and 19° N implies the presence of large-scale subsidence, perhaps in response to the extensive convective updrafts occurring farther south. By 1800 UTC, a deep convective profile remains near the coast, albeit less intense than at noon, while a transition to a more stratiform structure appears inland, with generally weaker heating now overlaying minor cooling.

These patterns generally correspond with the diurnal cycle of rainfall in West Africa as determined by previous studies. As described by Laing et al. (2008), convection often initiates in the lee of high terrain by early afternoon and thunderstorm systems grow and merge through the afternoon and evening. By late evening, that study found fewer intense convective systems, but for those that persist, the cold cloud areas expand and shift westward with time, and by early morning, convective intensity continues to reduce while the complexes propagate further to the west. The  $Q_1$  profiles in Figure 5.1 indeed show evidence of deep convective formation at the latitude of the Jos Plateau at 1200 UTC, while the magnitude of the upper level heating maximum decreases and a more stratiform pattern with low-level cooling emerges by 1800 UTC. This suggests the development of mature MCSs, and the stratiform  $Q_1$  configuration becomes even more prominent by 0000 UTC, with this structure persisting and even expanding in latitudinal coverage by 0600 UTC. While the time resolution of this data is not optimal for determining exactly when convective activity first forms, the deep heating present by 1200 UTC insinuates that thunderstorms may develop earlier in the day than has been indicated by prior studies using cold cloud tops as a proxy for convective intensity. (This issue of a timing mismatch between heating profiles and cold cloud tops as indicators of deep convection will be

explored further later in this chapter.) Regardless, it appears that after noontime or early afternoon initiation, thunderstorms organize into MCSs by evening, then propagate westward across the study domain during the night, and reach a wide area at the western edge of the EBA regions by early morning. Once these convective systems evolve into the mature stage, the stratiform heating structure seems to dominate their influence on the large-scale thermodynamic environment.

Another interesting aspect of the apparent heat source data in Figure 5.1 is the persistent, deep heating maximum located near  $7^{\circ}$  N latitude. Across much of the longitudinal averaging domain for these plots, the Gulf of Guinea shoreline is located near  $6^{\circ}$  N latitude, so this location is generally just inland from the coast. In addition, there are a few different areas of moderately high terrain (500 – 1000 m elevation) located at around  $7^{\circ}$  N, notably in south central Togo and southwest Nigeria. Accordingly, there may well be a combination of the moist monsoon flow and sea breezes, both impinging on hilly to mountainous topography, that could help explain the apparent convective maximum in this area. The apparent heat source maximum is of greatest magnitude at 1200 UTC, which makes sense from the perspective of convection initiating in association with high terrain or along a sea breeze. However, it is also fairly prominent at 0600 and 1800 UTC and even present to a degree at 0000 UTC, so rainfall and thunderstorms of some form look to be a frequent occurrence at that latitude throughout the diurnal cycle.

Figure 5.2 provides plots of the  $Q_2$  apparent moisture sink data. Of note overall is that  $Q_2$  magnitudes are generally largest at low to mid levels and become small to near zero at upper levels, which is simply due to the fact that water vapor concentrations are largest near the surface and rapidly decrease aloft. At 0000 UTC, a broad region of drying is present aloft north of  $7^{\circ}$  N, which generally corresponds to the zone of heating in Figure 5.1, suggesting that net

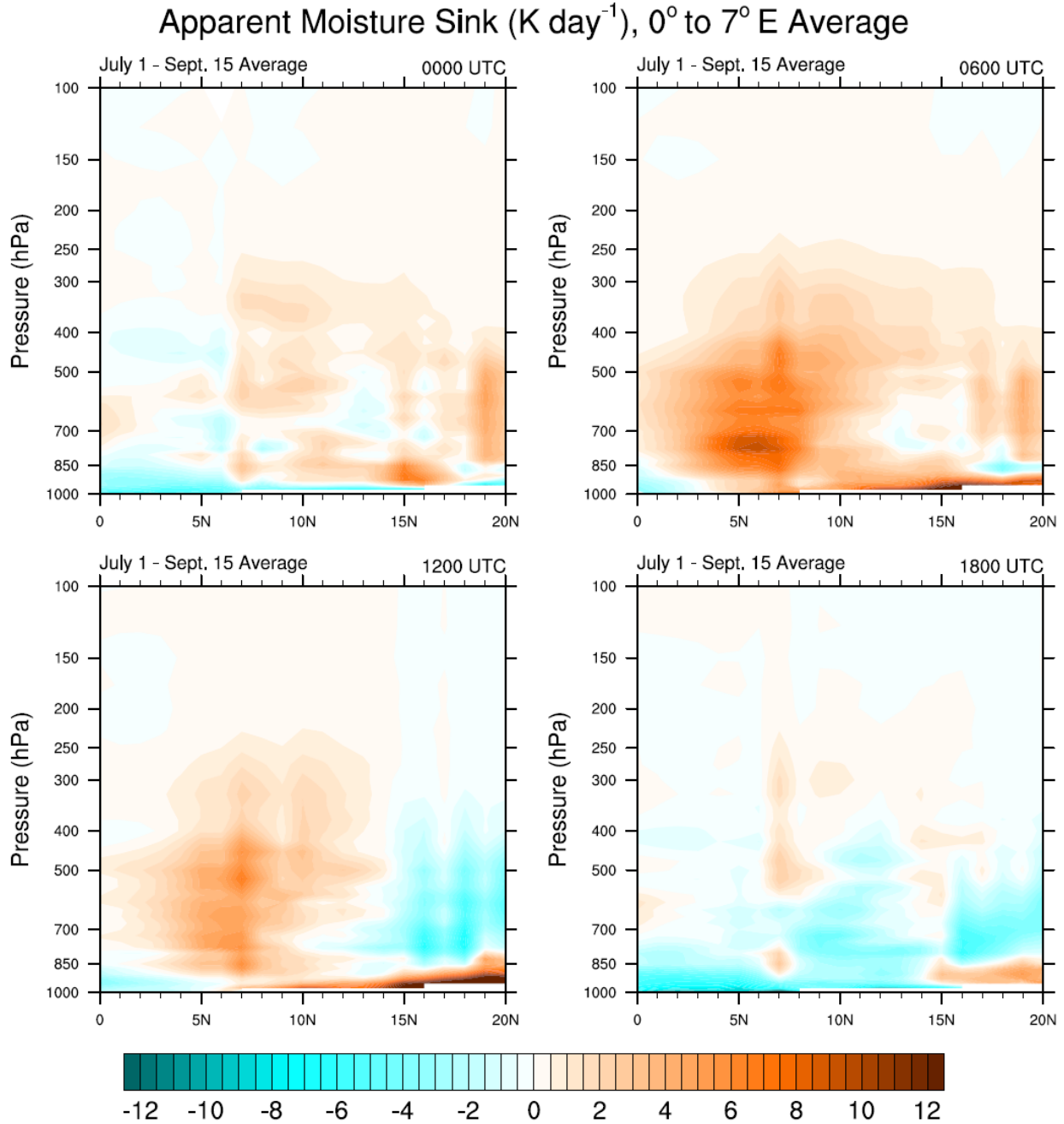


**Figure 5.2** As in Figure 5.1, but for the  $Q_2$  apparent moisture sink, in units of  $\text{K day}^{-1}$ .

condensation and deposition are taking place in the upper levels of the extensive MCSs present overnight in the region. While there is some negative  $Q_2$  present at mid levels below this feature, which would be indicative of net evaporation, there is also an extensive band of low-level drying over a thin, near-surface strip of moistening. This pattern would imply vertical eddy moisture

flux divergence at low levels with water vapor flux convergence at the surface, so perhaps the widespread downdrafts are playing some role in transporting moisture from the lower part of the troposphere to the surface.

By 0600 UTC, widespread drying exists at low to mid levels throughout most of the domain, with a maximum in positive  $Q_2$  near the surface in the northern part of the analysis region. This low-level drying peak looks to be associated with the start of daytime boundary layer mixing, as was also indicated in Figure 5.1, and a moisture flux divergence out of the boundary layer. On a related note, Lothon et al. (2008) found that the moist, southwesterly nocturnal low-level jet that occurs regularly in this region during the summer monsoon phase maximizes around 0500 UTC at 400 m above ground level. They emphasized the role of this jet in bringing in water vapor from the south overnight as well as the role of the daytime boundary layer in mixing the moisture over a greater depth of the lower troposphere. Thus, the near-surface moisture flux divergence suggested by Figure 5.2 may well be attributable to the start of vertical mixing of water vapor transported inland during the night by a low-level jet. The broader region of positive  $Q_2$ , particularly that near the coast and offshore from 850 to 400 hPa, may well be associated with net condensation and deposition in showers and thunderstorms, as rainfall picks up during the morning in that area. However, the fact that the largest amplitudes of positive  $Q_2$  outside of the boundary layer occur at 0600 UTC may have more to do with the daytime dry bias in the radiosonde observations. As addressed in Chapter 3, while some efforts were undertaken to correct this problem, it likely still exists to some extent in the AMMA gridded dataset. Thus, the extensive “drying” at 0600 UTC could be more indicative of a transition to the daytime underestimation of humidity by the sounding measurements than of any physical process.

At noon, the apparent moisture sink distribution aligns quite well with the apparent heat source pattern shown in Figure 5.1. A large zone of drying exists between 900 and 250 hPa south of about 13° N latitude, suggesting net condensation and deposition taking place in thunderstorm activity in the same areas highlighted by heating in the  $Q_1$  plot. Again, the peak magnitude of apparent moisture sink falls at 7° N latitude, suggesting intense convection and precipitation taking place in that area. Over land, the boundary layer is dominated by intense drying, illustrating the deep mixing that is occurring and the moisture flux divergence out of the low levels, with the greatest thickness and amplitude in the northern reaches of the domain. The moistening centered around 750 hPa between 10° N and 15° N may be indicative of net evaporation in convective downdrafts, the presence of which were also implied by a collocated minimum in apparent heat source shown in Figure 5.1. Lastly, the negative  $Q_2$  values north of 15° N and above 800 hPa are likely associated with large-scale subsidence that may be a response to the widespread convective updrafts happening to the south.

In the 1800 UTC panel, some pockets of positive apparent moisture sink remain in the boundary layer north of 15° N, indicative of continued mixing and moisture flux divergence out of the low levels, and in the most intense convective elements around 7° N, showing net condensation and deposition in those thunderstorms. However, most of the rest of the domain is characterized by moistening at this hour. Contributions to this pattern are surely made by net evaporation and moisture fluxes associated with convective downdrafts, which are growing in coverage and influence by evening at low to mid levels, particularly between about 8° N and 15° N. However, as previously discussed with regard to the 0600 UTC plot, much of this negative  $Q_2$  may be due to the daytime dry bias in the sounding measurements. The widespread “moistening” at 1800 UTC may not be tied to any actual atmospheric changes, but instead could

reflect the switch from the daytime underestimation of humidity to more accurate observations at night.

The diurnal cycle of the divergence profile is illustrated by Figure 5.3. As was indicated by the discussion of Figure 4.9 in the previous chapter, the divergence structure in this region

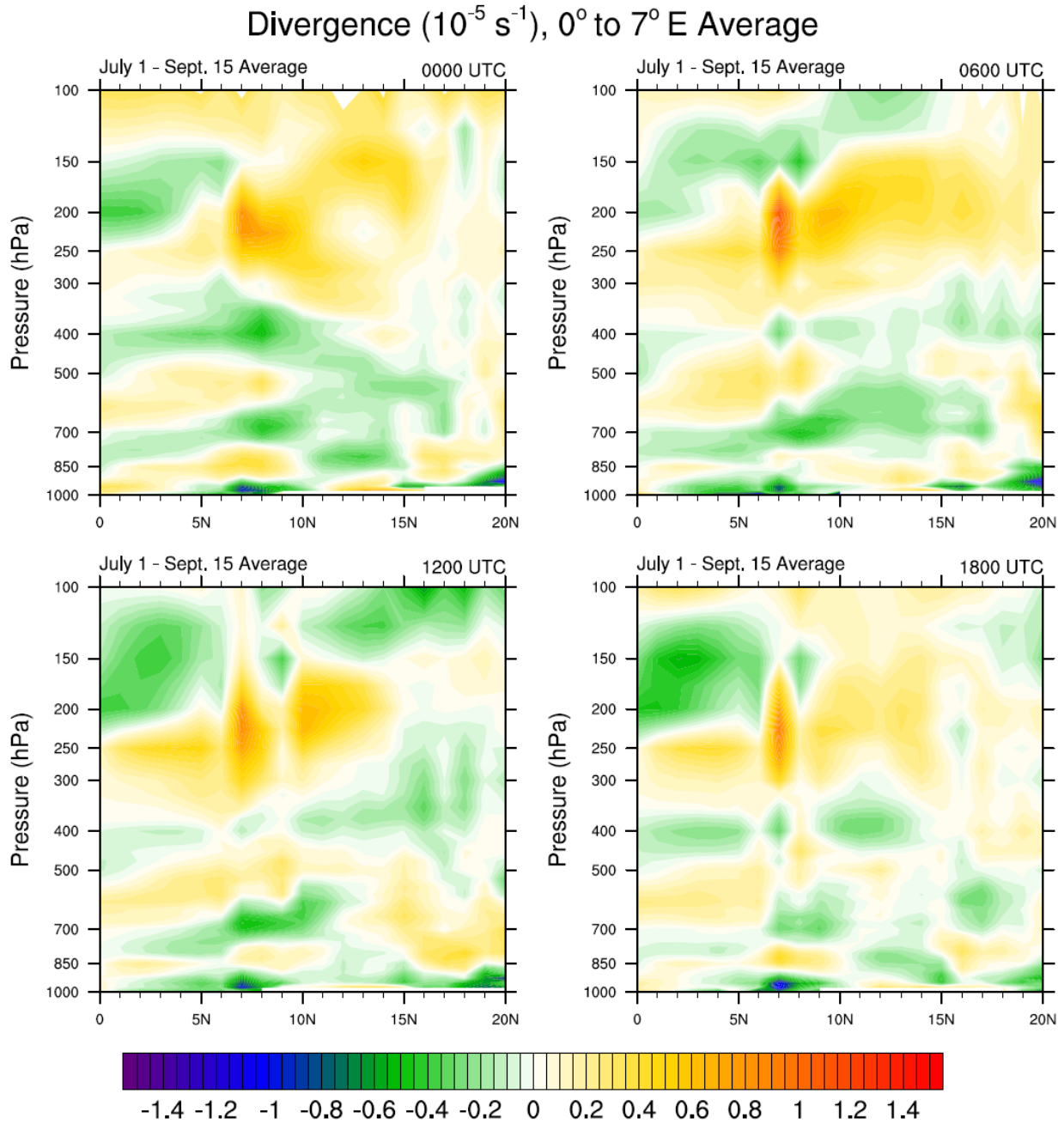


**Figure 5.3** As in Figure 5.1, but for divergence, in units of  $10^{-5} \text{ s}^{-1}$ .

appears very complex, with numerous alternating layers of time-mean convergence and divergence. This likely reflects the contributions from a diverse cloud population, with cloud tops, and the associated divergence, located at numerous levels throughout the vertical column. Overall, the divergence patterns are fairly consistent throughout the diurnal cycle – there certainly appears to be less temporal variation in divergence than in the structures of  $Q_1$  or  $Q_2$ . Nonetheless, some salient features will be pointed out. Near the coast and offshore, there generally appears to be strong near-surface convergence and strong upper-level divergence at the 200 to 300 hPa layer. In between are lower magnitude levels of divergence near 850 hPa and 500 hPa and of convergence near 700 hPa and 400 hPa. The major low-level convergence is suggestive of predominant rising motion in this area, likely aided by sea/land breeze activity and the proximity of hilly terrain. In turn, the strong upper-level divergence indicates the prevalence of deep convective updrafts, which corresponds nicely to the intense heating and drying depicted at this location by Figures 5.1 and 5.2. The intermediate divergence layers near 850 hPa and 500 hPa could represent, respectively, shallow upward motion associated with boundary layer mixing and the effects of small cumuli, and moderately deep upward motion connected with cumulus congestus and shower activity.

Farther inland, particularly between  $10^\circ$  N and  $15^\circ$  N latitude, the 0000 UTC and 0600 UTC divergence profiles are both characterized by a broad region of strong divergence at upper levels, appreciable convergence at mid levels, and a shallow layer of near-surface divergence. This three-layered structure is a signature of the stratiform precipitation regions of MCSs, which are prevalent and extensive during the overnight hours in this area. The pattern is associated with rising motion above the freezing layer and sinking motion below, yielding a convergence into the mid levels in between and divergence of the upward moving air aloft and of the

downdraft flow near the surface. The structures become more complex at 1200 UTC and 1800 UTC, though the upper-level divergence persists, indicating the continued importance of deep convective updrafts through the afternoon and evening, and a layer of divergence forms near 500 hPa, similar to the coastal pattern, which may be connected with shallower convection and showery precipitation. Also of note is that the upper-level divergence maximum and the mid-level convergence maximum occur at a higher altitude farther to the north ( $13^{\circ}$  N to  $15^{\circ}$  N) than they do closer to the coast ( $7^{\circ}$  N to  $9^{\circ}$  N). As was proposed in Chapter 4, this may signify that the convective systems in the Sahel region have more intense updrafts that can reach higher into the atmosphere than those farther south, and the increased height of the mid-level convergence as well illustrates that this effect may cause an entire MCS complex to have greater vertical scale.

Figure 5.4 depicts the vertical velocity distribution through the diurnal cycle. At midnight, deep rising motion is present around  $7^{\circ}$  N, suggesting ongoing convective activity, while a broad zone of upward velocities extends north to around  $15^{\circ}$  N latitude at mid and upper levels, with downward motion indicated at low levels, peaking in intensity around  $13^{\circ}$  N. This structure is suggestive of widespread MCSs, inclusive of both deep convective updrafts along with a widespread stratiform region. The superposition of the rising motion at all levels in the updrafts and the rising motion aloft and downdrafts below the melting layer in the stratiform region can yield this type of vertical velocity pattern, where rising motion through most of the column overlies a shallow layer of descent. Over the ocean and in the northern part of the domain, deep downward motion is present, which could be associated with compensating subsidence for the convective updrafts at the intermediate latitudes and/or radiative cooling.

The 0600 UTC structure shares many similarities with the 0000 UTC plot, though the area of rising motion aloft over land has expanded northward, consistent with the northward

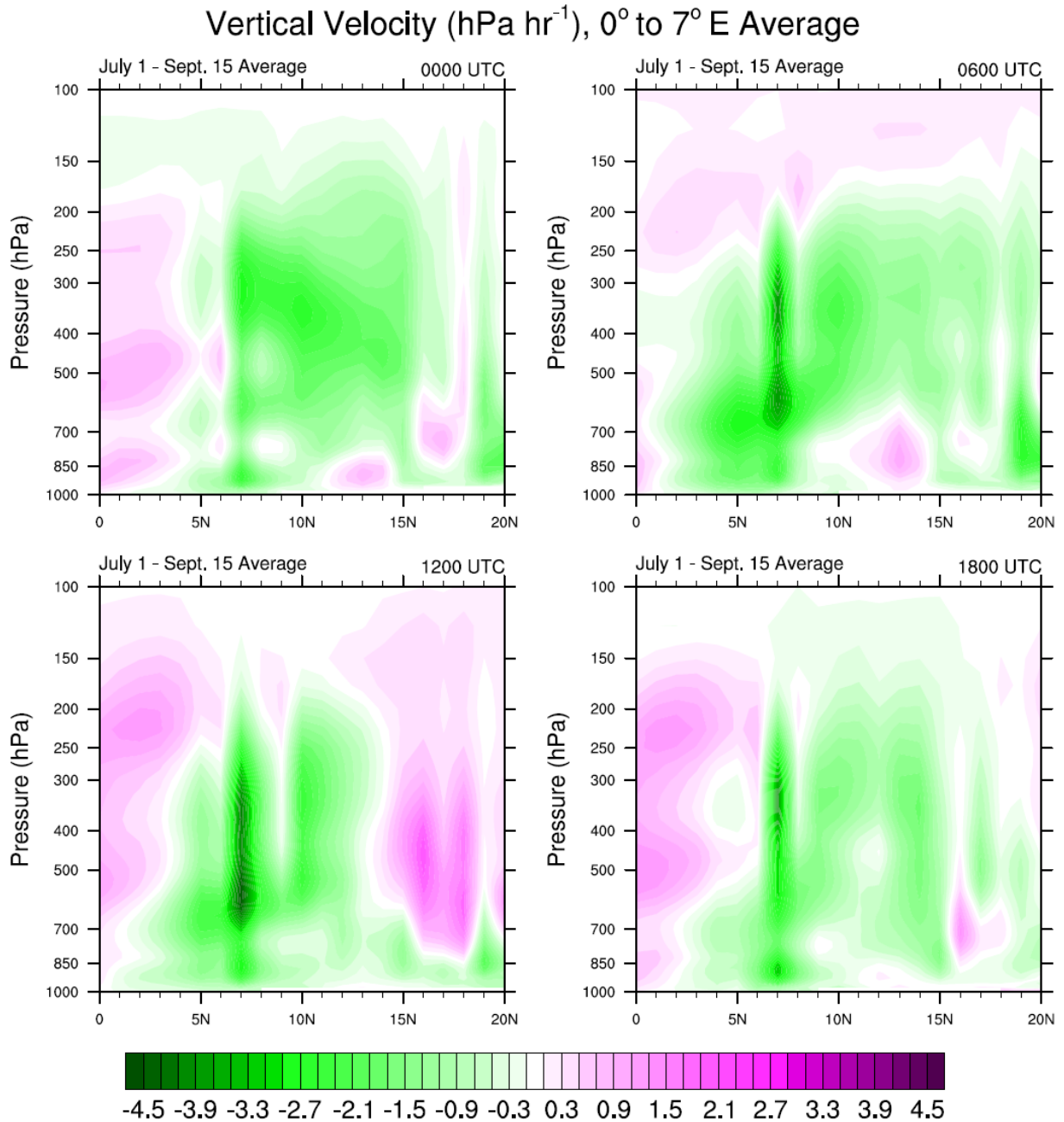


**Figure 5.4** As in Figure 5.1, but for vertical velocity, in units of hPa hr<sup>-1</sup>.

expansion of positive  $Q_1$  values at this time in Figure 5.1, and the zone of low-level descent between 11° N and 14° N has also increased in both depth and meridional extent. Both of these changes imply that the stratiform regions of the MCSs that propagate westward across the region overnight increase in coverage and magnitude by early morning while the convective updrafts

begin to decay. Additionally, the rising motion near the coast has intensified, in concert with the increasing heating and drying values discussed earlier in this chapter at that location, and moderately deep ascent has developed over the ocean, which matches the  $Q_1$  structure very closely and shows the development of shower and thunderstorm activity during the morning.

By noon, the moderately deep rising motion over the Gulf of Guinea generally persists, although the thickest layer of ascent is confined to areas near the coast and the magnitudes have decreased from the 0600 UTC values, particularly at low levels, suggesting that offshore convective activity is waning by midday and downdrafts are increasing in prominence. At  $7^\circ$  N, just inland from the coast, the strong upward velocities reach their peak amplitude and extend throughout the troposphere at 1200 UTC, indicating that the deep convection taking place in that region is at its maximum intensity. This pattern harmonizes well with the matching peak in positive  $Q_1$  in this same location shown in the 1200 UTC panel of Figure 5.1. Farther north, a second zone of relatively strong, deep ascent is found between  $10^\circ$  N and  $13^\circ$  N latitude, which also corresponds to a similar peak in positive apparent heat source at noon. Again, this latitude band lines up with the high terrain of the Jos Plateau, so the development of deep convection and rising motion would be expected in the area around midday. The magnitude of the upward velocities is minimal below about 700 hPa, though, so downdraft formation already looks to be well underway by this time. Both over the near-equatorial ocean and inland north of about  $14^\circ$  N latitude, descending motion predominates through most of the column, indicating a lack of noontime thunderstorm activity in those areas. As suggested previously, these regions of subsidence may well be a response to the large-scale ascent going on in the widespread convective updrafts occurring near the coast and over the more southerly continental locales. At

the lowest levels, rising motion prevails, particularly over the northernmost part of the domain where the deep daytime boundary layer continues to grow.

In the 1800 UTC panel of Figure 5.4, the strong, deep upward velocities around  $7^{\circ}$  N remain, indicative of persistent convective activity in the area, though the magnitudes have weakened somewhat from their 1200 UTC values. The rising motion near the coast has decreased substantially, suggesting showers and thunderstorms in that region are in decline. Meanwhile, the zone of subsidence over the ocean endures. Farther inland, deep ascent continues, though at lower amplitude than at 1200 UTC, while the low to mid level upward velocities have weakened further, and a small patch of downward motion has even developed near  $12^{\circ}$  N. Thus, while the convective activity evidenced in the noon plot looks to continue, it appears that updrafts have become less intense while stratiform precipitation takes on a more prominent role, a sign that the thunderstorms are organizing into more mature MCS structures. In addition, the areal coverage of these MCS-suggestive features has increased, with mid and upper level ascent encompassing nearly the whole land portion of the domain at 1800 UTC, and a major zone of sinking motion only occupying the low to mid levels near  $16^{\circ}$  N, which may now incorporate contributions from convective downdrafts.

Relative humidity values through the diurnal cycle are presented in Figure 5.5. The highest humidity figures tend to be located at low levels, which makes sense since surface processes like evaporation from bodies of water and transpiration from foliage are the sources of atmospheric water vapor. Additionally, there is a clear low-level meridional gradient in humidity, with the highest amounts of moisture over the ocean and near the coast, and the lowest amounts in the semi-arid and desert areas well inland. However, the positioning of this gradient varies by time of day. At 0000 UTC, there is a large, homogeneous region of high humidity over

## Relative Humidity (%), 0° to 7° E Average

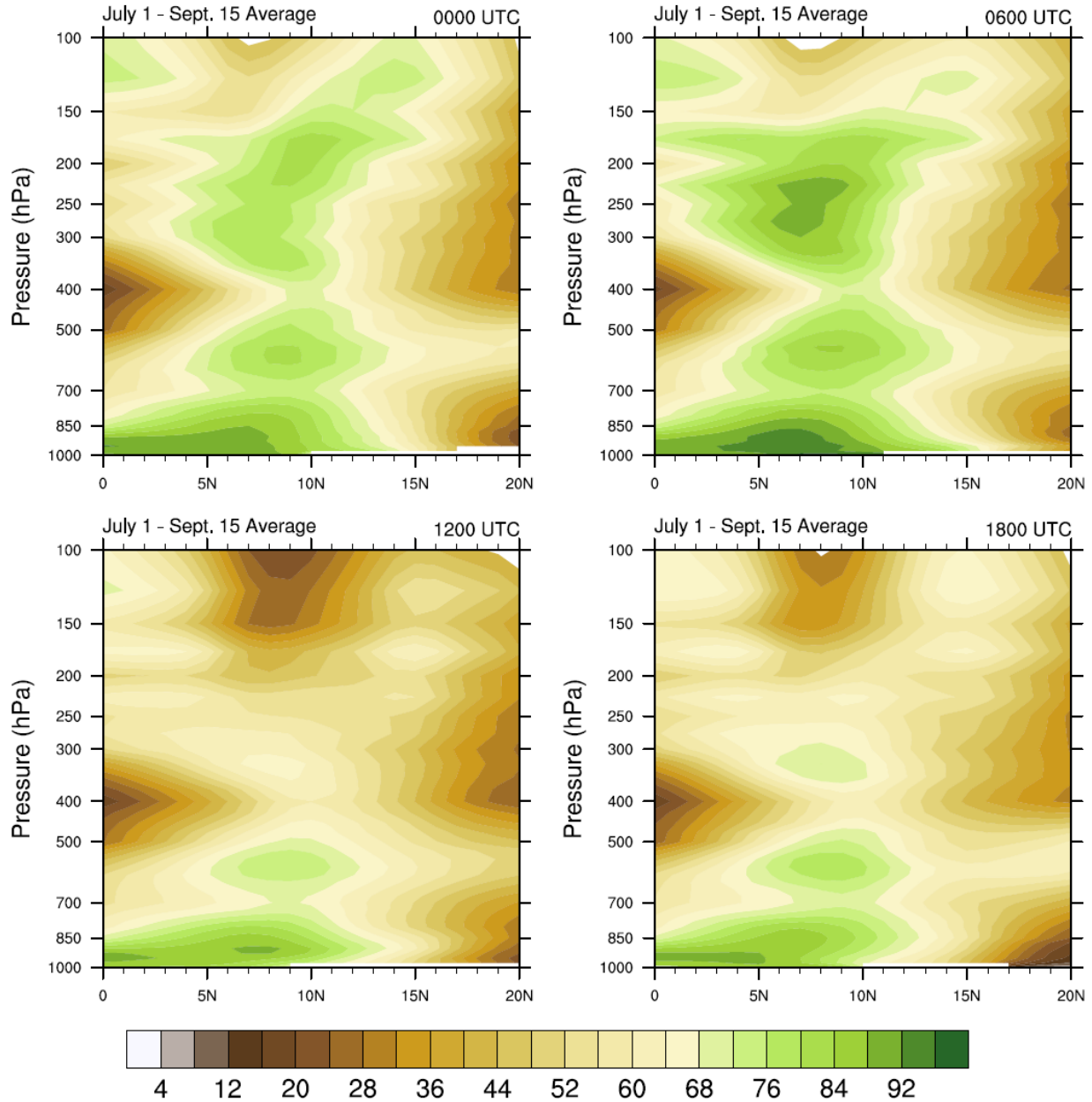


**Figure 5.5** As in Figure 5.1, but for relative humidity, in units of percent.

the ocean and north to 8° N latitude, while fairly moist conditions extend inland to around 13° N to 14° N. By 0600 UTC, humidity has increased further near the coast, which makes sense since this time also corresponds to the coolest part of the day. The northern edge of the moist air, though, has moved north as well, with a thin nose of high humidity extending all the way past

15° N just above the surface. By this time, the moist, southwesterly low-level jet has been blowing inland across West Africa all night, transporting water vapor northward and resulting in the most humid conditions of the day near the surface in the Sahel region. At noon, the low-level environment near and south of the coast remains moist, while the humidity has decreased appreciably north of 10° N latitude, and by 1800 UTC, the drier conditions inland have expanded farther south and increased in magnitude. This pattern matches well with the scenario described by Lothon et al. (2008) in this region, in which the nocturnal low-level jet, located just above the surface, brings water vapor from the south into the continental areas overnight, and daytime boundary layer fluxes and convective activity then mix the moisture over a greater depth of the atmosphere. Along with factors like boundary layer development and convection that transport moisture away from the surface, the warmer temperatures during the daytime would also tend to decrease relative humidity values even if water vapor mixing ratios remained constant. Lothon et al. (2008) surmise that the northward advance of moist conditions during the night associated with the low-level jet and the southward advance of drier conditions through the morning and afternoon connected with boundary layer mixing and convection are analogous to a dryline. However, they note that the environment in West Africa is quite different from, say, the Great Plains, since a strong low-level jet sets up nearly every night, even in locations far from the interface of the humid and dry air.

Other prominent features in the moisture fields shown in Figure 5.5 include a relative maximum in the humidity values at mid levels, around 550 to 600 hPa. It is plausible that this relatively moist layer could be associated with the effects of moderately deep convective elements or cumulus congestus type clouds that top out near this level and detrain water vapor. Some credence is lent to the possibility of this sort of moistening process by the fact that one of

the many layers of divergence illustrated by Figure 5.3 typically occurred at a similar altitude. However, it is also notable that this peak corresponds closely with the typical height of the 0° C level in this region, which is important since the relative humidity values were computed with respect to liquid water at temperatures above freezing but were calculated with respect to ice in below-freezing conditions. Since the saturation vapor pressure with respect to ice is lower than that with respect to liquid water at the same sub-freezing temperature, relative humidity numbers could increase simply due to the transition from a water-based to an ice-based formula even if water vapor amounts are unchanged. It is unclear, then, whether the mid-level humidity peak represents an actual moisture maximum or the change between a water-referenced and an ice-referenced regime at the freezing level.

There is also a relative maximum in humidity values aloft over the coastal and southern continental latitudes, with lower amounts farther south over the ocean and farther north toward the Sahara. This mid to upper level maximum extends as high as about 150 hPa during the nighttime, with greater magnitudes and meridional expansion by 0600 UTC. Such a pattern is suggestive of the widespread convective activity in the region, which takes the form of mature, propagating MCSs overnight, transporting moisture upward throughout the tropospheric column. The increasing upper level humidity values from 1200 UTC to 1800 UTC to 0000 UTC to 0600 UTC parallel the formation of thunderstorms around midday, with expanding coverage and improving organization through the evening, and the march of widespread precipitation systems across the domain overnight. The drying aloft between 0600 UTC and 1200 UTC corresponds to a time of decay for convective systems over land, with cold clouds reaching a minimum by late morning (Laing et al. 2008). Thus, reductions in upper level relative humidity over the continent during the morning hours make sense. However, this analysis must be qualified by considering

the daytime dry bias in the AMMA radiosonde humidity observations, which persists to a degree in the gridded dataset. It is unknown how much of the decrease in the relative humidity values between 0600 UTC and 1200 UTC, for instance, is attributable to actual changes in water vapor and how much may simply be a measurement error. Similarly, the increasing humidity amounts overnight likely combine legitimate moistening from thunderstorms with a return to more accurate readings after dark.

### **b. TRMM Precipitation Meridional Cross Sections**

Figure 5.6 presents north-south cross section plots of surface precipitation rate data from the TRMM 3B42 product. Like the previous figures in this chapter, the various panels represent rainfall estimates averaged at different points in the diurnal cycle, though the TRMM 3B42 product has a three-hour time resolution, so there are eight diurnal phases instead of the four used in the earlier diagrams. The eight specific time ranges used are simply those that were provided directly in the 3B42 dataset. For each time of day, the measurements were again averaged over the period from 1 July to 15 September 2006 and over the longitude band from 0° to 7° E.

Examination of this figure reveals a general correspondence between the precipitation estimates and the distribution and diurnal cycle of convective activity as established based on the AMMA radiosonde gridded data. During the time range centered on 0000 UTC, the maximum rainfall rates are located at 9° N to 10° N, with a broad peak from 7° N to 15° N, and a small offshore peak as well. By 0300 UTC, rainfall rates have increased in the Sahel strip, yielding a wide maximum from 8° N to 15° N. At the period centering on 0600 UTC, the greatest rain rates of the night occur between 11° N and 14° N, while precipitation wanes slightly to the south of

TRMM 3B42 3-hour Precipitation Rate ( $\text{mm day}^{-1}$ )  
 $0^\circ$  to  $7^\circ$  E Average, July 1 - Sept. 15 Average

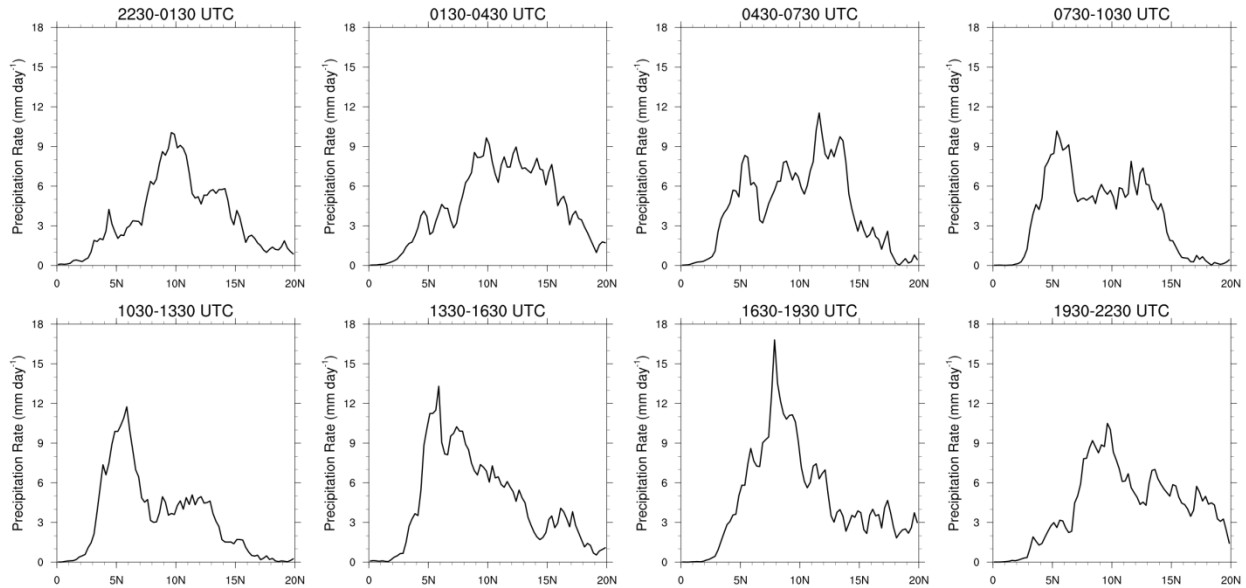


**Figure 5.6** Time-mean meridional cross-section plots of TRMM 3B42 three-hour precipitation rate, in units of  $\text{mm day}^{-1}$ , averaged at different points in the diurnal cycle. The eight panels each show the data from one three-hour period during the day. For each time range, the values were temporally averaged from 1 July to 15 September 2006 and spatially averaged over the  $0^\circ$  to  $7^\circ$  E longitude band.

that band and rain begins to increase around the coast. These distributions are largely consistent with the extensive propagating MCSs that move westward across the continental portion of the domain overnight, with large stratiform regions and widespread rainfall. During the 0900 UTC time range, precipitation values decrease inland, while a peak continues to develop near the coast, and by 1200 UTC, the coastal maximum has increased further in magnitude while continental areas between  $7^\circ$  N and  $13^\circ$  N experience their lowest rain rates of the day and regions north of  $13^\circ$  N are shown as receiving minimal precipitation. The patterns of the greatest rain amounts being found near the Gulf of Guinea shore during the morning and peaking in this area between late morning and midday are consistent with the typical diurnal cycle of showers and thunderstorms in that region. However, the apparent heat source and vertical motion profiles

shown previously indicated that robust and appreciably extensive convective activity was likely occurring inland as well by noon, particularly in the 10° N to 13° N band, where the TRMM 3B42 shows low precipitation values. During the afternoon, Figure 5.6 depicts increasing rainfall rates over the continent, though the values remain relatively low. The coastal precipitation maximum persists in the time period centered on 1500 UTC, while by 1800 UTC, the plot illustrates the greatest rain rate value of the diurnal cycle at about 8° N. At 2100 UTC, precipitation near the coast is now much lower, while a broad peak exists between 7° N and 11° N and appreciable rain rate values extend northward from there to the edge of the domain. The afternoon and evening comprise the phase of the day when convection is becoming better organized and more extensive as it moves from the initiation areas near high terrain and the Gulf of Guinea shore into other parts of the analysis region. The increasing areal coverage and gradually rising magnitudes of precipitation rates in the TRMM 3B42 data over the continental locations are consistent with this pattern.

Despite the links between the rainfall estimates in Figure 5.6 and the general diurnal cycle of precipitation in West Africa, some distinct and important differences exist between the TRMM 3B42 data and the picture painted by the AMMA gridded analysis. Perhaps the most obvious inconsistency is that the most intense heating rates in Figure 5.1 occurred at 1200 UTC, with deep heating predominating over a wide region between 5° N and 15° N latitude, while the peak 3B42 precipitation rate does not occur until the 1630-1930 UTC period, and midday and afternoon rainfall estimates are low over much of the continent. Even later in the evening and into the nighttime hours, the TRMM 3B42 estimates seem to show precipitation as being slower to develop and of lesser amplitude over continental areas than has been suggested by the AMMA data analysis. Similarly, rain near the coast and just offshore over the Gulf of Guinea seems to

persist longer into the afternoon and over a wider area in Figure 5.6 than the typical diurnal cycle of shower and thunderstorm activity in that location would suggest. The contrast between the AMMA apparent heat source values and the TRMM 3B42 rain rate estimates at 1200 UTC, in particular, suggests some sort of mismatch between the detection of thunderstorm activity by the 3B42 product and the convective signal revealed by the radiosonde observations. The fact that the peak 3B42 precipitation estimate occurs in the 1630-1930 UTC time range while the maximum  $Q_1$  values in Figure 5.1 appeared at 1200 UTC alludes to the possibility of a temporal lag in the TRMM estimates.

In order to investigate this discrepancy in more detail, precipitation feature (PF) records from the TRMM database provided by the University of Utah Tropical Meteorology Group were examined. As described in Chapter 3, this analysis uses Radar PF data, based on areas of surface precipitation as detected by the TRMM precipitation radar (PR), and Radar Projection PF data, based on the ground projection area of PR reflectivity greater than 20 dBZ at any vertical level. Like the previous datasets in this chapter, the PF values were averaged over the  $0^\circ$  to  $7^\circ$  E longitude band. However, since the gridded PF statistics have a monthly time resolution, data from all of July, August, and September 2006 were averaged together. While this differs from the 1 July to 15 September averaging period used in the earlier figures by the inclusion of the latter half of September, adding this time range should have minimal effect on the analysis, since it lies outside of the most convectively active portion of the summer monsoon phase in this part of West Africa. Plots of the TRMM 3B42 rainfall rate estimates, analogous to those in Figure 5.6, were computed for the whole 1 July to 30 September span (not shown) and confirmed this assessment, since both the spatial pattern and magnitudes of the precipitation values were nearly indistinguishable from those in the graphs using data from 1 July to 15 September. The TRMM

PF records were also similar to the 3B42 dataset in being divided into eight three-hour periods through the diurnal cycle. Unfortunately, the time ranges used in the PF dataset are offset by an hour and a half from those used in the 3B42 product, complicating their comparison somewhat.

North-south cross section plots of TRMM Radar PF precipitation rate data are presented in Figure 5.7. Many of the rainfall features in these estimates from the PR correspond well with the heating profiles calculated from the AMMA radiosonde analysis and the diurnal cycle of convective systems in the region. Around midnight, low to moderate rain rates exist across much of the 7° N to 15° N band, suggesting that stratiform rainfall may indeed predominate. Later in the night, a rainfall peak develops around 11° N, which is likely associated with the westward-propagating MCSs that cross the domain overnight. Precipitation then intensifies near the coast in the morning, with an offshore peak in late morning, along with continued rainfall inland. The timing of the rain rate estimates near and over the Gulf of Guinea matches nicely

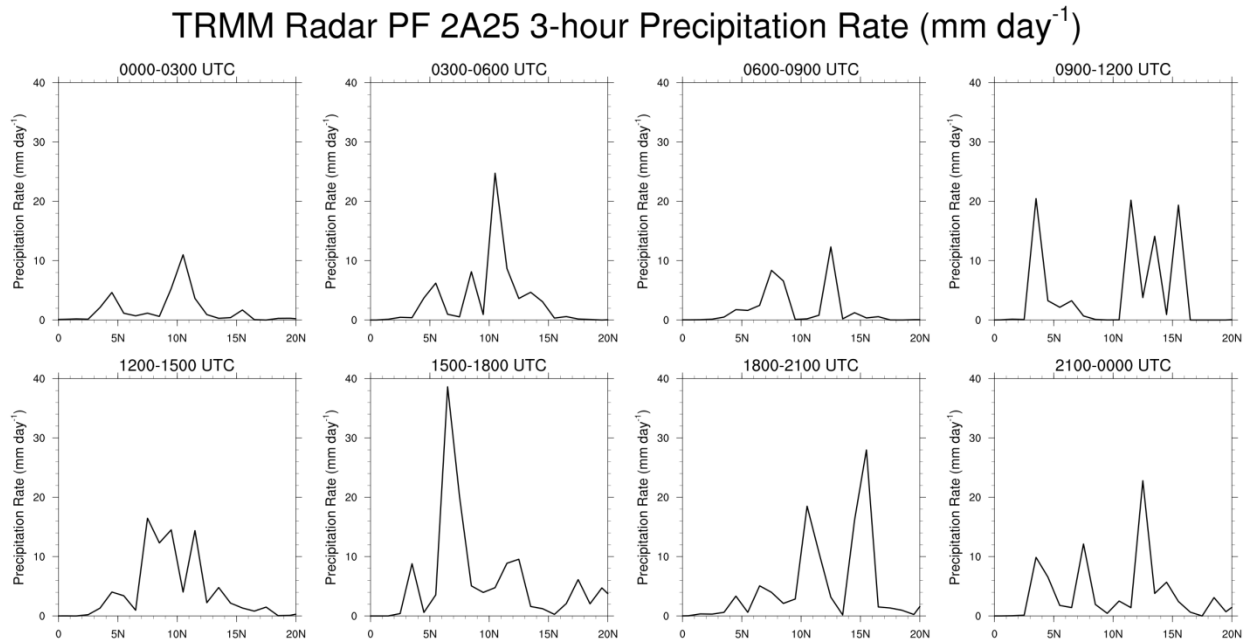


**Figure 5.7** Time-mean meridional cross-section plots of TRMM Radar PF three-hour precipitation rate, in units of mm day<sup>-1</sup>, averaged at different points in the diurnal cycle. The eight panels each show the data from one three-hour period during the day. For each time range, the values were temporally averaged from 1 July to 30 September 2006 and spatially averaged over the 0° to 7° E longitude band.

## TRMM 20 dBZ Radar Projection PF 2A25 3-hour Precipitation Rate (mm day<sup>-1</sup>)

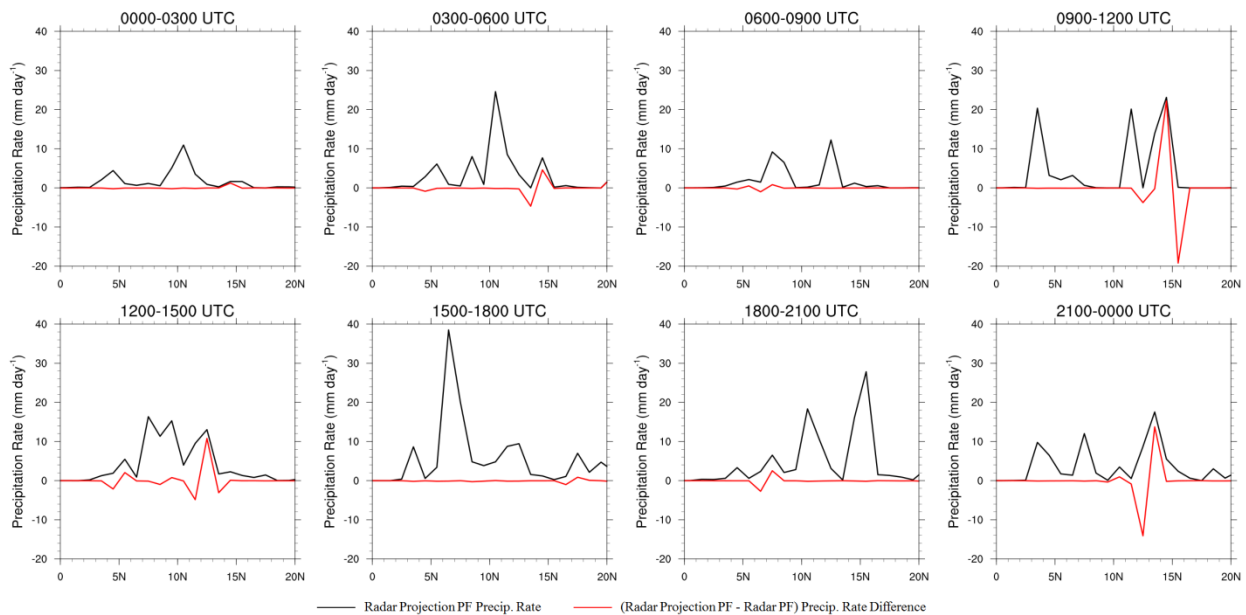


**Figure 5.8** As in Figure 5.7, but for TRMM Radar Projection PF three-hour precipitation rate, in units of mm day<sup>-1</sup> (black curves). The red curves show the difference between the Radar Projection PF and the Radar PF precipitation rate values; that is, the red curves are the black curves in Figure 5.8 minus the black curves in Figure 5.7.

with the expected diurnal cycle of shower and thunderstorm activity in that area. Precipitation is concentrated between 7° N and 13° N during the afternoon, coinciding with the deep convective heating structure in the region at that time, with a notable late afternoon peak just inland from the coast near 7° N latitude. Later in the evening, the greatest rainfall occurs from 10° N to 16° N, as MCSs organize and begin to proceed across the Sahel portion of the domain from east to west.

Figure 5.8 contains north-south cross section plots of TRMM Radar Projection PF precipitation rate data. In addition to the raw precipitation rate estimates, Figure 5.8 also depicts the difference between those Radar Projection PF values and the Radar PF amounts from Figure 5.7. The Radar Projection PF rainfall rates generally correspond well with the Radar PF figures, suggesting that most 20 dBZ echoes aloft in the analysis region are associated with surface precipitation as detected by the Radar PFs. In some cases, the difference curve in Figure 5.8 includes positive and negative anomalies of the same magnitude at adjacent grid boxes,

indicating a spatial shift of the Radar Projection PFs relative to the Radar PFs. As described in Chapter 3, the PF grouping algorithm assigns all rainfall associated with a single feature to the grid box where the PF centroid lies. Thus, the spatial shifting examples are likely scenarios where the centroid of a PF was located close to the edge of a grid box and inclusion of the projection area of radar returns aloft moved the centroid into the neighboring box. This suggests some meridional asymmetry or tilt in the structure of MCSs in this region between the surface and the upper levels, though no consistent patterns emerge from the changes shown in Figure 5.8. Sometimes, though, the difference curve indicates that the Radar Projection PF rainfall estimates are greater than those in the Radar PFs, such as near 12° N latitude during the 1200-1500 UTC period. This implies the presence of areas of PR reflectivity aloft that do not match with surface rainfall, due to non-precipitating anvils or the low-level evaporation of falling hydrometeors. The semi-arid Sahel location of the mentioned point and the heating profile structure in that area are both consistent with some low-level evaporation of rainfall.

Comparing the TRMM 3B42 rainfall estimates in Figure 5.6 with the TRMM Precipitation Radar-based PF estimates just discussed, the 3B42 product clearly has a spatially broader precipitation distribution and lower peak magnitudes than the PF data. This could be associated with the lower precision inherent in discerning cores of heavy rainfall by using infrared satellite measurements as a proxy, since cold cloud tops in convective systems spread out over a larger area than the updrafts and stratiform regions of precipitation occupy. Thus, the observations on which the 3B42 analysis is based provide a much less detailed, more “washed out” picture of thunderstorm activity than the radar images used in the PF database. This broader rainfall distribution in the 3B42 data is consistent with the results of Liu et al. (2007), who found that only 35 to 57 percent of the area of TRMM VIRS cold cloud features in their analysis

corresponded with PR-detected rainfall. That study also noted that land areas of central Africa had a relatively larger proportion of non-raining cold cloud area than the ocean regions they examined. However, it is important to point out that the PF data had a coarser horizontal resolution than the 3B42 data ( $1^\circ$  vs.  $0.25^\circ$ , respectively). This difference, along with the grouping of an entire precipitation feature's rainfall into its centroid's grid box in the PF database, could account for the sharper, more intense precipitation peaks seen in the PF plots compared to the 3B42 figure as well.

The TRMM PF data also fit more closely in several cases with the representation of the diurnal cycle of convective activity in the West African domain that is suggested by the AMMA data than did the 3B42 values in Figure 5.6. The greater rainfall amounts in the PF data during the early afternoon between  $7^\circ$  N and  $13^\circ$  N match the deep convective heating profiles at 1200 UTC in Figure 5.1 much more appropriately than do the low 3B42 numbers. Additionally, the maximum precipitation value near  $7^\circ$  N occurred during the 1500-1800 UTC time range in the PF data compared to 1630-1930 UTC in the 3B42 product. This earlier timing improves the correspondence with the peak heating rates that were seen at 1200 UTC in the AMMA dataset, but the most intense rainfall still occurs in late afternoon, not midday. Perhaps the  $Q_1$  values would be even greater at, say, 1500 UTC than they were at 1200 UTC, which would align more closely with the phasing suggested by the precipitation data, but the AMMA radiosonde data were only available four times per day, so such a conclusion must be left as a question for future research. The decrease in offshore rain rates by early afternoon in the PF dataset looks to agree more closely with the usual timing of shower and thunderstorm activity in that section of the domain than the 3B42 estimates that continued precipitation in the area into the afternoon. The greater PF rainfall values through the evening in the continental zone also look to harmonize

more closely with the expected intensity of precipitation associated with the organizing, widespread MCSs that cross the domain at that time of day than do the lower valuations in the 3B42 dataset.

The later timing of some of the rainfall peaks in the 3B42 product compared to the TRMM PF dataset may be associated with a delay between the maximum intensities of upward motion and precipitation in convective systems and the subsequent generation and spreading of a large, cold anvil. Since the area and brightness temperatures of cold clouds are used as proxies for rainfall magnitudes by infrared-based methods like the TRMM 3B42 algorithm, developing thunderstorms, which may have strong updrafts, heavy precipitation, and a high amplitude heating signal but a small horizontal cross section, would tend to have their rain rates underestimated in those datasets. On the other hand, more mature convective systems that have had time to create a widespread cold anvil would be diagnosed as producing intense rainfall, even if ascent and precipitation may well be weaker than earlier in the storm's life cycle. This possible mechanism to explain a time lag in infrared rain estimation products was suggested by the work of Liu and Zipser (2008), who found that cold clouds reached a maximum two to three hours later than surface rainfall over the tropical land regions in their study.

While the timing of the TRMM PF rainfall data seems to improve the alignment with the diurnal phasing suggested by the AMMA radiosonde gridded analysis relative to the TRMM 3B42 estimates, there are still some caveats that must be attached to this outcome. In particular, the one and a half hour shift between the time ranges used in the PF and the 3B42 products certainly complicates any direct comparison of precipitation details between the datasets. Additionally, even though PF statistics from a three-month period were used in this paper, this still represents a small sample size. This is because data from the TRMM PR is not continuously

available for a given region – observations can only be taken when the TRMM satellite is passing over the location of interest, and the satellite overflies a particular location approximately twice per day. Thus, many of the precipitation cases that are included in the continuous AMMA radiosonde and TRMM 3B42 analyses were inevitably missed by the PF dataset because the TRMM satellite was not overhead at the appropriate time. As long as the rainfall episodes that were sampled by the TRMM PR are representative of the entire population of precipitation systems in a statistical sense, this issue should not greatly skew the results, but there is no way to know if such a representativeness criterion happened to be met during July through September of 2006.

Despite the qualifications to this analysis, it still raises important issues that should be considered when choosing to employ an infrared-satellite based precipitation estimate product. These measurements are subject to inaccuracies in magnitude and areal coverage since cold clouds are only a proxy for intense rainfall, and for research involving the diurnal cycle, a substantial time lag is likely present in the data. Until additional remote sensing platforms are deployed, such infrared observations are often the best available source of information for much of the world, so they should certainly be used, but must be used with appropriate caution.

## CHAPTER 6

### MCS-RELATIVE HEATING, MOISTENING, AND VERTICAL MOTION

#### a. Case Selection

This chapter examines conditions relative to the passage of squall line mesoscale convective systems (SL MCSs) at the AMMA observation site in Niamey, Niger. This particular location was chosen because, as discussed in Chapter 3, the MIT C-band Doppler weather radar was deployed at the Niamey airport from July through September 2006. The frequent, high-resolution observations from this radar system provided the means to evaluate potential SL MCS episodes for inclusion in the following analysis much more precisely than elsewhere over the larger EBA region. In particular, the radar data permitted the selection of only intense, mature, and well-organized squall line events and allowed the time of MCS passage at Niamey to be discerned to within a five to ten minute period, neither of which would have been possible using, for instance, lower-resolution satellite measurements over the broader AMMA domain.

The selection of SL MCS cases for further study was greatly aided by a subjective case log compiled from the Niamey radar data, provided via personal communication by Rosana Nieto Ferreira. This log listed the date and time of significant convective episodes observed at the Niamey radar site, along with a brief subsection description of each thunderstorm system. The times in the log were used as a starting point to search for appropriate cases; each of the listed events was then examined in detail using the Niamey radar rain rate estimates provided by Nick Guy. As described in Chapter 3, that dataset comprises estimates of rain rate at 1 km elevation above ground level every ten minutes (the volume scan interval of the radar) within a 158 km radius of the Niamey airport (the scan domain of the radar). Maps of the rain rate values

were generated for times identified as MCS episodes in the subjective radar log, and the qualitative structure of the convective activity was then analyzed.

While no specific, objective criteria were used to choose or reject MCS events, the selected cases consisted of a solid or nearly solid line of intense rain rates at least 50 to 100 km in length. Intense precipitation was loosely defined as a substantial area of  $20 \text{ mm hr}^{-1}$  or greater rainfall rate, which is approximately equivalent to a reflectivity factor of 40 dBZ in the convective Z-R relationship used for this dataset. Systems comprised of widely scattered convective elements (numerous gaps on the order of the size of the thunderstorms cells or larger) or in which most of the convective line did not meet the rough intensity condition described above were not used in the analysis. Moreover, only events in which the main convective line actually passed through Niamey were used – squall lines that may have been intense enough and adequately organized but only skirted the edges of the radar domain and did not affect Niamey were not included. There was no special requirement for the convective systems to include stratiform precipitation of a certain size or intensity, but all of the chosen cases did include an adjoining region of stratiform rainfall along with the main convective line. Most of this stratiform precipitation was located behind the deep convective updrafts (a trailing stratiform configuration), though it also occurred ahead of the convective line in some cases (a leading stratiform configuration). Many of the chosen SL MCS cases extended beyond the range of the radar at one or both ends, so it is difficult to assess whether a parallel stratiform pattern was prevalent as well.

Once the events that qualified as SL MCS cases at Niamey based on the above size, intensity, and organization conditions were chosen, the precise time of passage for each system was determined using the radar rain rate maps as well. The time of passage for an MCS was

defined as the time when the Niamey radar site was located in the center of the intense convective line, as measured in the direction parallel to the system's motion. This center point was qualitatively determined based on the spatial extent of the highest, 20 mm hr<sup>-1</sup> or greater rain rates. In addition, despite the application of an attenuation correction algorithm to the reflectivity data before this precipitation rate dataset was computed, some attenuation at the greater ranges from the radar was usually apparent while the most intense rainfall was occurring at Niamey. Thus, the timing of the greatest attenuation of distant echoes was used as another aid in discerning when the most intense convective elements were passing over the Niamey site. For most of the cases, the radar site appeared to be at the center of the convective line during a single volume scan, and the time of that scan was then used as the time of MCS passage for that episode. In some instances, though, the center of the line had clearly not yet reached the radar in one volume scan but had already passed the site by the time of the next scan. In these cases, the time halfway between the times of the two relevant scans was assigned as the passage time.

Using the above procedures, twelve cases of robust, well-organized SL MCSs passing over the Niamey observation site were selected. The times of passage for these twelve cases were 0520 UTC 14 July 2006, 0650 UTC 17 July 2006, 0545 UTC 19 July 2006, 0940 UTC 22 July 2006, 1415 UTC 3 August 2006, 0810 UTC 6 August 2006, 0330 UTC 11 August 2006, 0845 UTC 18 August 2006, 0340 UTC 22 August 2006, 0240 UTC 28 August 2006, 1520 UTC 12 September 2006, and 0330 UTC 24 September 2006. Most of these SL MCS episodes reached the Niamey area during the early morning, between 0200 UTC and 1000 UTC, which is consistent with the overnight propagation of MCSs from east to west across the EBA regions and the location of Niamey toward the western side of this domain. However, two of the cases took place in the mid-afternoon, at 1415 UTC and 1520 UTC, illustrating that the typical diurnal cycle

of precipitation in this part of West Africa is not absolute and that exceptions and anomalies do occur with non-negligible frequency.

### **b. Composite MCS-Relative Vertical Profiles**

Figures 6.1 through 6.7 depict time series plots of the vertical profiles of assorted variables relative to the times of MCS passage at Niamey. The data in these plots represent the averages of the values at the two grid points in the AMMA radiosonde gridded dataset that are closest to the Niamey airport site. Specifically, data from the ( $13^{\circ}$  N,  $2^{\circ}$  E) and ( $14^{\circ}$  N,  $2^{\circ}$  E) points in the AMMA analysis were averaged to create these plots, as the Niamey airport is located at approximately  $13.49^{\circ}$  N,  $2.17^{\circ}$  E (Russell et al. 2010). The time coordinate used in the graphs is relative to the MCS passage time, and runs from 24 hours prior to 24 hours after the event. Time zero represents the MCS passage time as defined in section a, while negative time values correspond to the period prior to the MCS arrival and positive time values correspond to the period after MCS arrival. The quantities presented in Figures 6.1 through 6.7 are a composite, or mean, of the conditions in the twelve individual SL MCS cases.

Figure 6.1 shows the pattern of the  $Q_1$  apparent heat source relative to MCS passage at Niamey. Between 24 and 12 hours prior to the arrival of an MCS, this plot shows evidence of heating below about 850 hPa, while very slight cooling predominates through most of the rest of the vertical column. This pattern is reminiscent of the 1200 UTC  $Q_1$  structure north of  $15^{\circ}$  N latitude shown in Figure 5.1. As discussed in Chapter 5, the strong low-level heating is likely associated with the growth of the daytime boundary layer and the associated mixing and eddy heat flux convergence. In turn, the negative apparent heat source values aloft may be attributable to large-scale subsidence in response to upward mass transport by convective activity elsewhere

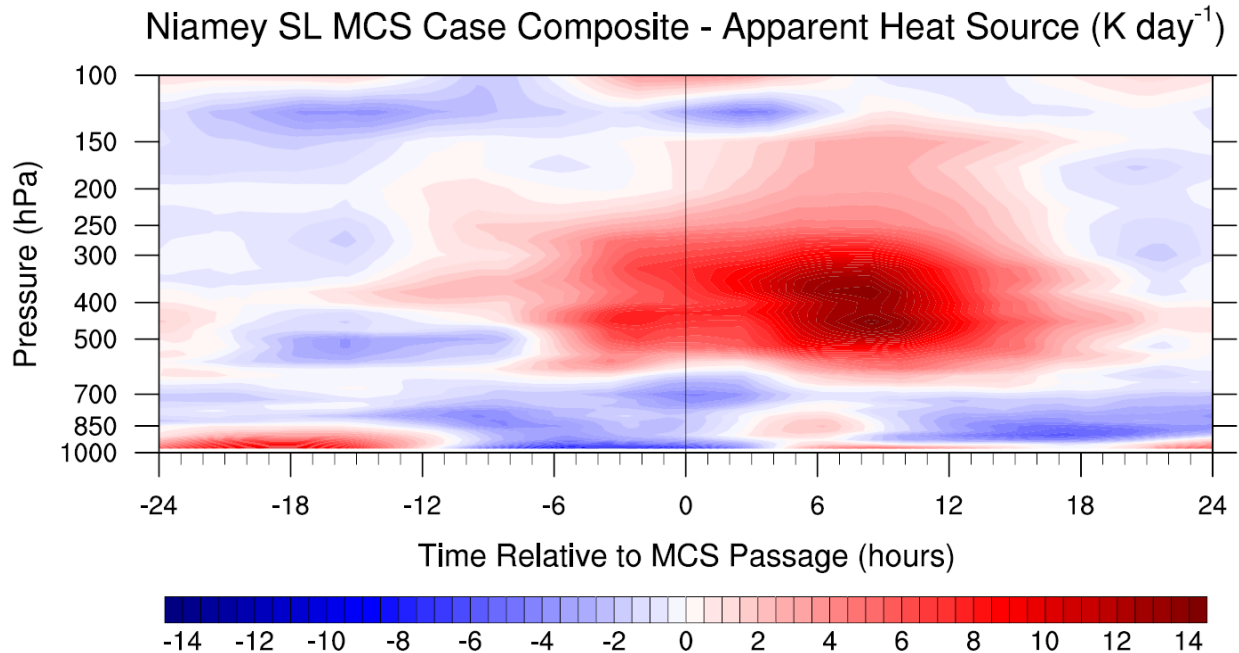


**Figure 6.1** Squall line MCS case composite time vs. pressure contour plot of the  $Q_1$  apparent heat source at Niamey, in units of  $\text{K day}^{-1}$ , derived from the AMMA radiosonde gridded analysis, relative to the time of system passage.

in the area. Since most of the MCS passage events included in this composite took place in the early morning, the period 24 hours to 12 hours beforehand would correspond to daytime the previous day, so the midday-like  $Q_1$  pattern matches expectations. Additionally, considering that the typical evolution is for convection to develop near the areas of high terrain well to the east of Niamey around midday, intensify and organize through the afternoon and evening, and propagate westward as a widespread MCS overnight and into the early morning, the thunderstorms that will eventually comprise the squall line that passes through Niamey are initiating elsewhere during this time. Thus, the presence of compensating subsidence aloft, indicative of developing convection in a nearby region, makes sense as well.

From about eight hours before MCS passage onward, a predominant stratiform structure of heating aloft above low-level cooling develops, with the dividing line between the positive and negative  $Q_1$  values between 600 and 700 hPa. The mid to upper level heating intensifies as

time goes on, with the maximum magnitudes between six and twelve hours after the squall line arrival. Between the time of MCS passage and about 17 hours later, the upper level heating deepens to around the 150 hPa level, while between zero and six hours after the system arrival time, a layer of cooling is evident above that, centered at around 125 hPa. During the time of maximum upper level heating, the apparent heat source at low levels also mostly switched to positive values, illustrating the superposition of a stronger convective-type deep heating structure on the pre-existing stratiform pattern.

Considering the extensive nature of stratiform precipitation regions in typical MCSs in this part of West Africa and the repeated indications of the predominant role of downdrafts, evaporation, sublimation, low-level cooling, and related phenomena throughout much of the analysis of this study, the prevalence of a stratiform  $Q_1$  structure in association with squall line passage at Niamey is not surprising. As mentioned in previous chapters, the change in the sign of the apparent heat source near the climatological  $0^\circ\text{C}$  level within this stratiform pattern also corresponds nicely with the configuration of the archetypal MCS model. The depth of the heating aloft, up to around 150 hPa, also speaks to the great intensity of convective activity in the region, as both the deep updrafts in individual thunderstorm cells as well as the mesoscale ascent in the adjoining stratiform zone look to extend high into the atmosphere. The area of negative  $Q_1$  even higher up, around 125 hPa, is likely associated with radiative cooling above the top of the extensive cold anvils that develop and spread out at upper levels in association with large, long-lived convective systems. Thus, the apparent heat source structure relative to squall line passage at Niamey largely conforms to expectations, with the exception of one strange timing issue. Namely, while one would anticipate observing an intense, deep heating maximum throughout the vertical profile of  $Q_1$  in connection with a convective line, such a feature only appears in the

apparent heat source composite in Figure 6.1 about three to four hours after the time of MCS passage, with the greatest magnitude at eight to nine hours after the arrival of the system. The vertical arrangement of this pattern, with the strongest heating aloft and lesser heating magnitudes at low levels, resembles the expected structure where a convective mode of heating throughout the troposphere and a stratiform mode of heating above cooling are combined. However, the presence of this heating setup would make sense at or close to the time when the main convective line passes a location, not several hours later.

A couple of possible explanations for the apparent delay in the timing of the deep convective heating signal relative to the actual time of MCS arrival at Niamey are both related to the fact that the dataset used in this analysis was derived from observations in a large-scale radiosonde array. First, since soundings were only conducted every six hours, data was generally not collected right at the time of MCS passage at Niamey, and in the event of a squall line arriving just after an observation was taken, the earliest measurements of the post-MCS environment would not be collected for several hours after the system had passed. Thus, it is possible that none of the soundings would be timed appropriately to sample the main convective line well, and in the event that the heating signal of the intense updrafts was detected by the first post-system observation, this may have only happened hours after the actual time of passage. In other words, the heating patterns may well have been produced by the squall line at physically reasonable times, but no observations were available to reveal them until hours later, with this detection delay causing features in the data to appear to have a time lag relative to the passage of the MCS. Since the system arrival times for the twelve cases used varied throughout the six-hour window between radiosonde launches, patterns affected by this sort of delay would not appear at any single discernible lag time, but would show up spread over a range of seemingly

late phases. The influence of the timing of the sounding observations and the lack of data during the “gap” between measurements will be explored further later in this chapter, but this factor could certainly play a part in causing the apparent delay of heating features in this analysis relative to the times when they would be expected with respect to MCS passage.

A second potential influence is the large-scale nature of the observational array used in creating the AMMA gridded dataset and the time ranges in which the effects of a convective system are communicated to the surrounding environment by gravity waves. Recalling the discussion from Chapter 2, Mapes and Houze (1995) described how mesoscale heating sources like MCSs create outward propagating temperature anomalies in association with the gravity waves excited by the systems. They note that the slower-moving, high-frequency wave modes generated by the storms tend to cause direct vertical motion and heating responses within the convective system that have the effect of cancelling them out, while the two lowest-wavenumber modes tend to predominate the impacts outside of the system itself. These modes comprise a deep heating response throughout the troposphere, which is the fastest propagating pattern (about  $50 \text{ m s}^{-1}$  in their model), and a warming above cooling structure, which moves at about half the speed of the first mode (about  $24 \text{ m s}^{-1}$  in their model). For a large-scale sounding array like that used in AMMA, with stations separated by hundreds of kilometers, the extensive heating signal associated with these gravity wave motions is really what is detected in the observations, and not the fine scale heating and cooling actually occurring within the convective system itself. Since it takes some time for the temperature anomalies to propagate over the hundreds of kilometers between radiosonde launch sites, there can be a delay of several hours between when thunderstorm activity happens and when the associated heating structure is picked up in the sounding measurements, even if the timing of the launch is perfect for capturing the signal. For

variables like divergence, vertical velocity,  $Q_1$ ,  $Q_2$ , and the like that include spatial gradients in their calculation, this is an especially important factor. Essentially, the indications of a given disturbance must reach all the stations surrounding a location under analysis by the time observations are taken in order for those effects to be reflected in the spatial gradients that are computed from the observational data and that feed into the aforementioned derived quantities.

Therefore, when using a dataset based on measurements from a large-scale sounding array, there can be a delay of a few hours between when a heating signal is produced by a convective system and when the effects have propagated across a wide enough region that they are detected by the set of observation stations. Combined with the discontinuous nature of the sampling by the radiosondes and the often sub-optimal timing of the launches with respect to the times of MCS passage at Niamey, these factors likely explain the apparent phase lag in the deep heating signal illustrated in Figure 6.1. However, while the deep convective structure shows up in the plot a few hours after the MCS arrival time and a stratiform structure predominates afterwards, these features are also preceded by a chiefly stratiform pattern starting six to eight hours before the squall line passage. This provides a reminder of the fact that real MCSs are not constant, isolated, idealized heating sources – they move, change in organization, vary in intensity, and interact with their environment throughout their evolution, so the textbook structure of a pure heating profile later followed by a neat heating over cooling shape is unlikely. In this case, the overwhelming prevalence of the stratiform signal suggests that the stratiform regions of the MCSs in this analysis are likely much more extensive than the convective lines and contribute more intensely to the net mesoscale effects of the systems as sampled by the radiosonde array. Since the heating anomalies associated with squall lines propagate away from the thunderstorms themselves, it is not surprising that a distinct pattern shows up in the  $Q_1$

profile hours before the system actually arrives. It is possible that the structure throughout the event is indeed a superposition of the deep convective and stratiform modes, but that the stratiform component is just more dominant or more widely observed by the soundings for most of the time, yielding the net cooling at low levels that is seen in Figure 6.1. Only when the convective line itself moves through the array is the deep heating mode strong enough to be detected in the observations, and this pattern then shows up in the composite profile a few hours after system passage for the above-described reasons.

The values of the  $Q_2$  apparent moisture sink relative to MCS passage at Niamey are provided in Figure 6.2. Prior to around nine hours before squall line arrival, the predominant signal in this plot is low to mid level moistening, below about 500 hPa. Then, for several hours around the time of MCS passage, there is a pattern of very strong low-level drying, below about 750 hPa, with continued mid-level moistening above that layer to near 450 hPa. Lastly, the profile transitions to one characterized by a deep zone of upper-level drying above 600 hPa

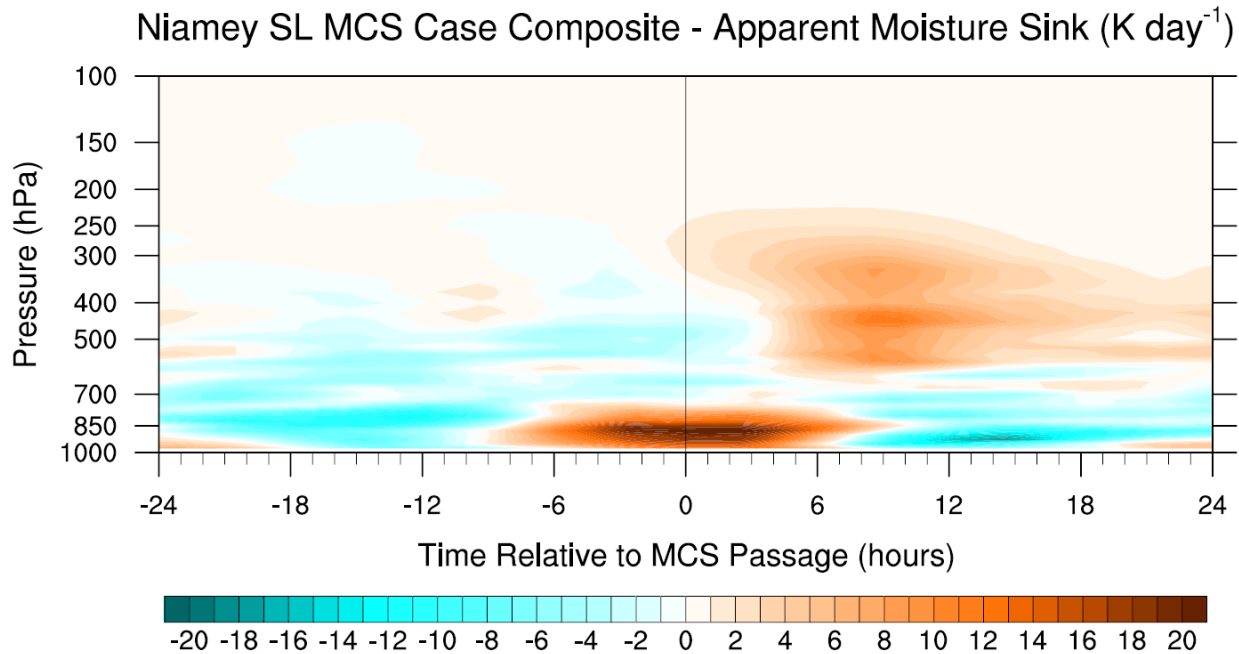


**Figure 6.2** As in Figure 6.1, but for the  $Q_2$  apparent moisture sink, in units of  $K \text{ day}^{-1}$ .

overlying low-level moistening, after about six hours past the time of system arrival. The moistening in the lower half of the troposphere before the MCS reaches Niamey makes sense from a perspective of preconditioning the atmosphere for deep convection. Processes like evaporation, transpiration, and moisture advection build up water vapor at low levels, which can then be drawn on to promote positive buoyancy and the formation of clouds and precipitation. In this region, advection associated with the near-surface southwesterly monsoon flow, and particularly northward moisture transport by the nocturnal low-level jet followed by mixing of the water vapor through the lower troposphere by the developing daytime boundary layer, are likely the most important means of this moistening.

Around the time of MCS passage, the strongly positive low-level  $Q_2$  looks to be an indicator of intense vertical moisture flux divergence, while the negative apparent moisture sink aloft would correspondingly suggest moisture flux convergence. Thus, this pattern may be associated with convective updrafts, in which water vapor is strongly being transported upward out of the low levels and into the mid and upper levels. Alternatively, the fact that  $Q_2$  changes sign at the relatively low level of 700 hPa and becomes low in magnitude above 400 hPa indicates that this upward transfer of moisture may be more associated with the low-level rising motion forced by the stratiform gravity wave mode propagating ahead of the MCS, which consists of adiabatic ascent in the lower half of the troposphere. The timing of this apparent moisture sink signal, starting eight to nine hours prior to the MCS passage time, matches well with the arrival of the  $Q_1$  signal of heating over cooling in Figure 6.1. This further suggests that the rising motion associated with the apparently strong upward moisture flux between the surface and about 400 hPa at this time may be forced more by the propagating stratiform gravity wave mode than by updrafts within the convective system itself. Whatever the precise attribution of

the upward moisture transport, the fact that the drying maximum is of much greater peak magnitude than the moistening maximum indicates that this flux divergence/convergence pattern may be superimposed on a background structure of positive  $Q_2$ . Such a pattern would be associated with net condensation, as would be expected in a scenario where moist air is being lifted and clouds and precipitation are forming.

Later, between three and nine hours after the MCS passage time, the low-level drying persists while a broad zone of upper-level drying develops, with a thin strip of moistening remaining at 600 to 700 hPa. This is the period when a more deep convective profile became apparent in the  $Q_1$  plot, and the apparent moisture sink structure looks to follow suit. The low and mid level pattern may indicate a continuation of the strong upward moisture flux described earlier, now more likely associated with thunderstorm updrafts themselves. The upper level drying and the general predominance of positive  $Q_2$  through the column suggest net condensation is present, which jives well with the deep clouds and intense precipitation connected with the convective system. Despite the prevalence of positive apparent moisture sink in the column, the persistent mid-level zone of negative  $Q_2$  now may not only be a sign of moisture flux convergence, but could also be aided by net evaporation just below the melting layer linked with downdraft formation.

After six to nine hours past the time of MCS arrival, the apparent moisture sink profile settles into a pattern of drying above 600 hPa and moistening below that level. This structure reflects the stratiform precipitation region of the disturbance, with net condensation aloft in association with the broad, weak rising motion at upper levels, and net evaporation below the melting layer connected with the downdrafts in that part of the system. Since the stratiform region is characterized by net formation and inflow of hydrometeors at upper levels and general

evaporation and sublimation thereof lower in the atmosphere, the  $Q_2$  signal can also be thought of as indicating a moisture flux from aloft to nearer the surface. This would correspond with the positive apparent moisture sink values above negative values seen in Figure 6.2, although this “flux” is substantially accomplished by falling precipitation that at least partially returns to the vapor phase at low levels, rather than the transport of water vapor only that would typically be thought to constitute a moisture flux.

It is also interesting to note that the apparent moisture sink signal that looks to be associated with the stratiform gravity wave mode propagating ahead of the MCS has a very different structure from the  $Q_2$  pattern within the actual stratiform precipitation region of the storm. As described above, the  $Q_2$  profile ahead of the system arrival is characterized by a strong near surface drying overlaid by moistening at mid levels, which could be associated with rising motion in the lower troposphere connected to the wavenumber-two gravity wave response acting on the previously-moistened low level environment. On the other hand, the apparent moisture sink structure within the stratiform precipitation region itself comprises deeper layers of drying aloft and moistening at low levels, with the change of sign occurring near the melting layer. This presents a sharp contrast to the  $Q_1$  patterns shown in Figure 6.1, in which both stratiform-forced signals, the pre-system gravity wave response and the precipitation region within the MCS, comprised deep layers of heating above cooling. Therefore, while the heating structures of the gravity wave modes forced by deep convection and stratiform precipitation may resemble those of the features driving them, the moistening profiles look to present significant differences that require a distinction to be made between the mesoscale effects of the propagating wave modes and the impacts of the MCS components that excite them.

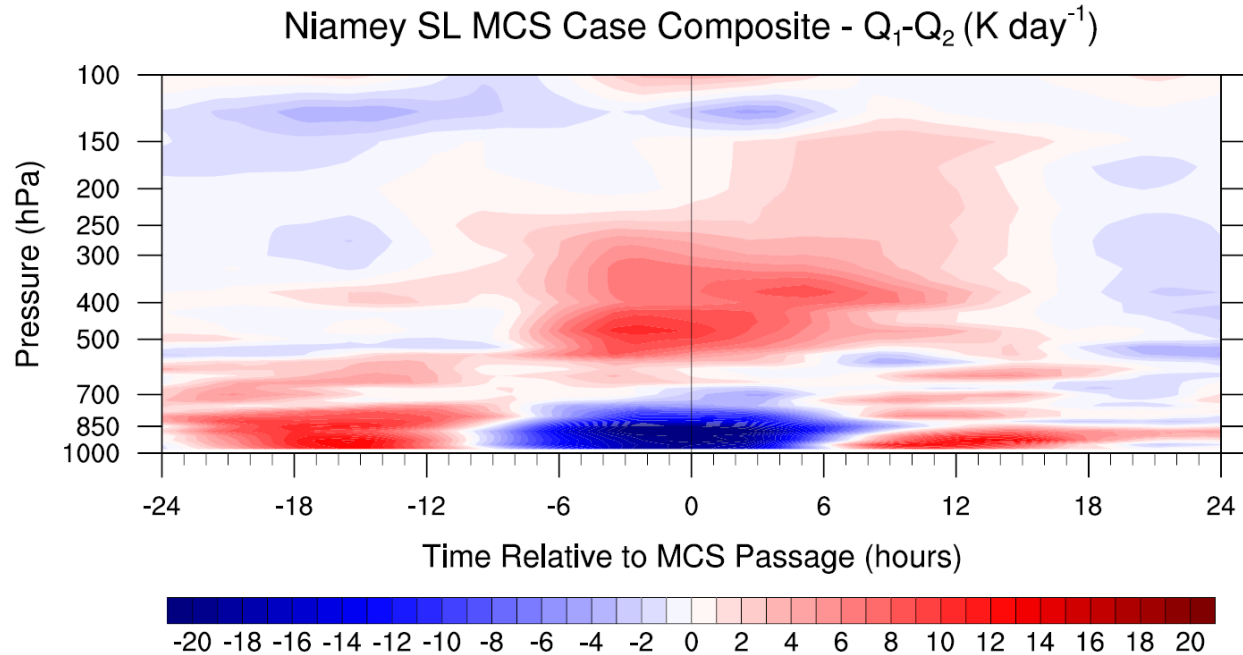


**Figure 6.3** As in Figure 6.1, but for the difference  $Q_1 - Q_2$ , in units of  $\text{K day}^{-1}$ .

Figure 6.3 illustrates the composite profile of the difference between apparent heat source and apparent moisture sink relative to squall line passage at Niamey. Recall from Chapter 2 that the difference  $Q_1 - Q_2$  can be interpreted as the sum of the radiative heating rate and the vertical eddy flux convergence of moist static energy. Before about ten hours prior to MCS arrival, the predominant signal is strongly positive  $Q_1 - Q_2$  at low levels, with especially great magnitudes below 750 hPa, and weaker positive amounts as high as 550 hPa. Higher in the profile, amplitudes are generally low. Although some radiative heating could be playing a role, this pattern mainly looks to indicate a potent flux convergence of moist static energy into the lower troposphere. As addressed in the previous discussion in this chapter, there seems to be a combination of heating and moistening near the surface in advance of the system, likely combining monsoon flow and the moist, nocturnal low-level jet with strong daytime heating and mixing to quickly ramp up moist static energy values in the lower troposphere. These factors work together to precondition the atmosphere for deep convection.

By around nine hours prior to system passage at Niamey, the  $Q_1 - Q_2$  values become strongly negative below 600 to 700 hPa, while a deep zone of positive  $Q_1 - Q_2$  is established above that layer. This pattern suggests intense moist static energy flux divergence at low levels and moist static energy flux convergence aloft, with the change in sign at mid levels approximating the location of the maximum upward eddy flux. Deep, moist convective activity tends to homogenize the vertical profile of moist static energy, transporting high values from near the surface into the mid levels, which typically have the lowest moist static energy in the tropospheric column, as well as into the upper levels, where moist static energy values again become high. The minimum moist static energy values in the EBA regions are located around 600 hPa in the time mean (not shown), so it makes sense that the strongest fluxes in association with processes working to establish a uniform moist static energy profile would be located near that layer. The relative roles of the gravity wave response ahead of the MCS and the thunderstorm system itself in causing this apparent deep upward transport of high moist static energy are difficult to discern from this figure. However, prior to the squall line arrival at Niamey, it is probable that the gravity wave modes would be the dominant forcing, while from the time of MCS passage onward, the updrafts within the thunderstorm complex would play a more important role. This change to a bigger influence of the actual squall line may be discernible by the fact that the positive values of  $Q_1 - Q_2$  aloft expand to a higher level around the time of passage and for about 12 hours following that point, indicating a deeper moist static energy transport that may be associated with the intense updrafts within the MCS. The level at which  $Q_1 - Q_2$  changes sign also shifts upward around the time of squall line arrival, apparently illustrating a deeper profile of saturated ascent and a higher altitude of the peak upward eddy

moist static energy flux within the thunderstorm system than in the gravity wave motions ahead of it.

Other interesting features in Figure 6.3 include the transition between positive  $Q_1 - Q_2$  values below about 150 hPa during the few hours following system passage and a zone of negative  $Q_1 - Q_2$  centered around 125 hPa. As addressed during the discussion of Figure 6.1, the area of negative values likely represents radiative cooling taking place atop the extensive cold anvil that forms and spreads out in the upper troposphere in association with a widespread, long-lived MCS. With this in mind, the region of positive  $Q_1 - Q_2$  just below may include contributions from the layer of radiative heating that is characteristically located near the bottom of such anvils, along with the effects of moist static energy flux convergence described previously. Lastly, between six and twelve hours after squall line arrival at Niamey, the upper level zone of positive  $Q_1 - Q_2$  gradually decreases in magnitude while a multi-layered pattern of positive  $Q_1 - Q_2$  returns at low levels. The redevelopment of positive values near the surface likely again reflects a vertical eddy flux convergence of moist static energy. Given all of the vertical transport just accomplished by the MCS, though, the contribution of fluxes from above this layer may well be more prominent than it was prior to the system, when sources associated with surface processes and horizontal advection were the major players.

Figure 6.4 presents composite temperature perturbation values relative to squall line passage at Niamey. To create this plot, the time vs. pressure temperature data were gathered for each MCS passage case, then at each pressure level, the time mean temperature of the analysis period (from 24 hours prior to 24 hours after squall line arrival at Niamey) was subtracted out. Thus, the temperature perturbation values represent anomalies from the time mean temperature at each vertical level over the 48-hour time range centered at the squall line arrival time. After

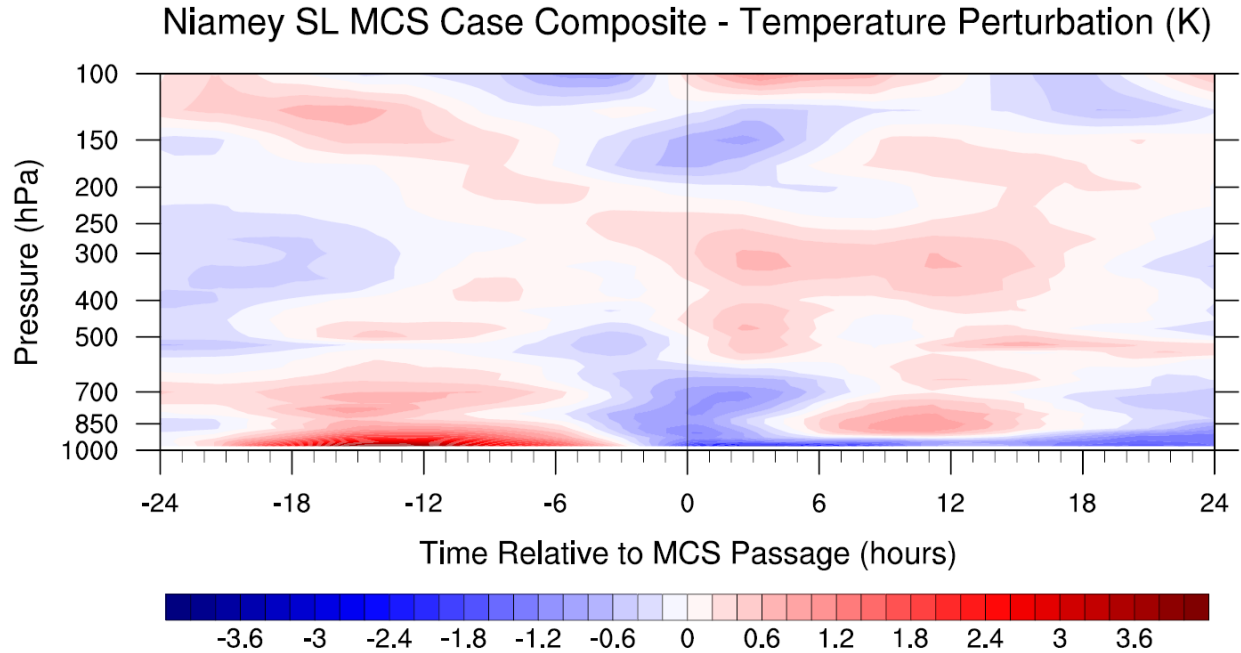


**Figure 6.4** As in Figure 6.1, but for the temperature anomaly from the time-mean temperature of the compositing period at each pressure level, in units of K.

the temperature perturbations were computed for each individual case, they were averaged to form the composite in Figure 6.4. It should be mentioned that since temperature is a point measurement and not a derived quantity involving spatial gradients like  $Q_1$  or  $Q_2$ , the delay between the time of MCS passage and when relevant features appear in the data should be somewhat less. The issues relating to the timing of the sounding launches relative to the system arrival and the frequent unavailability of an observation for several hours after the time of passage remain the same as described in connection with the  $Q_1$  field, so that portion of the timing lag will be unchanged. However, there is no requirement for a large-scale signal to have time to propagate to a number of neighboring radiosonde sites in order for the temperature to be measured accurately at Niamey. Since the temperature values used in this analysis are the average of two points in the gridded dataset and not raw sounding observations from Niamey, there will likely still be a slight influence of the data from other locations. Still, the portion of the timing delay associated with the period required for a large-scale signal to spread throughout

the AMMA array should be minimal for the temperature values. Overall, then, a lag of a few hours in connection with the observation timing matters will still exist, but the delay should be reduced somewhat compared to the  $Q_1$  and  $Q_2$  figures.

The most obvious temperature perturbation pattern prior to the MCS passage time is a low-level warm anomaly. This feature has the strongest magnitude very close to the surface, although appreciable warm values extend to near 600 hPa. This matches up with part of the low-level region of heating in Figure 6.1, so relatively high temperature would be expected there, and given the diurnal phasing of most of the MCS cases, the first portion of the warm anomaly period corresponds to the daytime, when warmer temperatures generally occur. However, this feature may not in fact be as much a warm anomaly as just an expression of the background conditions on which the low-level cool anomaly associated with the MCS is later imposed. Since half of the averaging period for the temperature data is, by definition, after the squall line passage, these warm temperatures may only be high compared to the low-level conditions within and behind the MCS and not represent a deviation from the usual temperatures in the area.

Beginning a few hours prior to MCS passage and lasting until about six hours afterward, the leading temperature perturbation structure is a cool anomaly below about 600 hPa, a warm anomaly between 600 and 200 hPa, and another cool anomaly above 200 hPa. This pattern looks to be a reflection of the stratiform gravity wave mode propagating ahead of the system, with contributions from the convective-scale updrafts and downdrafts likely in the later part of this time frame. As shown by Mapes and Houze (1995), the characteristic temperature structure of the wavenumber-2 response associated with the stratiform region of an MCS is indeed a cool perturbation in the lower half of the troposphere overlaid by a warm perturbation aloft, which is just what is observed in Figure 6.4. The cool anomaly at the uppermost part of the troposphere

would not be part of a wavenumber-2 mode, but such a temperature structure does appear in Figure 15 of Mapes and Houze (1995), which also includes several higher-frequency modes. In this case, the cool anomaly may be associated with the radiative cooling atop the MCS anvil that has been suggested by Figures 6.1 and 6.3, or it may be associated with another gravity wave mode of high wavenumber excited by the squall line. Evidence of the faster-moving wavenumber-1 mode, forced by deep heating in the main convective line of an MCS, does not obviously appear in the temperature anomaly field the way the stratiform pattern does. However, there is a very slight sign of a weak warm anomaly extending throughout the troposphere around seven to ten hours prior to the system passage time. Thus, it is possible that this is a reflection of the wavenumber-1 structure, which arrives in the sounding array earlier than the wavenumber-2 structure, but is of much lower magnitude due to the overall predominance of the stratiform portion of the MCS.

Between about six and sixteen hours after the squall line arrival at Niamey, the vertical profile is characterized by a general warm anomaly throughout the majority of the troposphere, between about 925 and 150 hPa, overlaying a very thin, but intense, cold anomaly below 925 hPa. The warm anomaly aloft can be explained by the extensive heating at upper levels associated with both deep convection and stratiform precipitation within the MCS. On a more fundamental level, thunderstorm activity works to stabilize the atmospheric profile, and warming aloft is consistent with and indicative of this outcome. The near-surface cool anomaly represents the cold pool generated by the saturated, convective-scale downdrafts in the squall line. This moist, low-temperature, high-stability layer is a well-known near-surface feature of organized convective systems (e.g. Zipser 1977), and Figure 6.4 indicates that it develops right around the time of squall line passage and persists even beyond the end of the compositing period. As

described in Chapter 4, Laing et al. (2012), among many others, found that organized, propagating MCSs in tropical Africa tend only to recur on multi-day time scales and usually not on consecutive days. In their study, some of the features preventing convection from surviving away from high terrain on the day following a squall line event were the persistence of long-lasting cold pools and low-level stabilization in the wake of heavy rain episodes. Figure 6.4 looks to support this concept of enduring, stable cold pools remaining well after an MCS has passed through the region. The mid-level warm anomaly between 600 and 925 hPa is a signature of the “onion shape” sounding that is characteristic of unsaturated mesoscale downdrafts occurring in the stratiform precipitation region of MCSs (Zipser 1977). As described by that study, these downdrafts are characterized by comparatively low humidity, even though precipitation is usually falling within them, and the evaporation of that rain contributes further to the negative buoyancy of the downdrafts. Despite the attendant diabatic cooling and moistening effects, substantial adiabatic warming connected with the unsaturated subsidence tends to cause a net positive temperature anomaly. The presence of this feature in Figure 6.4 and the indications thereof in the time-mean EBA-averaged temperature and dewpoint temperature profiles shown in Figure 4.7 comprise yet another illustration of the predominant role played by widespread stratiform precipitation regions and downdrafts within MCSs in West Africa.

The composite relative humidity values with respect to the times of squall line passage at Niamey are displayed in Figure 6.5. Like the temperature perturbations just presented in Figure 6.4, these relative humidity data represent point measurements and not quantities involving spatial gradients. Thus, the phase delay relative to the time of MCS passage will similarly be less than that in the earlier  $Q_1$  and  $Q_2$  plots, but still on the order of a few hours since the sounding timing issues remain. Prior to the time of MCS arrival, the atmosphere is generally

rather dry, with particularly low humidity values between 500 and 200 hPa. These dry upper-level conditions are typical for areas aloft in this semi-arid region outside of periods of convective activity. Of course, it must also be kept in mind that the daytime dry bias of the sounding observations could be contributing to the magnitude of the humidity minimum, but since the low values persist for nearly the whole 24-hour time range prior to squall line passage, the bias is likely not the primary factor. The lower levels are somewhat more humid prior to MCS arrival, and there are indications that the layer below 800 to 850 hPa is gradually being moistened with time. These slowly rising relative humidity values may well be connected with moisture advection into the region by the near-surface monsoon flow and the nocturnal low-level jet, especially since they increase more steadily in the last several hours before system passage, which generally corresponds to nighttime given the early morning phasing of most of the MCS cases. Of course, this predominant diurnal phasing means that near-surface temperature fluctuations between day and night could also contribute to the relative humidity changes even if

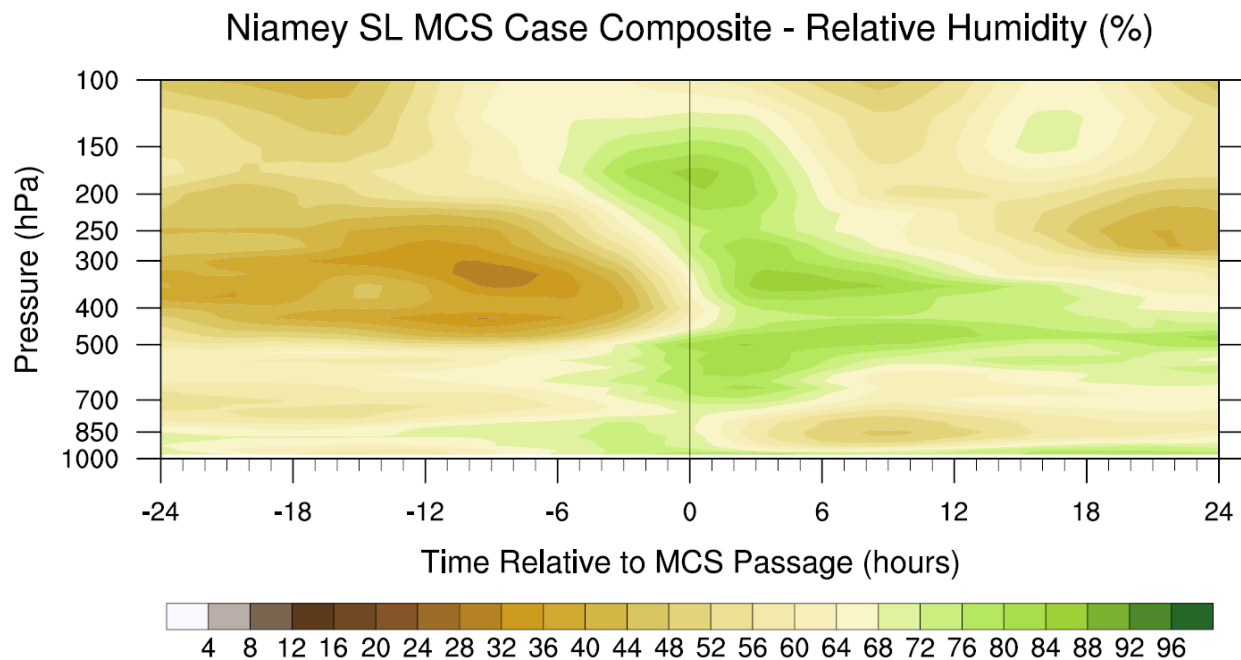


**Figure 6.5** As in Figure 6.1, but for relative humidity, in units of percent.

water vapor mixing ratios remain constant (e.g. lower temperatures at night with the same water vapor amounts would yield higher relative humidity).

Around the time of MCS passage, the whole tropospheric column has higher relative humidity values, which match well with the ongoing, deep, extensive cloudiness and precipitation associated with the squall line. It appears that the moist layer at low levels increases in depth with time as the squall line approaches, suggestive of gradually growing ascent ahead of the system rooted near the surface where the greatest moisture is found, a feature which could be associated with the stratiform-forced gravity wave mode ahead of the MCS arrival. Interestingly, the upper levels, between about 125 and 250 hPa, are also characterized by increasing humidity prior to the system passage time, which may be connected with moist outflow from the MCS anvil or even arrival of the anvil itself prior to the time when the main convective line strikes. The mean easterly winds aloft in this region coupled with the east to west propagation of the squall lines would be supportive of either relatively humid flow or the anvil itself extending to the west ahead of the system. The dry mid levels are the slowest to moisten with respect to the time of MCS passage. Thus, the squall lines may end up entraining some comparatively dry air at mid levels – while this can have a detrimental effect on the positive buoyancy of updrafts, it can also enhance the evaporation and sublimation that contribute to downdraft formation, which is clearly a key process in these systems.

Beyond a few hours after the squall line passes, the upper levels, above 300 to 400 hPa, gradually dry out, with fairly low relative humidity values returning by six to twelve hours after passage. The downward slope of the moist layer top as time progresses suggests that the stratiform regions of the MCSs gradually decline in height as one moves toward the back edge of the system. At mid levels, in contrast to the pre-squall line scenario, appreciable moisture

remains through the end of the compositing period, 24 hours after system arrival. This suggests that residual mid-level cloudiness can endure long after the thunderstorms and precipitation have moved on from the area, with little dissipation after a full day. Similarly, the thin moist layer very near the surface that corresponds to the cold pool from the MCS remains humid and persistent from around the time of system passage through the end of the analysis interval. As also discussed in relation to Figure 6.4, Laing et al. (2012) mentioned both residual cloudiness and long-lasting, stable cold pools near the surface as factors suppressing convection away from areas of high terrain on days following intense precipitation events. The other major feature apparent in Figure 6.5 following the MCS passage is the relatively dry conditions between 600 and 925 hPa. Like the low-level warm anomaly pointed out in Figure 6.4, the reduced relative humidity values are also a signature of an “onion shape” sounding induced by the unsaturated mesoscale downdrafts taking place within the stratiform precipitation zones of MCSs. Zipser (1977) specifically notes the relative humidity within these features can be as low as 40 to 50 percent, even as precipitation is ongoing, which matches well with the lowest values in Figure 6.5 between six and twelve hours after the squall line arrival time around 850 hPa. The prominence of this dry layer speaks yet again to the key role played by stratiform region downdrafts in determining the large-scale effects of West African convective systems.

Figure 6.6 shows the composite divergence profile with respect to the passage of MCSs at Niamey. Divergence is a derived quantity incorporating the computation of spatial gradients, so similar to the  $Q_1$  and  $Q_2$  plots earlier in this chapter, both sounding timing issues and the non-instantaneous communication of atmospheric changes to the large-scale array will contribute to the potential phase delay in this figure. Both lag-contributing factors will also be in play for the vertical velocity profiles to be displayed in Figure 6.7, since the vertical velocity is calculated

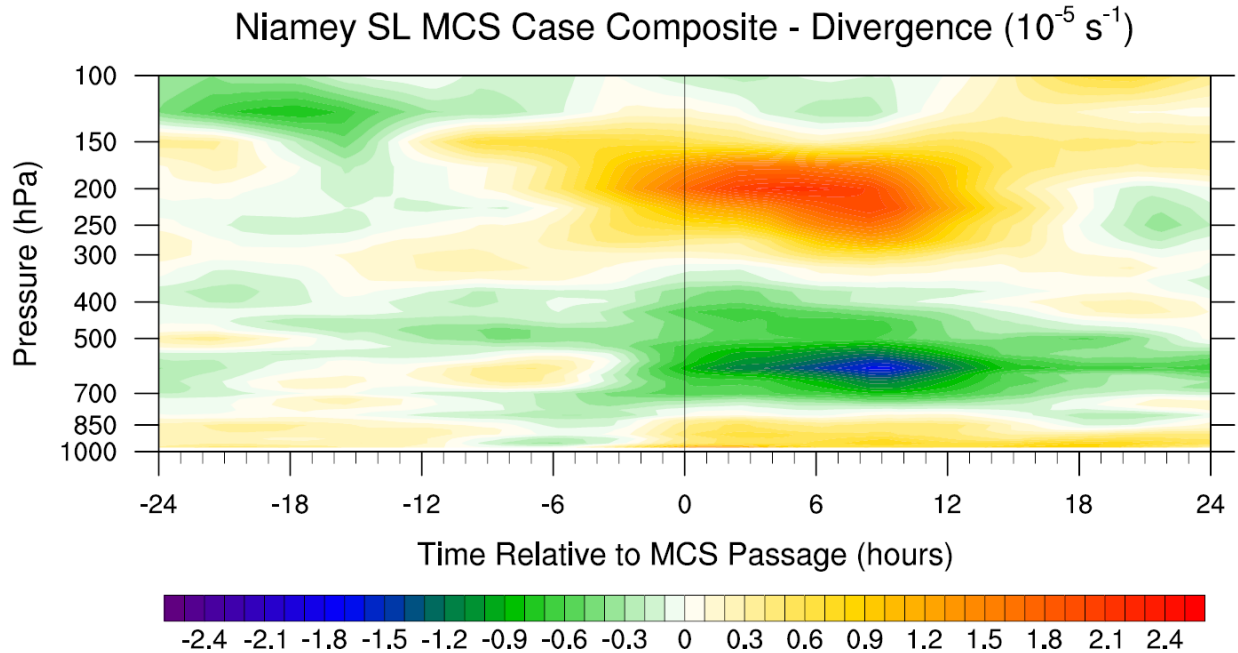


**Figure 6.6** As in Figure 6.1, but for divergence, in units of  $10^{-5} \text{ s}^{-1}$ .

primarily by integrating the divergence field. Between 24 and 12 hours prior to the time of squall line arrival, the divergence pattern consists of the usual multi-layered structure for this location, though the strongest features are a layer of convergence centered on 125 hPa and a near-surface zone of divergence. This arrangement would be associated with deep-tropospheric descent, so it may be related to compensating subsidence forced by the developing convection elsewhere in the region that will move into the Niamey area later. The divergence structure continues to look messy around six hours before the MCS passage, though there is now low-level convergence and mid-level divergence around the 600-hPa layer. This would correspond with rising motion and may be related to the lower-tropospheric ascent forced by the wavenumber-2 gravity wave mode propagating ahead of the system. However, this mode is also associated with upper-level downward motion, and excepting a thin convergence layer between 400 and 500 hPa, the upper troposphere is generally characterized by divergence at this time, so there does not appear to be any signal of such descent in this plot.

The most clearly prominent pattern in Figure 6.6 develops about three hours before the time of MCS passage and lasts through around eighteen hours after system arrival. This structure consists of intense divergence at upper levels, intense convergence at mid levels, and substantial divergence at low levels. This profile is the classical hallmark of a stratiform precipitation region within an MCS, with rising motion overlying sinking motion (e.g. Houze 1997). In the archetypal structure, the peak magnitudes of the mid-level convergence are located at the melting layer, since the melting, evaporation, and sublimation taking place near that level and the associated strong diabatic cooling, increase in hydrometeor fall speeds, and downdraft formation are the major factors forcing the convergence. Sure enough, in Figure 6.6, the convergence maximizes at 575 to 600 hPa, the climatological height of the 0° C level in this region. The strong upper-level divergence is associated with the rising motion in both the convective updrafts in the thunderstorm cores within the MCS and the mesoscale ascent taking place aloft in the stratiform zone. As mentioned previously in connection with Figure 6.5, the upper-level divergence peak does appear to descend somewhat with time after the squall line passage, suggesting that the stratiform region and anvil gradually decline in height moving toward the back edge of the system. This makes sense, as one would expect the intensity of the precipitation and the magnitude of the upward motion aloft to decrease the farther you move away from the main convective line. The low-level divergence is indicative of the prominent downdrafts occurring on a widespread, mesoscale basis within the stratiform precipitation area. Notably, even after the upper-level divergence wanes around 18 hours after system arrival, the mid-level convergence and low-level divergence remain in place through the end of the compositing period, suggesting that continued descent characterizes the lower troposphere even well after the thunderstorm complex itself has moved by.

Lastly, the composite vertical velocity structure in relation to squall line arrival at Niamey is illustrated by Figure 6.7. Prior to 12 hours in advance of the MCS passage time, the entire tropospheric column contains descending motion. As suggested previously, this feature may be indicative of compensating subsidence connected with the formation of deep thunderstorm updrafts elsewhere in the region, such as those that will move into the Niamey area later in the averaging period. It is also possible that this is evidence of the fast-moving wavenumber-1 gravity wave mode forced by deep convection, which comprises downward motion throughout the troposphere (Mapes and Houze 1995). However, the lack of evidence of this feature in most of the other variables does not make this a strong explanatory candidate. It is also conceivable that the downward velocities are associated with diabatic cooling, such as by radiation. The preponderance of weakly negative  $Q_1$  at most levels in Figure 6.1 at this time would match with this description as well.

Starting between six and twelve hours ahead of the squall line passage, rising motion develops at most all levels. As discussed with Figure 6.6, the low-level upward velocities around

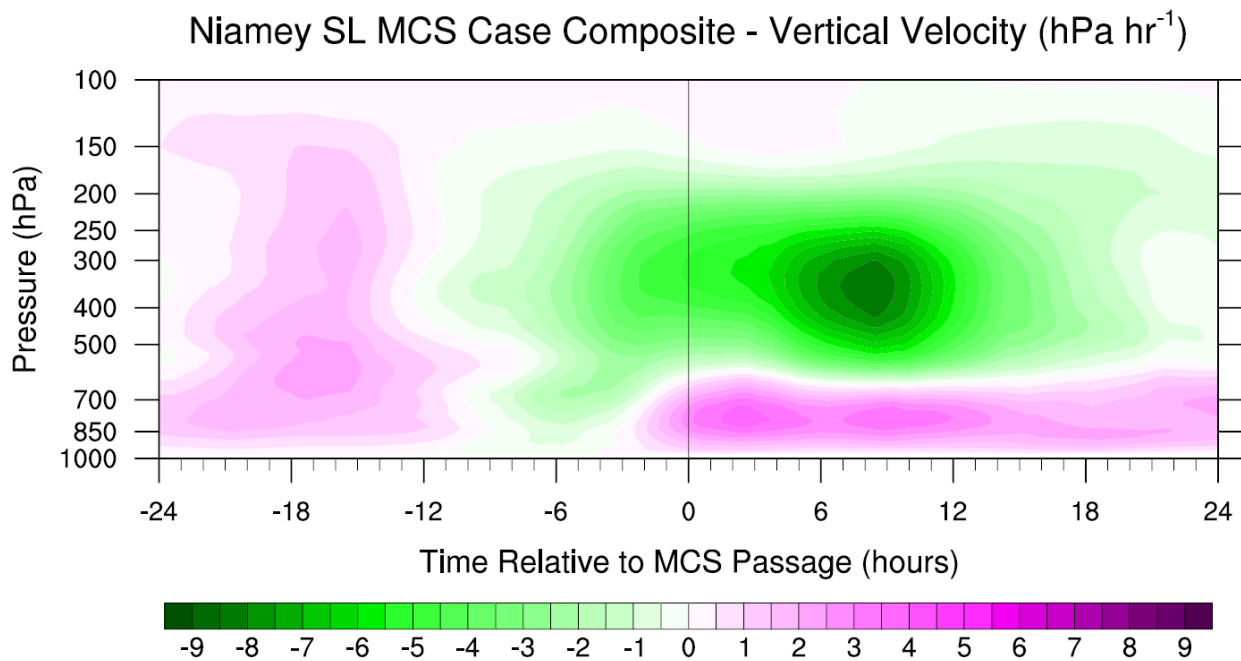


**Figure 6.7** As in Figure 6.1, but for vertical velocity, in units of hPa hr<sup>-1</sup>.

six hours before the MCS arrival may be forced by the wavenumber-2 gravity wave mode moving ahead of the system. On the other hand, this mode includes descent in the upper troposphere, which is not observed in the composite, where upward flow is emerging instead. Beginning around three hours before the squall line hits Niamey, a prominent pattern of rising motion aloft above sinking motion at low levels develops, with the dividing line between these regimes around the 600-hPa level. This structure also fits perfectly with the prototypical arrangement of vertical velocities in the stratiform precipitation zone of an MCS, and it is obvious how it was derived from the divergence layout shown in Figure 6.6. The change in the sign of vertical velocity near 600 hPa matches the peak in convergence associated with the melting layer, and the mesoscale updrafts above and downdrafts below are clearly discernible in Figure 6.7. The most intense rising motion at upper levels takes place between four and twelve hours after the system arrival time, and considering the phase lag factors discussed extensively in this chapter, it is likely that this represents the superposition of the deep ascent in the convective updrafts with the broad, less intense upward velocities throughout the stratiform precipitation zone. In a similar vein to the analysis connected with the divergence field, the upward velocities aloft weaken to low magnitudes by around 20 hours after MCS passage, but the downward motion at low levels persists with appreciable amplitude through the end of the compositing interval. Therefore, descent in the lower troposphere appears to outlast the presence of the thunderstorm complex itself in Niamey, putting a further damper on any attempt for convective activity to form during the day following a heavy precipitation episode.

### c. Individual MCS Cases and Discussion

As an illustration of the factors contributing to the apparent phase lag between the actual time of MCS passage at Niamey and when the physical signals of the thunderstorm activity are detected in the composite analyses just examined, Figure 6.8 contains time series plots of the vertical profiles of the  $Q_1$  apparent heat source for all twelve of the individual MCS cases that were composited to create Figures 6.1 through 6.7. The data points that were averaged and the squall line arrival-relative time coordinate that is used in Figure 6.8 are the same as those employed in the previous graphs in this chapter. In fact, Figure 6.1 is essentially the mean of the twelve panels in Figure 6.8. The dashed black vertical lines in each plot in Figure 6.8 depict the times of the sounding observations relative to that particular squall line case.

It is clear from looking at Figure 6.8 that the timing of the radiosonde launches plays a substantial role in the temporal structure of the  $Q_1$  profile. Any minima or maxima in time are inherently required to occur at the time of a sounding, as no additional observational information is available between those times. As a matter of fact, the data values presented between the analysis times every six hours are just a linear interpolation in the temporal dimension, as there is no way of knowing from this dataset what other trend pattern might exist. The strong changes that take place from one observation time to the next in these plots suggest that physically important transitions are occurring within those time ranges, but the data “gap” between soundings prevents any attempt to correlate their phasing precisely with the MCS passage. These plots also illustrate the fact that for many of the squall line cases, the first sounding after the time of arrival at Niamey was not launched until several hours later, preventing any hope of detecting the signal associated with the convective line’s passage until then. Even the timing issues shown by Figure 6.8 are further complicated by the fact that a balloon sounding takes

## Niamey SL MCS Cases - Apparent Heat Source ( $\text{K day}^{-1}$ )

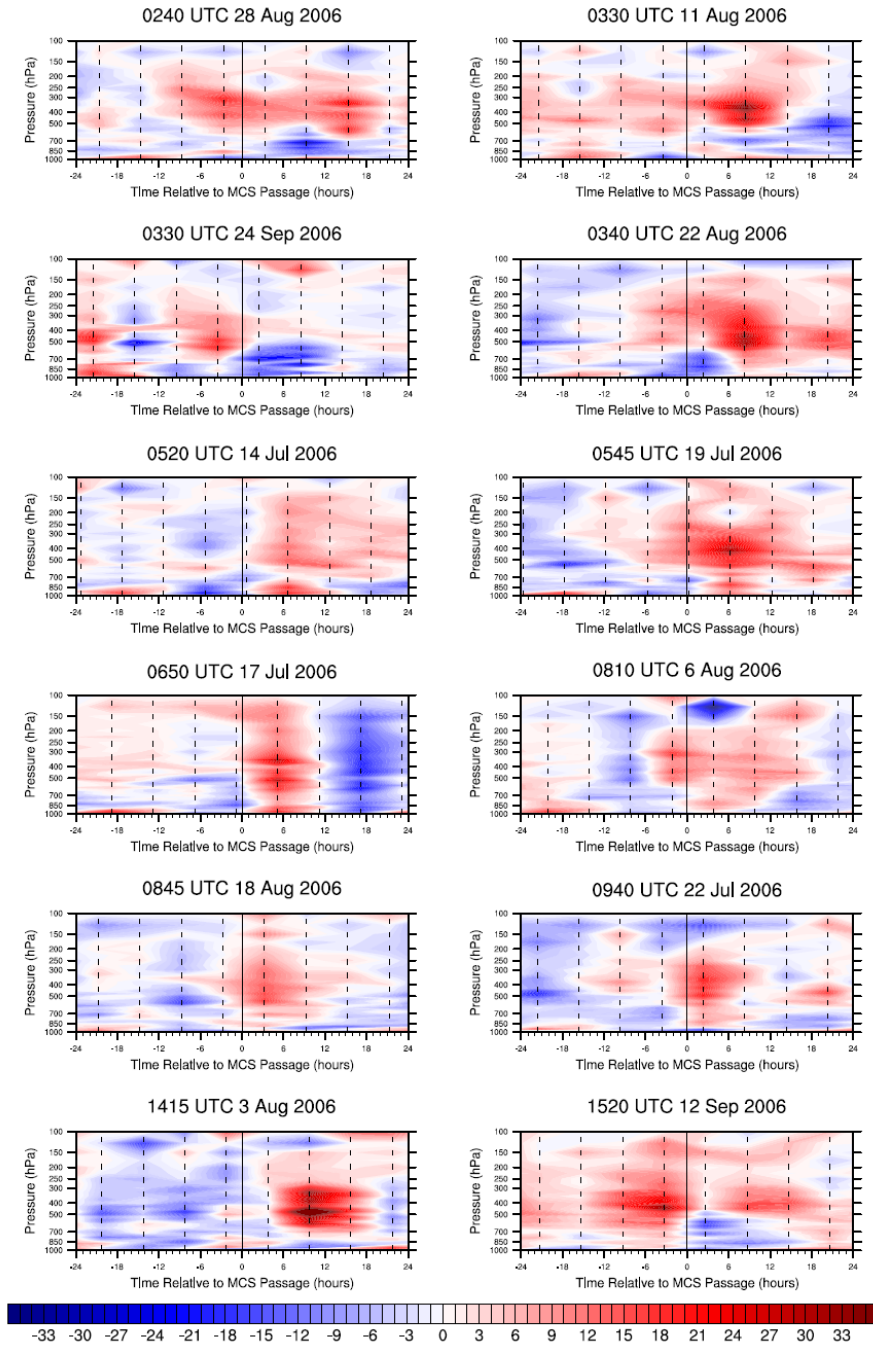


**Figure 6.8** Individual squall line MCS case time vs. pressure contour plots of the  $Q_1$  apparent heat source at Niamey, in units of  $\text{K day}^{-1}$ , derived from the AMMA radiosonde gridded analysis, relative to the time of system passage.

more than an hour to sample the entire depth of the troposphere, so observations taken by a single radiosonde actually span an appreciable range of times. In accordance with this reality,

soundings are typically launched 30 to 45 minutes before their nominal time, so that the mean of the interval of their ascent through the troposphere approximates the assigned time. With that in mind, observations with a nominal time that falls just after the passage time of an MCS may have in fact been launched prior to the squall line arrival, while the upper-level measurements may not have taken place until 60 to 90 minutes later! All of these complexities certainly muddle the precise interpretation of the timing of any of the features presented in this chapter, and given the apparent importance of the launch times in determining the temporal pattern of the profiles, these are significant issues.

Figure 6.8 also provides some evidence supporting the idea that the time required for propagating gravity waves to communicate the effects of a convective system to a large-scale sounding array contributes to the apparent phase delay. Namely, in several of the MCS cases, the most intense heating signal does not appear in connection with the first radiosonde observation after the time of squall line arrival at Niamey, but with the second observation. This implies that the apparent heat source pattern generated by the convective system had not had enough time to spread across the portion of the AMMA station array near Niamey by the first launch after its arrival, but adequate time had passed six hours later. Given the interval between soundings, when the effects of the MCS on the broader environment “miss” one observation time, this imposes a minimum delay of six additional hours on when those impacts will appear in the data. Therefore, this factor, linked to the physical mechanisms by which convective systems influence the large scale and the size of the AMMA radiosonde array, looks to play a major role in creating a phase lag between the actual time of squall line passage and when the consequences can be detected in the analysis.

The significance of African easterly wave disturbances for controlling the prevalence of convective activity in West Africa on multi-day time scales has been a recurring theme in this work. Accordingly, an attempt was made to examine the relationship between the intense, well-organized MCS cases at Niamey studied in this chapter and easterly wave troughs and ridges. Specifically, objective analyses of the vorticity fields computed from the AMMA radiosonde gridded dataset were utilized in the procedure described in Chapter 3, based on the work of Berry et al. (2007), to identify easterly wave trough and ridge axes for times surrounding each of the squall line arrivals. Unfortunately, while this method looked to do a commendable job picking out the easterly wave disturbances based on the vorticity distribution at each analysis time, there was very little consistency in the identified trough and ridge axes from one time step to the next. It was apparent that easterly wave activity of some sort was ongoing during the passage of ten of the twelve MCS cases, but the trough and ridge axes generally varied wildly in both location and magnitude from one sounding time to another, often appearing or disappearing altogether in a manner that seemed physically unrealistic. For most of the cases, there was no coherent feature that could be reliably tracked among the different analysis times to suggest the phase of an easterly wave in which the squall line was located. Perhaps this outcome should not be a surprise, given the often-noisy nature of observational data, and this may be an indication that the winds measured near the sounding stations were not actually representative of the larger region onto which they were aliased by the broad spacing between the radiosonde launch sites.

Despite the shortcomings of applying the easterly wave analysis procedure to the AMMA dataset, a few of the cases in which the easterly wave pattern was better defined are deserving of a brief mention. In particular, the MCS cases of 0545 UTC 19 July 2006 and 0340 UTC 22 August 2006 both took place ahead of an African easterly wave trough, while the cases of 0520

UTC 14 July 2006 and 0940 UTC 22 July 2006 occurred ahead of an easterly wave ridge. The two squall lines ahead of a trough both have a well-defined structure of positive apparent heat source over negative apparent heat source by six hours prior to MCS passage, followed by a strong deep heating signal seven to eight hours after system arrival, with an intense heating maximum around the 400 to 500 hPa level. During the remainder of the analysis period,  $Q_1$  generally remains positive through most of the column in these cases, with only weak hints of cooling near the surface. In the two MCSs that were located ahead of a ridge, there is also low-level negative  $Q_1$  in advance of the squall line arrival at Niamey, but the upper-level heating signal is weak to non-existent. A deep convective heating pattern likewise develops after system passage, though the amplitude looks to be appreciably weaker than in the pre-trough cases. Toward the end of the study interval, the positive  $Q_1$  aloft decays faster than in the systems ahead of a trough, while the cooling pattern at low-levels is deeper and more intense. Overall, there is some suggestion that the convective portions of the MCSs were stronger in the cases ahead of an easterly wave trough than in those ahead of a ridge, especially in terms of the magnitude of the deep zone of positive  $Q_1$  after system passage. The pre-trough cases also had a stronger heating signal aloft both prior to and after squall line arrival, though the low-level cooling structure was more prominent in the pre-ridge systems. Thus, areas of rising motion, both in terms of thunderstorm-scale updrafts and the mesoscale stratiform ascent at upper levels, seem to play a greater role in the MCSs ahead of easterly wave troughs, while downdrafts look to be more dominant in the squall lines ahead of easterly wave ridges. Given the large-scale forcing for ascent in advance of an approaching trough and for descent in advance of an approaching ridge, these relationships seem reasonable. However, it must be cautioned that these conclusions were drawn simply based on subjective analyses of the apparent heat source profile plots, with a

sample size of only two for each condition, so while sensible, the results are almost certainly not statistically significant.

## CHAPTER 7

### CONCLUSION

The investigations throughout the present work have revealed a number of factors that make weather systems in West Africa particularly interesting from the perspective of the broader tropical belt. On the seasonal scale, the north-south transitions associated with the West African monsoon comprise the predominant control on the location and intensity of precipitation. However, this general trend seems to be modulated by variations in convective activity at 25 to 60 day periods related to the Madden-Julian Oscillation. On shorter time scales of two to six days, African easterly wave disturbances look to be the principal factor governing the timing of rainfall events. One of the most distinctive traits of the study region in West Africa compared to other tropical areas is the particular prevalence of convective downdrafts, chiefly those associated with mesoscale zones of stratiform precipitation in thunderstorm complexes. These features, along with the gravity waves forced by their characteristic heating pattern, have an especially large influence on the time-mean atmospheric structure relative to the majority of the tropics. This unique situation may be connected with the continental setting of much of the region and the juxtaposition of deep moist convection near an expansive desert, both of which work to make the overall tropospheric profile drier than in many tropical locations. Cold pools and residual cloudiness generated by thunderstorm systems are particularly long lasting in this area as well, placing constraints on convective evolution on the days following a heavy rain episode.

The vertical patterns of atmospheric variables tend to be complex and multi-layered in West Africa, suggesting that the area is home to an especially diverse cloud population, with

contributions from numerous regimes prominent enough to influence the mean state. Meridional differences within the domain of this analysis also appear, including indications of more intense convective updrafts to the north, stronger effects of boundary layer mixing in the north, and a greater influence of MCS downdrafts toward the south. The diurnal cycle of precipitation in West Africa during the boreal summer is most prominently shaped by convective initiation near areas of high topography and the subsequent development and long-distance propagation of extensive, well-organized thunderstorm systems, though there seem to be effects related to diurnal flow patterns near the Gulf of Guinea coast too. Farther inland, moisture transport achieved by the nocturnal low-level jet is a key influence on rainfall, with mixing by the daytime boundary layer playing an important function as well. Changes in the relative contribution and intensity of deep convective and stratiform heating and moistening patterns are evident among different times of day and night, as the leading precipitation regime transitions from developing deep convection at midday to organizing thunderstorm systems by evening and propagating MCSs with extensive stratiform rainfall overnight. The distribution of subsidence outside of the convective regions also varies correspondingly through the diurnal cycle.

The present study has demonstrated both the incredible value of observational datasets and field campaigns to atmospheric science research and some of the challenges and caveats connected with using such measurements. For instance, the timing lag apparent in the MCS-relative vertical profile plots shows the difficulty of interpreting observations that are not optimally phased with the physical phenomenon being explored. The similar delay associated with the time required for gravity waves to communicate signals to a large-scale sounding array presents another complication when data is only available at widely spaced, discrete points. On the other hand, both the temporal and spatial resolutions of the AMMA datasets represent a vast

improvement over the operational meteorological network in West Africa, permitting the exploration of features such as MCSs with degrees of precision and accuracy that would otherwise be impossible. Similarly, the inconsistencies between time steps that were encountered when attempting to analyze African easterly wave trough and ridge axes relative to the MCS cases at Niamey may have been related to the often “noisy” or “messy” nature of observationally based datasets. Although smooth and consistent model output or reanalysis fields may be simpler to work with, there can be no guarantee of their realism without actual measurements for comparison. Moreover, forcing datasets from field projects are an important tool for model development and for the creation of parameterizations and algorithms that simulate the atmosphere and reproduce actual weather patterns as faithfully as possible. Therefore, despite their complexity, observational records have great value for both direct inquiries into atmospheric phenomena and the improvement of the models used to diagnose and predict them. The AMMA project, in particular, has proven uniquely important, given the antecedent sparseness of the available data in West Africa, combined with the significant impacts of the meteorological conditions in that region both locally and throughout the North Atlantic basin.

The analyses in this paper have also shown the usefulness of satellite remote sensing systems, as well as the caution that must be applied in interpreting their output. The delay evident in the TRMM 3B42 rainfall estimates relative to the timing that is implied by the AMMA radiosonde-based heating profiles and the TRMM PR precipitation feature database provides a prime example. The global network of geostationary satellites is a tremendous resource that supplies temporally and spatially continuous observations covering most of the Earth. However, like many remote sensing platforms, these satellites cannot directly measure all

of the parameters of interest (e.g. precipitation) and must instead use measurements that act as a proxy for them (e.g. cold cloud tops) to compute an estimate. These estimates, by nature, are only approximations, and especially when attempting to examine them near the limits of their resolution, they are subject to error. In the case of the TRMM 3B42 product, using cloud top brightness temperature to infer rainfall intensity appears to impose a lag of about three hours compared to the actual timing of the precipitation, and may overestimate its spatial extent while underestimating its localized magnitude. This should not be construed to indicate that infrared satellite rainfall estimates are categorically incorrect or unreliable, as they represent the best available method of precipitation measurement in much of the world where direct observations are absent. Especially at longer time scales (at least a day) and larger space scales (at least a few degrees of latitude or longitude) than were analyzed in this paper, the values can represent rainfall patterns quite well. However, as with any remote sensing product, the uncertainty level of the details of the data must be taken into account, and this study suggests that infrared satellite precipitation estimates may be relatively unsuitable for assessing the diurnal cycle of rainfall on a fine scale.

The work presented here suggests many potentially fruitful avenues for future research. The interesting outcomes of analyzing the vertical profiles of variables relative to MCS passage at Niamey entreat the examination of such profiles over a larger area of West Africa. In particular, comparing the results from Niamey with a location closer to the Gulf of Guinea coast could shed more light on the intriguing meridional differences that characterize this region. Moreover, looking at how the profiles change as the thunderstorm complexes propagate from east to west across the study domain would provide more insight into their development and evolution from initiation, to organization, to maturity, and lastly to decay. It would also be

helpful to discern a more coherent method for tracking of African easterly wave troughs and ridges through this area, so that the relationship between the heating structure of an MCS and its phasing with easterly wave disturbances could be investigated more robustly. If individual wave troughs can be tracked consistently from West Africa into the eastern Atlantic Ocean, it could also prove revealing to look into whether there are any differences in the heating structures over land that are associated with disturbances that develop into tropical cyclones once they emerge in the Atlantic compared with those that do not. Depending on how early in their evolution any such distinctions among easterly waves may appear, the patterns could serve as a valuable predictive tool regarding the chance that a developing disturbance will eventually spawn a tropical cyclone. Lastly, it would be useful to study the timing delay present in infrared satellite precipitation estimates, such as the TRMM 3B42 product, in a region with relatively high-quality and long-term “ground truth” observations of rainfall amounts. An area covered by the TRMM datasets that has had extensive measurements of precipitation using radars, rain gauges, and similar methods over a number of years would be ideal for such an inquiry, so somewhere like the southern United States could be a good candidate. This would allow a much more accurate quantification of the temporal lag, magnitude error, and spatial spreading connected with the infrared estimates than the more limited analysis in the present work.

## REFERENCES

- Agustí-Panareda, A., A. Beljaars, M. Ahlgrimm, G. Balsamo, O. Bock, R. Forbes, A. Ghelli, F. Guichard, M. Köhler, R. Meynadier, and J.-J. Morcrette, 2010: The ECMWF re-analysis for the AMMA observational campaign. *Quart. J. Roy. Meteor. Soc.*, **136**, 1457-1472.
- Berry, G. J. and C. D. Thorncroft, 2005: Case study of an intense African easterly wave. *Mon. Wea. Rev.*, **133**, 752-766.
- Berry, G. J., C. D. Thorncroft, and T. Hewson, 2007: African easterly waves during 2004 – Analysis using objective techniques. *Mon. Wea. Rev.*, **135**, 1251-1267.
- Burpee, R. W., 1974: Characteristics of North African easterly waves during the summers of 1968 and 1969. *J. Atmos. Sci.*, **31**, 1556-1570.
- Cifelli, R., T. Lang, S. A. Rutledge, N. Guy, E. J. Zipser, J. Zawislak, and R. Holzworth, 2010: Characteristics of an African easterly wave observed during NAMMA. *J. Atmos. Sci.*, **67**, 3-25.
- Duvel, J. P., 1990: Convection over tropical Africa and the Atlantic Ocean during northern summer. Part II: Modulation by easterly waves. *Mon. Wea. Rev.*, **118**, 1855-1868.
- Fulton, S. R., 2011: Finite difference formulas for derivatives at arbitrarily spaced points. Received via personal communication.
- Guy, N., S. A. Rutledge, and R. Cifelli, 2011: Radar characteristics of continental, coastal, and maritime convection observed during AMMA/NAMMA. *Quart. J. Roy. Meteor. Soc.*, **137**, 1241-1256.
- Haertel, P. T., 2002: Spurious divergence within objective analyses with application to TOGA COARE heat and moisture budgets. *Extended Abstracts, 25<sup>th</sup> Conference on Hurricanes and Tropical Meteorology*, Convection III, San Diego, CA, American Meteorological Society, 4B.2.
- Houze, R. A., 1997: Stratiform precipitation in regions of convection: A meteorological paradox? *Bull. Amer. Meteor. Soc.*, **78**, 2179-2196.
- Houze, R. A., 2004: Mesoscale convective systems. *Rev. Geophys.*, **42**, RG4003.
- Hsieh, J.-S. and K. H. Cook, 2007: A study of the energetics of African easterly waves using a regional climate model. *J. Atmos. Sci.*, **64**, 421-440.
- Huffman, G. J., R. F. Adler, D. T. Bolvin, G. Gu, E. J. Nelkin, K. P. Bowman, Y. Hong, E. F. Stocker, and D. B. Wolff, 2007: The TRMM multisatellite precipitation analysis

- (TMPA): Quasi-global, multiyear, combined-sensor precipitation estimates at fine scales. *J. Hydrometeorol.*, **8**, 38-55.
- Janicot, S., J.-P. Lafore, and C. D. Thorncroft, 2011: The West African monsoon. *The Global Monsoon System: Research and Forecast*, C.-P. Chang, Y. Ding, N.-C. Lau, R. H. Johnson, B. Wang, and T. Yasunari, Eds., World Scientific Publishing Co. Pte. Ltd., Singapore, 111-135.
- Johnson, R. H., 2011: Diurnal cycle of monsoon convection. *The Global Monsoon System: Research and Forecast*, C.-P. Chang, Y. Ding, N.-C. Lau, R. H. Johnson, B. Wang, and T. Yasunari, Eds., World Scientific Publishing Co. Pte. Ltd., Singapore, 257-276.
- Johnson, R. H., T. M. Rickenbach, S. A. Rutledge, P. E. Ciesielski, and W. H. Schubert, 1999: Trimodal characteristics of tropical convection. *J. Climate*, **12**, 2397-2418.
- Kiladis, G. N., C. D. Thorncroft, and N. M. J. Hall, 2006: Three-dimensional structure and dynamics of African easterly waves. Part I: Observations. *J. Atmos. Sci.*, **63**, 2212-2230.
- Laing, A. G., R. Carbone, V. Levizzani, and J. Tuttle, 2008: The propagation and diurnal cycles of deep convection in northern tropical Africa. *Quart. J. Roy. Meteor. Soc.*, **134**, 93-109.
- Laing, A. G., S. B. Trier, and C. A. Davis, 2012: Numerical simulation of episodes of organized convection in tropical northern Africa. *Mon. Wea. Rev.*, **140**, 2874-2886.
- Lau, K.-H. and N.-C. Lau, 1992: The energetics and propagation dynamics of tropical summertime synoptic-scale disturbances. *Mon. Wea. Rev.*, **120**, 2523-2539.
- Lebel, T., D. J. Parker, C. Flamant, B. Bourlès, B. Marticorena, E. Mougin, C. Peugeot, A. Diedhiou, J. M. Haywood, J. B. Ngamini, J. Polcher, J.-L. Redelsperger, and C. D. Thorncroft, 2010: The AMMA field campaigns: Multiscale and multidisciplinary observations in the West African region. *Quart. J. Roy. Meteor. Soc.*, **136** (s1), 8-33.
- Lin, X. and R. H. Johnson, 1996: Heating, moistening, and rainfall over the Western Pacific warm pool during TOGA COARE. *J. Atmos. Sci.*, **53**, 3367-3383.
- Liu, C. and E. J. Zipser, 2008: Diurnal cycles of precipitation, clouds, and lightning in the tropics from 9 years of TRMM observations. *Geophys. Res. Lett.*, **35**, L04819.
- Liu, C., E. J. Zipser, D. J. Cecil, S. W. Nesbitt, and S. Sherwood, 2008: A cloud and precipitation feature database from nine years of TRMM observations. *J. Appl. Meteorol.*, **47**, 2712-2728.
- Liu, C., E. J. Zipser, and S. W. Nesbitt, 2007: Global distribution of tropical deep convection: Different perspectives from TRMM infrared and radar data. *J. Climate*, **20**, 489-503.

- Lothon, M., F. Saïd, F. Lohou, and B. Campistron, 2008: Observation of the diurnal cycle in the low troposphere of West Africa. *Mon. Wea. Rev.*, **136**, 3477-3500.
- Madden, R. A. and P. R. Julian, 1972: Description of global-scale circulation cells in the tropics with a 40-50 day period. *J. Atmos. Sci.*, **29**, 1109-1123.
- Maloney, E. D., 2011a: Lecture 3: Atmospheric budgets: Dry static energy, latent heat, and moist static energy. ATS 742, Tropical Meteorology, Fall 2011. Department of Atmospheric Science, Colorado State University, Fort Collins, CO.
- Maloney, E. D., 2011b: Lecture 6: Tropical heating profiles and implications of weak temperature gradient balance for vertical motions. ATS 742, Tropical Meteorology, Fall 2011. Department of Atmospheric Science, Colorado State University, Fort Collins, CO.
- Mapes, B. E. and R. A. Houze, 1995: Diabatic divergence profiles in Western Pacific mesoscale convective systems. *J. Atmos. Sci.*, **52**, 1807-1828.
- Murphy, D. M. and T. Koop, 2005: Review of the vapour pressures of ice and supercooled water for atmospheric applications. *Quart. J. Roy. Meteor. Soc.*, **131**, 1539-1565.
- Nieto Ferriera, R. and W. H. Schubert, 1997: Barotropic aspects of ITCZ breakdown. *J. Atmos. Sci.*, **54**, 261-285.
- O'Brien, J. J., 1970: Alternative solutions to the classical vertical velocity problem. *J. Appl. Meteorol.*, **9**, 197-203.
- Pytharoulis, I. and C. D. Thorncroft, 1999: The low-level structure of African easterly waves in 1995. *Mon. Wea. Rev.*, **127**, 2266-2280.
- Redelsperger, J.-L., C. D. Thorncroft, A. Diedhiou, T. Lebel, D. J. Parker, and J. Polcher, 2006: African Monsoon Multidisciplinary Analysis: An international research project and field campaign. *Bull. Amer. Meteor. Soc.*, **87**, 1739-1746.
- Reed, R. J., D. C. Norquist, and E. E. Recker, 1977: The structure and properties of African wave disturbances as observed during phase III of GATE. *Mon. Wea. Rev.*, **105**, 317-333.
- Russell, B., E. R. Williams, M. Gosset, F. Cazenave, L. Descroix, N. Guy, T. Lebel, A. Ali, F. Metayer, and G. Quantin, 2010: Radar/rain-gauge comparisons on squall lines in Niamey, Niger for the AMMA. *Quart. J. Roy. Meteor. Soc.*, **136 (s1)**, 289-303.
- Schumacher, C., R. A. Houze, and I. Kraucunas, 2004: The tropical dynamical response to latent heating estimates derived from the TRMM Precipitation Radar. *J. Atmos. Sci.*, **61**, 1341-1358.

- Schumacher, C., M. H. Zhang, and P. E. Ciesielski, 2007: Heating structures of the TRMM field campaigns. *J. Atmos. Sci.*, **64**, 2593-2610.
- Sylla, M. B., F. Giorgi, P. M. Ruti, S. Calmanti, and A. Dell'Aquila, 2011: The impact of deep convection on the West African summer monsoon climate: A regional climate model sensitivity study. *Quart. J. Roy. Meteor. Soc.*, **137**, 1417-1430.
- Thompson, R. M., S. W. Payne, E. E. Recker, and R. J. Reed, 1979: Structure and properties of synoptic-scale wave disturbances in the intertropical convergence zone of the eastern Atlantic. *J. Atmos. Sci.*, **36**, 53-72.
- Thorncroft, C. D. and M. Blackburn, 1999: Maintenance of the African easterly jet. *Quart. J. Roy. Meteor. Soc.*, **125**, 763-786.
- Thorncroft, C. D., N. M. J. Hall, and G. N. Kiladis, 2008: Three-dimensional structure and dynamics of African easterly waves. Part III: Genesis. *J. Atmos. Sci.*, **65**, 3596-3607.
- Thorncroft, C. D. and K. Hodges, 2001: African easterly wave variability and its relationship to Atlantic tropical cyclone activity. *J. Climate*, **14**, 1166-1179.
- Wheeler, M. C. and H. H. Hendon, 2004: An all-season real-time multivariate MJO index: Development of an index for monitoring and prediction. *Mon. Wea. Rev.*, **132**, 1917-1932.
- World Meteorological Organization, 2011: Manual on Codes: International Codes, Volume I.1, Part A – Alphanumeric Codes. WMO-No. 306, Geneva, Switzerland.
- Yanai, M., S. Esbensen, and J.-H. Chu, 1973: Determination of bulk properties of tropical cloud clusters from large-scale heat and moisture budgets. *J. Atmos. Sci.*, **30**, 611-627.
- Yanai, M. and R. H. Johnson, 1993: Impacts of cumulus convection on thermodynamic fields. *Meteor. Monographs*, **24**, 39-62.
- Zhang, C. and S. M. Hagos, 2009: Bi-modal structure and variability of large-scale diabatic heating in the tropics. *J. Atmos. Sci.*, **66**, 3621-3640.
- Zipser, E. J., 1977: Mesoscale and convective-scale downdrafts as distinct components of squall-line structure. *Mon. Wea. Rev.*, **105**, 1568-1589.